Novel Grid-forming Control for Black Start Restoration Using MMC-HVdc Systems

By

Arash Fazel Darbandi

A Thesis submitted to the Faculty of Graduate Studies of
The University of Manitoba
in partial fulfillment of the requirements of the degree of

Doctor of Philosophy

Department of Electrical and Computer Engineering
Faculty of Engineering
University of Manitoba
Winnipeg, Manitoba

© Copyright by Arash Fazel Darbandi, 2021

This page was intentionally left blank.

Abstract

System-wide power outages are fortunately very rare. However, when they do occur, they can catastrophically affect tens or even hundreds of millions of customers. To minimize this impact, a “black start” power restoration, must be achieved in the minimum possible time. Challenges during restoration can include overvoltage or overcurrent in equipment, and the frequency transitioning outside the acceptable range. Though the ac transmission is at present the method of choice for black start restoration, HVdc transmission, where available, is proving to be an attractive alternative.

Earlier research has investigated connections to simplified systems. Real world systems can be more complex and have regions that are completely blacked out and remote islands of generation which have been started earlier, or were never blacked out. This thesis considers methods for restarting in such networks, and presents a novel grid-forming approach that allows the converter to be synchronized to a local generation with synchronous generators, inverter-based generation and/or an external energized network during the restoration process. The method provides fault ride-through capability during black start restoration and operation in a very weak system.

This thesis demonstrates the key attributes and effectiveness of the proposed methods through a series of Electromagnetic Transient (EMT) simulation study in both steady-state and dynamic conditions.

Acknowledgments

I would like to thank my advisor Dr. Aniruddha Gole for providing me with technical help and overall guidance with the project. His enthusiasm and inspiration have proved to be extremely encouraging throughout the project.

I take this opportunity to express my gratitude to Dr. Farid Mosallat for his valuable comments and suggestions towards progress of the research.

Of course no one could survive university life without help and support of family. Thanks for all their support in the past seven years. Without the combined effort of these people, this project could not have been completed.

Table of Contents

List of Tables

List of Figures

List of Symbols

A:	Ampere – a unit of electrical current
Ac:	Alternating Current – a type of electric current
C:	Capacitor
DC:	Direct Current – the unidirectional flow of electric charge
EMTDC:	Electromagnetic Transients including DC
F:	Farad – a unit of capacitance
H:	Henry – a unit of inductance
Hz:	Hertz – a unit of frequency
IGBT:	Insulated Gate Bipolar Transistor
L:	Inductor
Ohm (Ω):	Ohm – a unit of electrical resistance
MMC:	Modular Multi-level Converter
PI:	Proportional Integral
PSCAD:	Power System Computer Aided Design
PWM:	Pulse Width Modulation
R:	Resistor
rad:	Radian – a unit of angular measurement
SW:	Switch
V:	Volt – a unit of electromotive force
VSC:	Voltage Source Converter
W:	Watt – a unit of electric power

Chapter 1

Introduction

Electrical power is the most refined and valuable form of energy in today's world. Though system-wide power outages are rare, when they occur, their effects can be quite disruptive and sometimes catastrophic. A "black start" power restoration must be implemented to mitigate these effects [1][2].

Each Transmission System Operator (TSO) has a restoration plan to recover from total or partial outages as soon as possible. In a traditional ac system, one generator is designated as the black start unit, and is started first, and then connections are sequentially made to restore the full network configuration. The ac system has to be configured to a state of readiness before the restoration begins. For instance, the breakers must be in the correct position so that all extraneous circuits are off. Similarly, the protection must be

adjusted to avoid any undesired operation during the restoration process, and so on. The goal is to restore the critical loads as soon as possible. Each TSO identifies these critical loads based on its individual criteria [3]. Typically, critical loads include major hospitals, sewage plants, and critical station service loads.

During restoration, an overvoltage or overcurrent in equipment can sometimes occur, and the system frequency may also transition beyond an acceptable range. While black start restoration is often achieved through ac transmission, High Voltage Direct Current (HVdc) transmission, where available, is proving to be a suitable alternative.

HVdc transmission is being encouraged to reinforce the existing ac interconnected grid, as well as create new long distance interconnections. As the number of such long distance point-to-point HVdc connections gain more popularity and grow, it becomes an attractive alternative for black start restoration due to the introduction of Voltage-Sourced Converters (VSC).

HVdc technology has been around for over 50 years, but its development has recently experienced a significant growth. The next section provides a summary of the benefits and drawbacks of earlier research.

1.1 Literature Review

An electrical network must have the ability to re-energize after it has been disconnected and de-energized. In any case, it should be possible to restore the energy within the system after a blackout or disturbance. The power source to perform the restart and the number of machines that are able to perform such actions strongly depends on the size of the system. For instance, the requirements of a small offshore collecting power from some wind farms might differ significantly from those of a developed grid [4].

Black start has been proposed with the traditional Line-Commutated Converter based HVdc system (LCC-HVdc). However, LCC-HVdc relies on an ac system voltage for commutation and requires a complicated start-up sequence and control strategy for black start. The initial ac voltage required to start the dc converter itself is typically obtained by energizing a synchronous condenser or employing the ac filter banks [5]-[8].

More recently, VSC-HVdc transmission is gaining popularity over LCC-HVdc transmission [9]-[15]. The Modular Multi-level Converter (MMC) [16]-[20] is now becoming the topology of choice for VSCs, because it has lower losses and produces an essentially harmonic free ac voltage. Unlike the LCC, the VSC does not require any ac voltage source to start, as it synthesizes a three-phase ac voltage waveform from the dc voltage by appropriately switching its IGBT valves [16]-[20].

One challenge in using HVdc transmission for black start is the difficulty faced by HVdc converters when operating into very weak ac networks. Although VSC converters are better at this, even they are challenged when the short circuit ratio (SCR) is very low [21][22].

Reference [23] discusses the use of power synchronization (PSL) control that allows connection to either high-impedance or low-inertia systems. This method, similar to a synchronous generator, uses the internal synchronization mechanism of the ac system instead of using a phase locked loop (PLL). Hence, the SCR of the ac system is less of a limiting factor. The challenge of using this method is that the system can become unstable at high power levels [23].

The concept of self-synchronized and grid-forming inverters are introduced and discussed in [24]-[27]. The focus is on application of 2-level VSC in microgrid, where the shunt filter is used as a shunt current branch. This prevents the voltage loop controller to saturate when the inverter is not loaded [26][27]. This approach also allows limiting the current during the fault. These methods cannot be directly applied to the MMC since there is no shunt filter branch.

The concept of virtual impedance has also been introduced in [28][29]. This method has been utilized in the past for improving damping, mitigating impact of unequal or resistive line impedance and for current limiting [28][29]. However, the focus of [28][29] is on the application to a microgrid system. A comprehensive small-signal analysis is required to develop the virtual impedance control [28]. This becomes very complex for a larger system for MMC application. Furthermore, as discussed in [28][29], special care needs to be taken when selecting the virtual impedances to avoid system instability or eliminating the steady-state voltage drops. It can also result in excessive reactive power sharing when operating in parallel with synchronous generators.

The concept of virtual synchronous machine (VSM) has also been introduced in [30][31]. In this method the inverter operates in the manner of a synchronous machine, which automatically adjusts its “internal voltage” and “phase angle” to the network conditions without the requirement of an external synchronizing element such as a PLL [30][31]. Since the synchronous machines can maintain operation in various ac network conditions, it makes sense to develop a control method based on a synchronization process of two synchronous machines, and hence uses the VSM approach

1.2 Gaps in Existing Research

The previous research on grid-forming methods were investigated for a 2-level VSC in a microgrid system, which makes it difficult to directly apply to MMC application. The conditions in a microgrid are quite different from in a major transmission network, which can have connections to large remote systems and different mix of loads. Today, MMC technology is growing rapidly for either point-to-point connection or integration of long distance renewable energy. MMC converters are used in multi-gigawatt transmission applications, unlike microgrids, which are typically in the range of tens of Megawatts. Therefore, it is important to investigate the grid-forming methods using MMC based technology for black start restoration.

Earlier research has investigated connections to simplified systems. Real world systems can be more complex and have regions that are completely blacked out and remote islands of generation that have been started earlier, or were never blacked out. Use of MMC-HVdc system allows energizing a blacked out region by transferring power from a long distance energized network. In addition, it provides a “firewall” protection, which means if two systems are connected only through HVdc, a blackout event in one network will not propagate to other. Therefore, this thesis considers black start restoration methods for restarting in such networks.

1.3 Objectives and Procedures of the Research

This thesis proposes a voltage control methodology, which produces the reference currents for the decoupled current controller used to overcome the challenges of existing

methods and to suit MMC application. The method also improves fault ride-through capability. The use of analytical methods to tune the controller parameters is not fully effective since this approach is applicable to systems linearized around an operating point. Hence, an optimization wrapper controlling the EMT simulation is implemented to optimize the control parameters and improve the performance of the proposed control methodology.

Furthermore, the thesis offers a novel synchronization method that enables the converter to be synchronized to a local generation with synchronous generators, an inverter-based generation and/or an external energized network during the restoration process. First, a simple test case is developed to provide an in-depth understanding of proposed method and its functionality. In addition, two case studies are investigated to describe actual systems. The first case study is focused on the application of proposed method in a traditional ac system consisting of a local area with generation, and a tie to a remote network. The second case study is to demonstrate the functionality of proposed method in an inverter-based system consisting of an offshore and onshore wind power generation, a LCC and MMC link and a tie to a remote network to transfer the generated power. A series of EMT simulations on realistic test systems are conducted to verify the robustness of the proposed method.

1.4 Thesis Organization

The contents of this thesis are organized in the following manner:

Chapter 2 provides deep insight into the theoretical background of HVdc transmission, the existing VSC-HVdc control methods and black start restoration. Chapter 3 presents the proposed grid-forming method, and evaluate its basic functionality and performance. Chapter 4 compares the proposed method with the existing grid-forming approaches with current limiting capability, and describes the implemented optimization method for tuning the control parameters. Chapter 5 investigates the feasibility and robustness of proposed method in realistic setups during the black start restoration, disturbances and operation in a very weak system. Finally, Chapter 6 summarizes the findings of this thesis and presents the future work.

Chapter 2

Background to HVdc transmission, and Black Start Restoration

Power electronic technology provides more flexibility in terms of energy conversion and control, and has shown rapid growth in past two decades in modern power systems. This chapter provides in-depth background information on HVdc transmission technology, its existing control methods, and introduces the concept of black start restoration using HVdc system.

2.1 High Voltage Direct Current (HVdc) Transmission

Although the converter stations add extra cost and losses, HVdc transmission can have many advantages over ac transmission, and in some cases is the only solution possible. The next few sections will discuss the benefits of dc transmission as well as the existing VSC's control approaches.

2.1.1 Ac versus dc Transmission

Ac transmission is the most widely used transmission technology. However, dc transmission becomes more recommended for certain applications, i.e. interconnection of renewables and dc cables [37]-[40].

Dc transmission has proven higher capabilities for power transmission through underground cables. Underground cables have higher capacitance than overhead transmission lines because of their physical structures. Therefore, the capacitive current in cables generated by ac voltage causes the ac power transmission over a long distance to be almost impossible. For instance, for a medium length cable of 50 km, the losses generated by the capacitive current can be so high that the reactive power compensation needs to be installed in the middle of the cable [37]. Though, installing reactive power compensation can be quite expensive and may not even be practical, e.g. submarine cable transmission, dc transmission can eliminate the capacitive current losses for long distance dc cable transmission. Dc cable transmissions have lower losses than a corresponding ac cable. The converter station losses are normally as low as 0.6% per station, and dc cable losses are only around 0.3 to 0.4% per 100 km. Dc transmission also avoids the resonance between the cable capacitance and the inductive reactance of the grid [39]. Thus, the HVdc transmission is a feasible solution.

Another application area is for high power transmission over a long distance. HVdc transmission requires less power lines than ac transmission to transmit the bulk power over a long distance. Consequently, the costs and losses of the converter stations break even when the overhead transmission distance is around 600 km to 800 km [39] as shown in Figure 2.1. In addition, dc transmission does not have the stability limitation of ac transmission over a long distance [39].

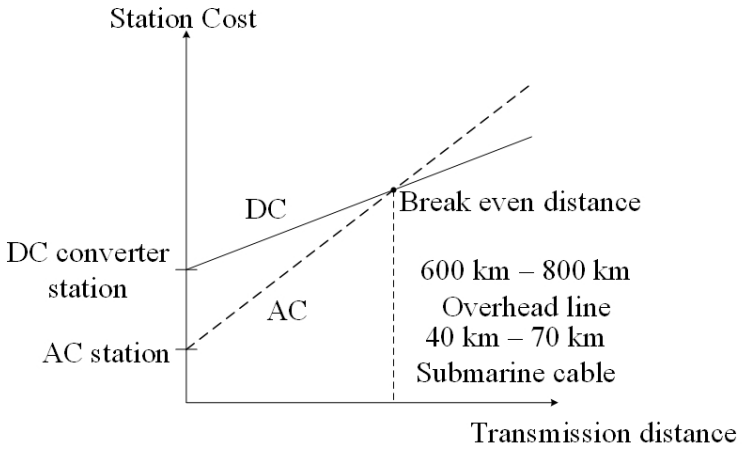

Figure 2.1: HVdc versus ac transmission break even distance [39].

Dc transmission also enables the connection of two unsynchronized ac systems. Ac transmission is only possible if the two interconnected ac systems have the same nominal frequency and operate synchronously, but dc transmission does not have such requirements. Therefore, many back-to-back HVdc links have been built for such purposes [4]. Higher controllability of the dc system can be exploited to improve the operating conditions of the interconnected grid. The ac voltage at either side can also be different, possibly saving the transformer.

In addition, dc transmission can improve the power system stability. One of the major features of the HVdc technology is its capability rapidly and accurately control the power flow, which can often be utilized to damp oscillations in the ac system. An example is where a HVdc system is used to damp low-frequency oscillations in ac systems by having an auxiliary damping controller [41]-[43]. Another example is the improvement of transient stability by increasing or decreasing the dc power for emergency power supports [40][44].

Large interconnected ac systems have many well-known advantages. For instance, the possibility of using larger and more economical power plants, reduction of reverse capacity in the systems, utilization of the most efficient energy resources, as well as achieving an increase in system reliability [45]. However, larger interconnected ac systems also increase the system complexity from the operational point of view. One of the consequences of such complexity is the large blackouts in America and Europe [46]. In this aspect, HVdc links

have the “firewall” function in preventing cascaded ac system outages spreading from one system to another [47].

2.1.2 Existing dc Transmission Technologies

2.1.2.1 Line Commutated Converter (LCC)

Converters based on either mercury valves or Thyristor valves are called line-commutated converters (LCCs), or current-source converters (CSCs). The basic module of a LCC is the 6-pulse bridge circuit shown in Figure 2.2. Although there are several alternative configurations possible, the 6-pulse bridge has been universally used for LCC-HVdc converters as it provides better utilization of the converter transformer and a lower voltage across the valve when not conducting [40].

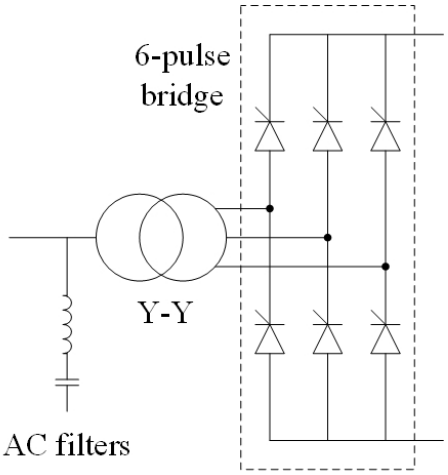

Figure 2.2: A 6-pulse bridge including phase reactance [39].

The Graetz Bridge can be used for transmitting power in two directions, i.e. the rectifier mode and the inverter mode. In either case, the flow of dc current is unidirectional, but the dc voltage polarity is reversible. This is achieved by applying different firing angles on the valves. If the firing angle is lower than 90^{o}, the direct current flows from the positive terminal of dc circuit, thus the power is following from ac side to dc side; if the firing angle is higher than 90^{o}, the direct voltage changes polarity, thus the direct current flows from the negative terminal of dc circuit. The power then flows from dc side to ac side. A HVdc

link is essentially constructed by two Graetz bridges, which are interconnected on dc sides. The interconnection could be an overhead line, a cable, or a back-to-back connection [40]. An alternative converter topology is the Voltage Sourced Converter (VSC) where the dc voltage is unidirectional, but the dc current changes direction. This will be discussed in section 2.1.2.2.

The application of LCC-HVdc technology has been very successful and the installations of LCC-HVdc links are expected to grow at least in the near future. However, the LCC technology suffers from several inherent weaknesses.

One problem is that the LCC always consumes reactive power, either in rectifier mode or in inverter mode. Depending on the firing angles, the reactive power consumption of a LCC-HVdc converter station is approximately 50-60% of the active power [40]. The reactive power consumption requires compensation by connecting large ac filters or capacitors at the converter stations. For a common LCC-HVdc link, the filters or capacitors not only increase the costs, but also occupy a large amount of space of the converter stations. Besides, large filters or capacitors also contribute to the temporary overvoltage (TOV) and low-order harmonic resonance problems of the HVdc link when connects to a weak system [48][49].

Another well-known problem of the LCC-HVdc system is the occurrence of commutation failures at the inverter station typically caused by disturbances in the ac system. Either depressed voltage magnitude or phase-angle shift of the alternating voltage may reduce the extinction volt-time area of the inverter valve [50][51]. If the extinction angle of the inverter valve is smaller than $5^{o} – 6^{o}$, the previously conducting valve will regain current, which will end up with a commutation failure. The commutation failure creates a short circuit on the dc side, which essentially temporarily stops the power transmission. Commutation failures are common phenomena of LCC-HVdc systems. A single commutation failure generally does no harm to either the converter valves or the ac system. However, a number of repeated commutation failures may force the HVdc link to trip [52].

While the above two problems can be mitigated relatively easily, a third problem described below can become a major limiting factor for LCC-HVdc applications. For LCCs, the successful commutation of the alternating current from one valve to the next

relies on the stiffness of the alternating voltage, i.e. the network strength of the ac system. If the ac system has low short circuit capacity relative to the power rating of the HVdc link, i.e. low short circuit ratio (SCR), more problematic interactions between the ac and the dc systems are expected. Besides, the SCR of the ac system also imposes an upper limit on the HVdc power transmission, which is often described by the well-known maximum power curve (MPC) [49]. Therefore, it becomes challenging to use LCC-HVdc when operating into a very weak ac network during the black start restoration.

An improved topology of the LCC-HVdc system to overcome part of the above mentioned problems is the capacitor-commutated converter (CCC) HVdc technology, where ac capacitors are inserted in series between the valves and converter transformers [53]. The series-connected capacitors not only supply the reactive power consumed by the valves, it also improve the dynamic performance of the HVdc system. However, the major drawback of the CCC concept is that the series capacitors increase the insulation costs of the valves. Thus, the CCC-HVdc technology has been so far only applied to back-to-back HVdc links, where the voltage level of the valves is much lower [53].

2.1.2.2 Voltage-Source Converter (VSC)

VSCs utilize self-commutating switches, i.e. gate turn off thyristors (GTOs) or insulated gate bipolar transistors (IGBTs), which can be turned on or off freely. This is in contrast to the LCC where the thyristor valve can only be turned off by reversed line voltages. Therefore, a VSC can produce its own sinusoidal voltage waveform independent of the ac system. Many different topologies have been proposed for VSCs. In HVdc applications, VSCs are typically one of three types: two-level converter, three-level converter, and modular multilevel converter (MMC) [16]-[20].

The MMC is currently favored, as it has lower losses and produces nearly harmonic free ac sine wave output in comparison to two- and three-level VSC arrangements [16]-[20]. In addition, compared to the two-level and three-level topologies, one major feature of the MMC is that no common capacitor is connected at the dc side. Instead, the dc capacitors are distributed into each module, while the converter is built up by cascade connected modules as shown in Figure 2.3.

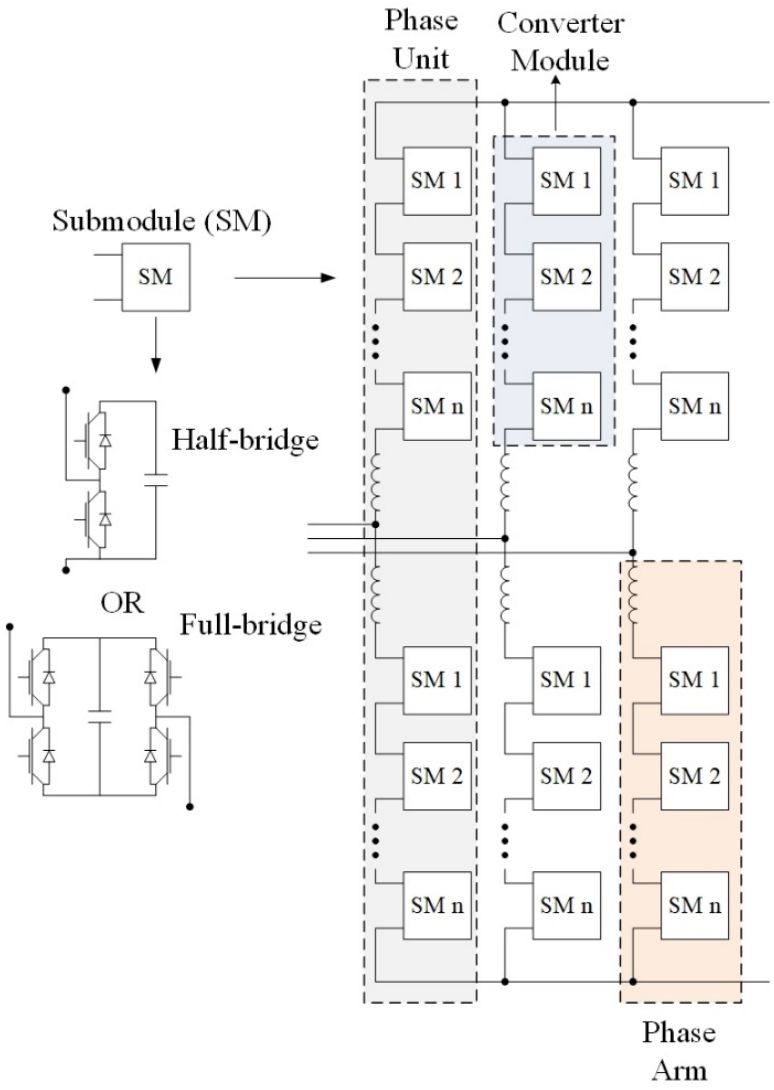

Figure 2.3: An example of 3-phase MMC valve [58].

The MMC concept is especially attractive for high voltage applications, since the converter can be easily scaled up by inserting additional modules in each arm. If a considerable amount of modules are cascaded, each module theoretically only needs to switch on and off once per period, which greatly reduces the switching losses of the valves. However, preliminary investigation indicates that slightly higher switching frequencies are necessary [54]. With MMC, the harmonic content of the voltage produced by the VSC is so low that additional filtering equipment is almost unnecessary as demonstrated in Figure 2.4

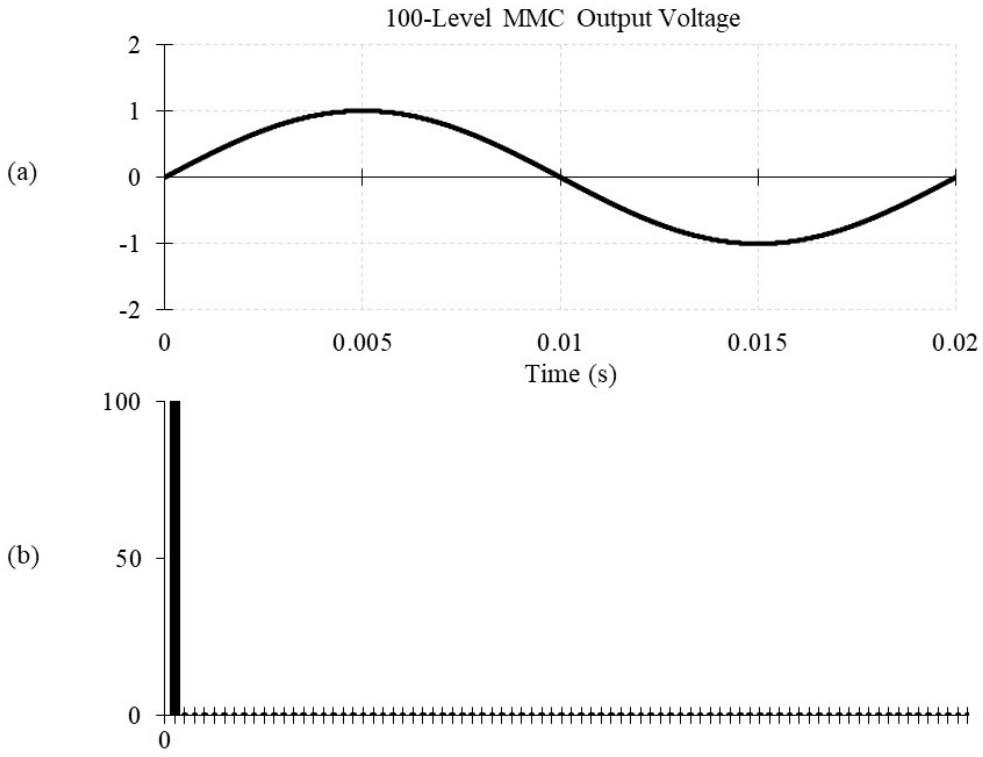

Figure 2.4: (a) The output voltage produced by 100-level MMC (b) The harmonic spectrum of the output voltage produced by 100-level MMC.

An additional benefit of MMC is that the control system has an extra freedom in dealing with faults at dc side. The dc capacitors are not necessarily discharged during faults. Thus, the fault recovery can be faster [55].

Compared to the two-level and three-level topologies, the major drawback of the MMC topology is that the required switching components are doubled since only one of the valves of each module contributes to the phase voltage when the module is inserted in. In addition, the design and control of MMC are generally more complex compared to the two-level converter [56]. However, since the switching frequency of MMC can be kept very low, switches with higher blocking voltages may be used, which in turn limits the increase in number of switches. On the other hand, the reduction of switching losses and saving on filtering equipment of MMC may eventually justify its application for HVdc transmission [57].

No matter what converter topology is used, the VSC can always be treated as an ideal voltage source where the control system has the freedom to specify the magnitude, phase, and frequency of the produced sinusoidal voltage waveform. However, for control design and stability analysis, it is important to take into account the limitation of the converter in terms of active and reactive power transfer capability [59][60].

One such limit is the converter current limitation, which is imposed by the current carrying capability of the VSC valves. Both the active power and the reactive power contribute to the current flowing through the valves. On the PQ diagram, this limits the operating region to the interior of circle whose radius is the maximum permitted MVA rating as illustrated in Figure 2.5. Accordingly, if the converter is intended to support the ac system with reactive power supply or consumption, the maximum active power has to be limited to make sure that the valve current is within the limit [60].

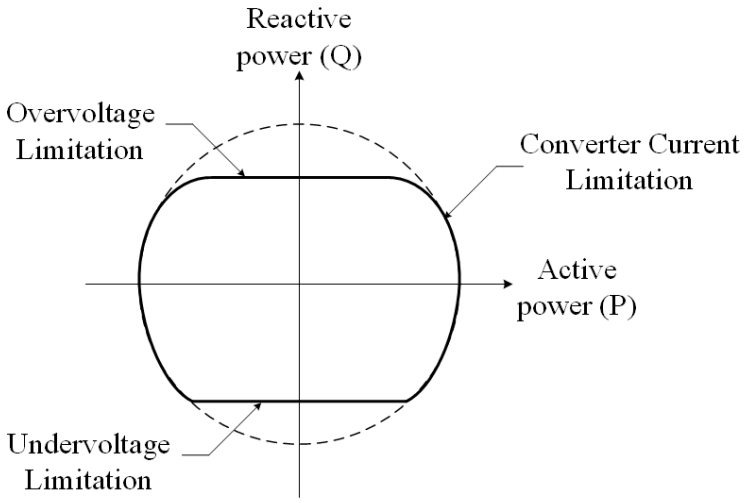

Figure 2.5: PQ capability curve for a typical VSC-HVdc converter [60].

Another limitation which determines the reactive power capability of the VSC is the over or under voltage magnitude of the VSC (modulation index limitation). The overvoltage limitation is imposed by the direct voltage level of the VSC. The undervoltage limit, however, is limited by the main circuit design and the active power transfer capability, which requires a minimum voltage magnitude to transmit the active power [60]. In this respect, the tap changer of the converter transformer can play an important role to

extend the reactive power limitation of the VSC. This could be an argument to have converter transformers in VSC-HVdc systems [60]. Figure 2.5 shows the PQ diagram with the above mentioned limitations for a typical VSC-HVdc converter [60].

VSC-HVdc technology overcomes most of the weaknesses of the LCC-HVdc technology. In addition, it supports the ac system with reactive power supply or consumption. Similar to a LCC-HVdc system, a VSC-HVdc system can quickly increase or decrease the active power for ac system emergency power support. In addition, it can also instantly reverse the active power [40].

Since the direct voltage of a VSC-HVdc system varies in a much smaller range than a LCC-HVdc system, extruded cables can be used for VSC-HVdc systems. The extruded cable reduced the cable cost and the construction cost. The latter makes long distance land cable transmission possible [59][60].

2.1.3 Existing Grid Synchronizing Techniques

The next sub-sections discuss existing approaches to grid-following and grid-forming control.

2.1.3.1 Grid-following Control Techniques

The grid-following control technique in VSCs can be categorized into an upper level controller and a lower level controller [58]. The upper level controller accept the dispatcher's orders (e.g. active and reactive power, or ac and dc voltage reference) and create the ac reference voltage for the lower level controls. This level of controller is largely independent of the converter topology (e.g. two- or three-level VSC or MMC). The lower level controls are specific to the converter topology. Figure 2.6 shows the structure of the grid-following control method.

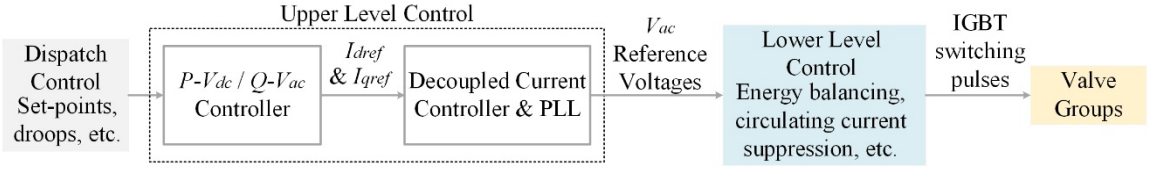

Figure 2.6: The structure of the grid-following control [58]

Figure 2.7 shows the details of the upper level controller [58][61][62]. The active power control loop can be configured by the dispatch controller to regulate either the dc voltage or the active power if the ac system is sufficiently strong. The reactive power control loop can be arranged to regulate either the ac voltage or the reactive power at the point of connection (POC).

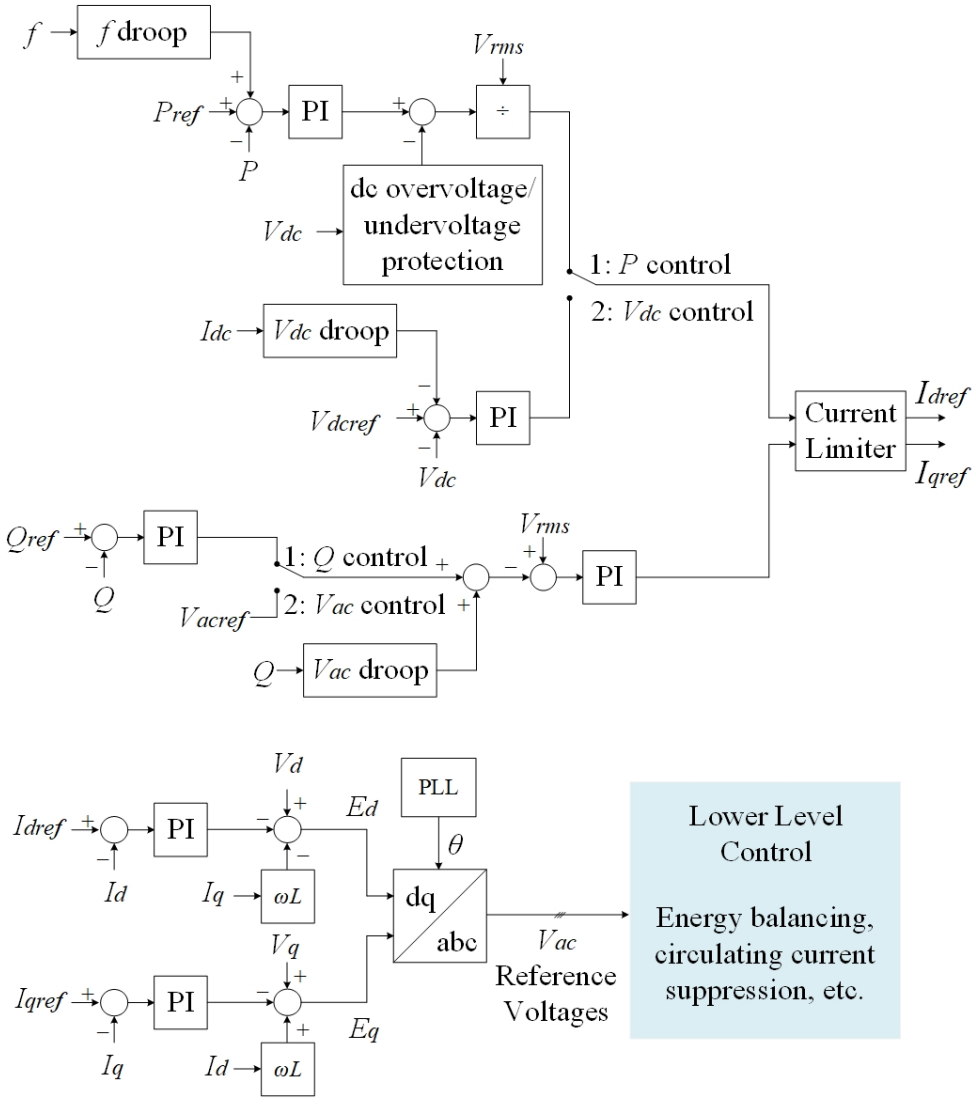

Figure 2.7: Upper level control structure for grid-connected operation [58]. Here f ($\omega = 2\pi f$) is the system frequency. L is the total leakage inductance of the interface transformer plus the equivalent inductance of the arm reactors.

The power sharing among several converters connected to the same system is achieved by implementing some standard droop controls as follows,

- Dc voltage droop is implemented when operating in conjunction with other dc voltage controlling converters.
- Ac voltage droop is implemented when operating in conjunction with other converters on the ac side, or with other sources of reactive power that operate as ac voltage regulators, i.e. SVC, STATCOM, etc.
- Frequency droop is implemented when the converter is operating in the active power control mode and is required to have a more active role in the control of the ac system frequency.

The direct (*d*) and quadrature (*q*) axis current orders are determined by the active and reactive power control as depicted in Figure 2.7. The key requirement for this approach is the connection to an external system or other synchronous machines to generate the three-phase voltage and establish the system frequency so that the PLL can be synchronized. The PLL generates the reference frame angle by locking onto the ac voltage at POC. The current and voltage measurements will then be converted into *dq*-frame.

The advantages of using decoupled current control strategy are as follows [58][61][62],

- The active and reactive current can be controlled independently, which was not possible with previous control methods.
- A maximum magnitude can be set for the ac current. This limits overcurrent during faults. The converter's current limit can easily be determined as shown in Figure 2.8a.
- If the reactive current is needed to support the ac voltage during the disturbances, the magnitude of reactive current can easily be controlled as shown in Figure 2.8b.

The lower level controls take the reference voltage for the three-phase output voltage of the VSC. They are topology specific and have a different form depending on the topology (e.g., two-, three-level or MMC). The basic timing for generating the IGBT firing signals is provided by PLL, which generates a reference angle that is synchronized to the voltage at the POC.

One challenge of grid-following control is the stability of its PLL when the short circuit ratio (SCR) is very low [21][22]. This becomes crucial during the black start

restoration because there are no other synchronous machines or an external system to generate the three-phase voltage and establish the system frequency so that the network can be energized.

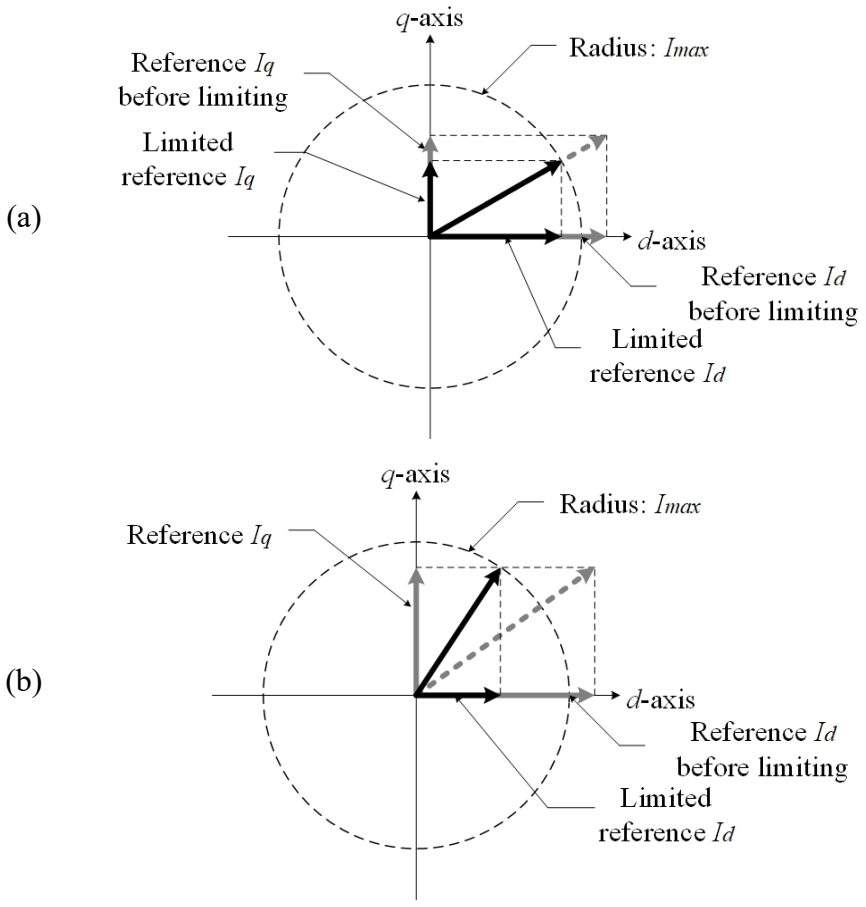

Figure 2.8: Current limiter

2.1.3.2 Grid-forming Control Techniques

In contrast to grid-following control discussed above, grid-forming control has the ability to generate its own internal voltage magnitude and frequency. Therefore, it can connect to a totally passive network (no intrinsic generation). Grid-forming control can also be used for connecting to a very weak ac system where the converter plays the major role in establishing ac system frequency.

In the grid-following mode, the PLL generates the reference angle, while in grid-forming mode; a Voltage-Controlled Oscillator (VCO) controls the system frequency and generates the required reference angle (θ).

Figure 2.9 shows the upper level of the grid-forming control structure discussed in [58]. The lower level controls are essentially identical between grid-following and grid-forming control techniques.

The voltage control loop regulates the magnitude of ac voltage at POC by generating the voltage reference V_{dref} while V_{qref} is set to zero. If the VSC is connected to an ac system with a comparable capacity, then the frequency droop becomes critical to coordinate the power generation between the converter and other synchronous machines.

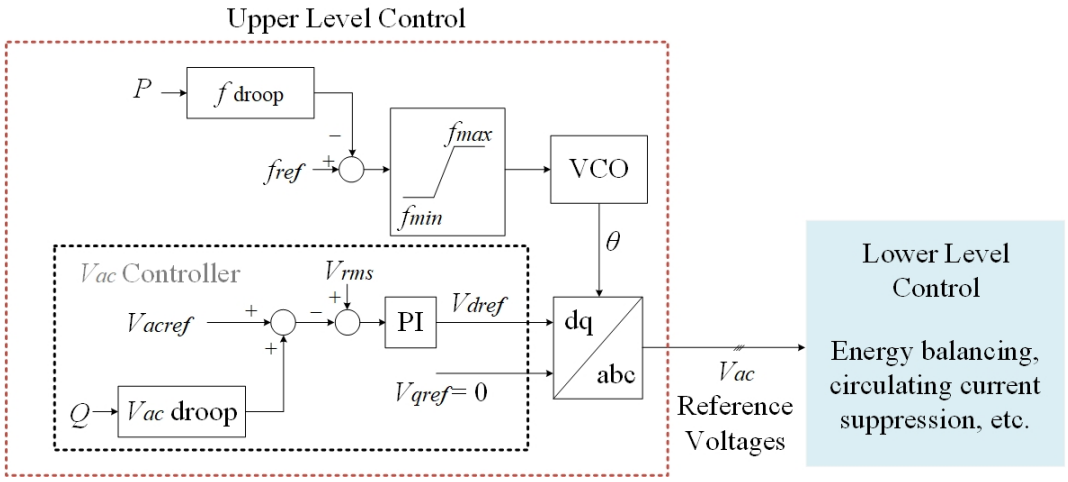

Figure 2.9: Upper level control structure for grid-forming operation [58]

A VCO generates the reference angle to control the system frequency to the desired reference value. This method is useful when connecting to a passive network. The main drawbacks of this approach, if used as shown in Figure 2.9, are as follows,

- Additional control features are required to limit the current to avoid damaging the valves during faults.
- Additional control features are required to synchronize to an external network or synchronous machine.

Several methods are available for limiting the current. These include inserting a current controller in tandem with the voltage controller. The concept is introduced and discussed in [24]-[27]. The focus is on application of 2-level VSC in microgrid, where the shunt filter is used as a shunt current branch as shown in Figure 2.10 [26][27]. L is the total series inductance of shunt filter, C is the shunt filter's capacitance, $\boldsymbol{V_{cdq}}$ and $\boldsymbol{I_{Ldq}}$ are the dq-components of shunt filter capacitor voltage and inductor current respectively.

Similar to Figure 2.9, V_{ac} controller can be used to regulate $\boldsymbol{V_{cdqref}}$ to a desired reference value. Then, the voltage control loop generates the dq-reference currents from the voltage references V_{cdref} and V_{cqref}. It outputs the dq-components of the reference current for the decoupled current control block that follows. The dq-components of internal voltages, $\boldsymbol{E_{dq}}$, are derived by compensating for the series impedance drop across the total VSC's filter branch. This approach allows limiting the current during the fault. However, this method cannot be directly applied to MMC since there is no shunt filter branch.

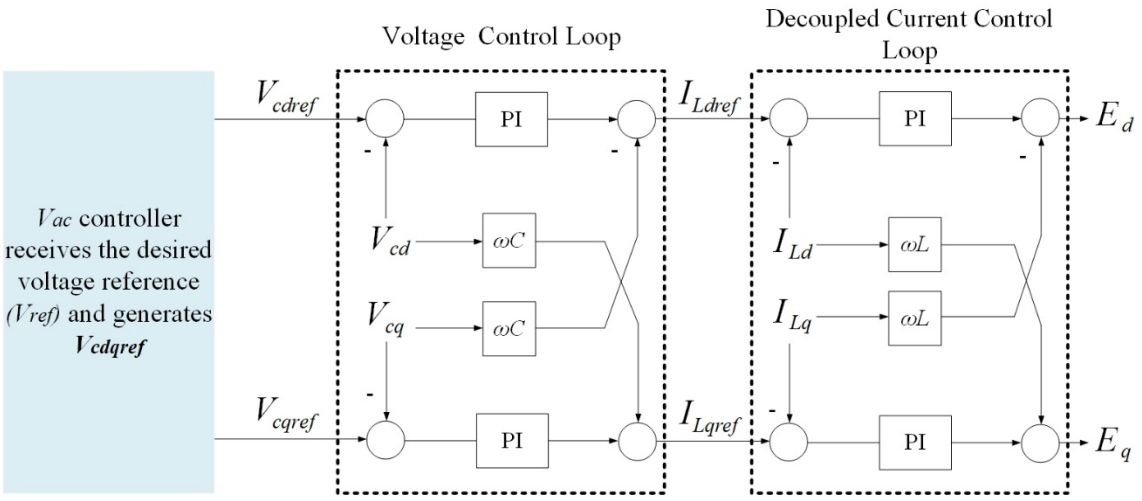

Figure 2.10: Dual loop control method [26][27].

The concept of virtual impedance has also been introduced in [28][29]. This method has been utilized in the past for improving damping, mitigating impact of unequal or resistive line impedance and for current limiting [28][29]. In this method, an external voltage regulator is implemented to maintain the POC voltage magnitude to its reference value. During the steady-state operation, the converter operates in grid-forming mode

shown in Figure 2.9 and the virtual impedance control mode is only enabled during transients to limit the valve current. The virtual impedance is usually selected as a series *R-L* circuit, $Z_{virtual} = R_{virtual} + j\omega L_{virtual}$. In this mode, the *dq*-components of VSC's internal, $\boldsymbol{E_{dq}} = [E_d, E_q]^T$, are derived by compensating for the series impedance drop across the $Z_{virtual}$ and the total VSC side inductance, *L*, as in (1).

$$\boldsymbol{E_{dq}} = \boldsymbol{V_{dqPOC}} - \begin{bmatrix} R_{virtual} & \omega(L_{virtual}+L) \\ -\omega(L_{virtual}+L) & R_{virtual} \end{bmatrix} \cdot \boldsymbol{I_{dqvalve}} - (L_{virtual}+L) \cdot \frac{d}{dt}(\boldsymbol{I_{dqvalve}}) \quad (1)$$

Where,

$\boldsymbol{E_{dq}} = [E_d, E_q]^T$ is the VSC's internal voltage vector in *dq*-coordinates

$\boldsymbol{V_{dqPOC}} = [V_{dPOC}, V_{qPOC}]^T$ is the POC voltage vector which is equal to $[V_d, 0]$ in the steady state

$Z_{virtual} = R_{virtual} + j\omega L_{virtual}$: the designed virtual impedance

ωL: the total VSC side inductance

$\boldsymbol{I_{dqvalve}} = [I_{dvalve}, I_{qvalve}]^T$ is the valve side current vector

The focus of [28][29] is on the application to a microgrid system. Also, as discussed in these publications, selecting the value of the virtual impedance requires special attention to avoid system instability, and the steady-state voltage drops. In addition, excessive reactive power sharing can occur when operating in parallel with synchronous generators. Therefore, a comprehensive small-signal analysis is required to develop the virtual impedance control [28], which is challenging for a larger system whose structure and operating point changes unpredictably.

2.1.3.2.1 Virtual Synchronous Machine (VSM) Concept

The concept of VSM has also been introduced in [30][31]. The main advantages of VSM approach include [30][31],

- Operation in both grid-following and islanded conditions.
- Provide frequency support and power sharing as its primary control scheme.
- Only requires the local measurements, e.g. does not depend on any external communications.

- No conflict with other external control structures.
- Its theoretical simplicity.

In this method, the grid-forming converter of Figure 2.9 operates in the manner of a synchronous machine, which automatically adjusts its "internal voltage", E, and "phase angle", θ, to the network conditions without the requirement of an external synchronizing element such as a PLL. This is accomplished by emulating synchronous machine's mechanical equation given in (2). As this is a virtual machine, we could give it an idealized form, with internal voltage, E, and its synchronous reactance, X, is the same as ωL of the VSC as described in section 2.1.3.2.

$$J\frac{d\omega_m}{dt} + D\omega_m = T_m - T_e \tag{2}$$

Using Laplace transformation, (2) can be written as,

$$\Omega_m(s) = \frac{T_m(s) - T_e(s)}{J \cdot s + D} \tag{3}$$

Where,

J: the total moment of inertia of the turbine and generator rotor
D: the damping coefficient
ω_m: the rotor shaft mechanical speed (Ω_m is the speed in Laplace domain)
T_m: the given virtual mechanical torque
T_e: the measured virtual electromagnetic torque

Neglecting resistance, the transmitted power, P is as in (4)

$$P = \frac{E \cdot V_{POC}}{\omega L} sin\,\theta \tag{4}$$

Where,

E and V_{POC}: are the machine's internal voltage and terminal voltage magnitudes respectively
θ: the electrical angle separating E and V_{POC}
ωL: the total reactance separating E and V_{POC}

From (4) it can be seen that an effective mechanism for power transfer is to regulate the angle θ, which is done through controlling the virtual mechanical torque, T_m in (2). This results in the mechanical speed of the rotor, ω, to be regulated as per (2) which corresponds to the rotor reference angle, θ, as shown in (5).

$$\theta = \int \omega \cdot dt \tag{5}$$

As discussed earlier, an external voltage regulator is implemented in VSM approach to maintain the terminal voltage magnitude to its reference value [30][31].

Reference [23] discusses the use of power synchronization control that allows connection to either high-impedance or low-inertia systems as shown in Figure 2.11. Similar to a synchronous generator, this method uses the internal synchronization mechanism of the ac system instead of using a PLL. The advantage of this method is that the SCR of the ac system will be less of a limiting factor. The challenge, on the other hand, is that the system can become unstable at high power levels [23].

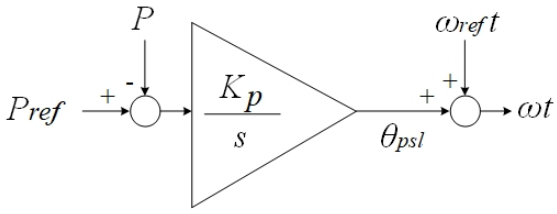

Figure 2.11: Power synchronizer scheme [23]

The next chapter will present a new grid-forming and synchronization technique to suit MMC application and overcome the challenges associated with existing methods.

2.2 Black Start Restoration (BSR) Using HVdc Systems

As stated previously, system-wide power outages are fortunately very rare, but when they do occur, a region can be effected from minimal to disastrous degrees. To mitigate this impact, a “black start” power restoration must be achieved as quickly as possible.

Each TSO has a restoration plan to recover from total or partial outages as soon as possible. In a traditional ac system, one generator is designated as the black start unit. Connections are then made in sequence to restore the full network configuration. Before

restoration begins, however, the ac system has to be configured to a state of readiness. First, the breakers must be in the correct position so that all extraneous circuits are off. Additionally, the protection must be adjusted to avoid any undesired operation while restoration occurs. Once a state of readiness has been achieved, restoration of the critical loads needs to occur as quickly as possible. Each TSO identifies these critical loads based on its individual criteria [3]. Typically, critical loads include major hospitals, sewage plants, and critical station service loads.

As mentioned, some challenges faced during restoration include overvoltage or overcurrent in equipment, and the frequency transitioning outside an acceptable range. Though ac transmission is presently the method of choice for black start restoration, HVdc transmission, where available, is proving to be an attractive alternative.

Black start has been proposed with the traditional LCC-HVdc system, which relies on an ac system voltage for commutation and requires a complicated start-up sequence and control strategy. The initial ac voltage required to start the dc converter itself is typically obtained by energizing a synchronous condenser or employing the ac filter banks [5]-[8].

More recently, VSC based HVdc transmission is gaining popularity over LCC-HVdc transmission [9]-[15]. The MMC [16]-[20] is now becoming the topology of choice for VSCs, as it has lower losses and produces an essentially harmonic free ac voltage. Unlike the LCC, the VSC does not require any ac voltage source to start since it synthesizes a three-phase ac voltage waveform from the dc voltage by appropriately switching its IGBT valves [16]-[20].

2.2.1 Benefit of Energizing Long Transmission Line and Large Transformer Using VSC-HVdc Systems

One of the advantages of using VSC-HVdc is the ability to control the ac voltage during the black start. This eliminates some of the challenges faced by traditional ac system when energizing a large transformer or a long transmission line. For example, an excessive inrush current can occur when energizing a large transformer which can result in an undesirable ac voltage dip, or harmonic distortion. Although the synchronized closing of the circuit breaker is a common practice to avoid such high inrush current, the ac voltage

controllability offered by VSC-HVdc can achieve the same effect. The breaker can be closed first, and then the voltage ramped up as shown in Figure 2.12, resulting in no inrush current.

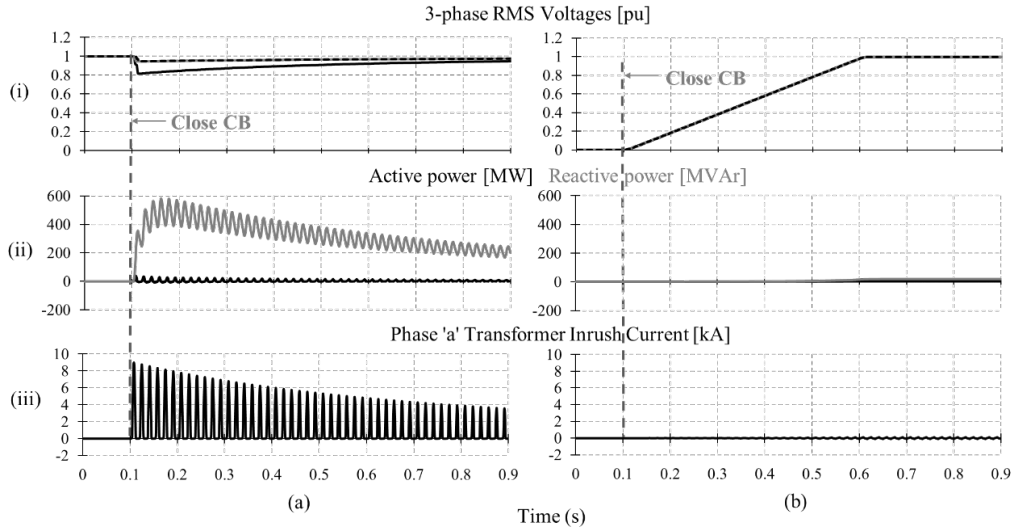

Figure 2.12: Energizing of a large transformer (a) in traditional ac system (b) in presence of VSC-HVdc

One of the challenges of energizing a long transmission line is the Ferranti effect which results in high temporary overvoltage at the open end. Also, the higher switching transients at the closing end during the energization is inevitable. Figure 2.13 demonstrates the benefit of using VSC-HVdc to energize a long transmission line when available. The ability to control the voltage by VSC-HVdc essentially eliminates any potential switching transients and temporary overvoltage at the closing and open end respectively.

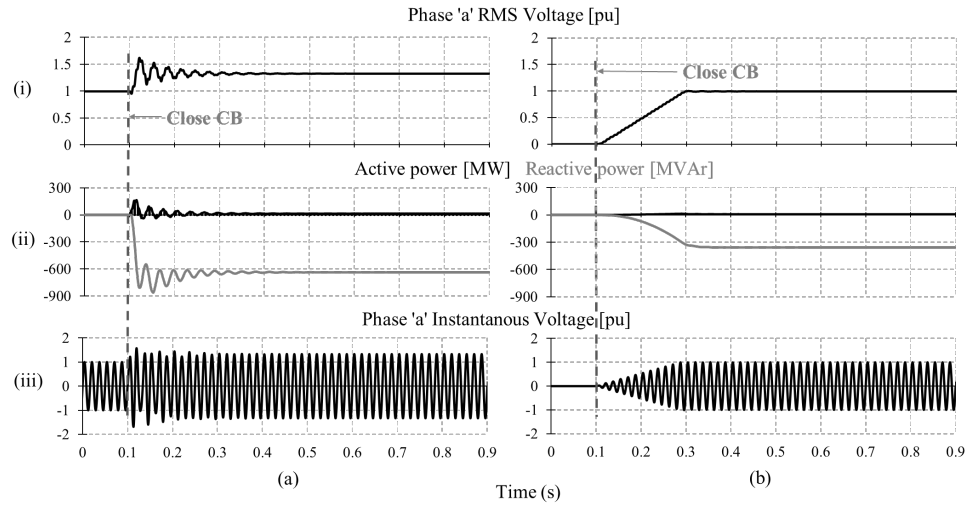

Figure 2.13: Energizing a long transmission line (a) in traditional ac system (b) in presence of VSC-HVdc

2.2.2 Black Start into Weak Ac Network Using VSC-HVdc Systems

One challenge in using HVdc transmission for black start is the difficulty faced by HVdc converters when operating into very weak ac networks. Although VSC converters are better at this, they are also challenged when the SCR is very low [21][22].

In traditional all-ac grids, two ac networks are connected by closing a circuit breaker when the voltage magnitudes and phase angles across the breaker are nearly equal. To achieve this, governor and exciter set points have to be adjusted by a synchronizing mechanism (synchroscope) to assure that the voltage magnitudes, angles and frequencies are in a close range, and thus prevent undesired transients when the breaker is closed.

During restoration of a purely ac network, it is probable that several "islands" can first be energized and then connected to each other. Perfect coordination of voltage magnitude and phase angles for two such ac networks before circuit breaker closing is a problem, because it requires coordinated control of several machines in both networks. Hence, the circuit breaker is generally closed with some voltage across it, which may result in a high transient power swing and large current surges between two systems. However, if a VSC link is present at the circuit breaker bus, the phase angle and voltage magnitude become controllable and the problem can be avoided. Chapter 3 demonstrates the effectiveness of proposed grid-forming approach to overcome the challenges faced during the black start restoration and operation in a very weak system.

2.3 Chapter Concluding Remarks

Chapter 2 discussed the advantages of dc transmission, the existing HVdc technologies, and the available grid synchronizing approaches. Moreover, this chapter discussed the benefits and challenges of existing methods in detail. The next chapter will evaluate the proposed grid-forming control method for black start restoration using MMC-HVdc systems. A detailed analysis of proposed method will serve as the main contribution of this research work.

Chapter 3

Proposed Grid-forming Control Method for MMC-HVdc Systems

This chapter proposes a new grid-forming methodology that addresses challenges of the existing methods described in Chapter 2. It includes the ability to:

- Work well for black start scenarios. For instance, the ability to energize passive elements and loads.
- Limit the current during the fault.
- Allow synchronizing either to an external network or to a purely passive network.
- Work as part of a larger system whose structure and operating point can change unpredictably.

The proposed control topology is a voltage control methodology along with a decoupled current controller to provide fault ride-through capability and suit MMC application. In addition, a new synchronization method is developed to allow synchronization to a local generation with synchronous generators, inverter-based generation and/or an external energized network during the restoration process. This chapter presents the proposed grid-forming method for black start restoration using MMC-HVdc systems. It also evaluates its basic functionality and performance.

Figure 3.1 shows the arrangement of the proposed method and the measurement points. The proposed approach, as shown in Figure 3.1, uses a similar upper level control structure as [26][27] to generate the voltage magnitude reference, V_{dref}, but has additional features such as an enhanced power control and synchronization loop; and current limiting to ensure smooth black start synchronization and successful fault ride-through.

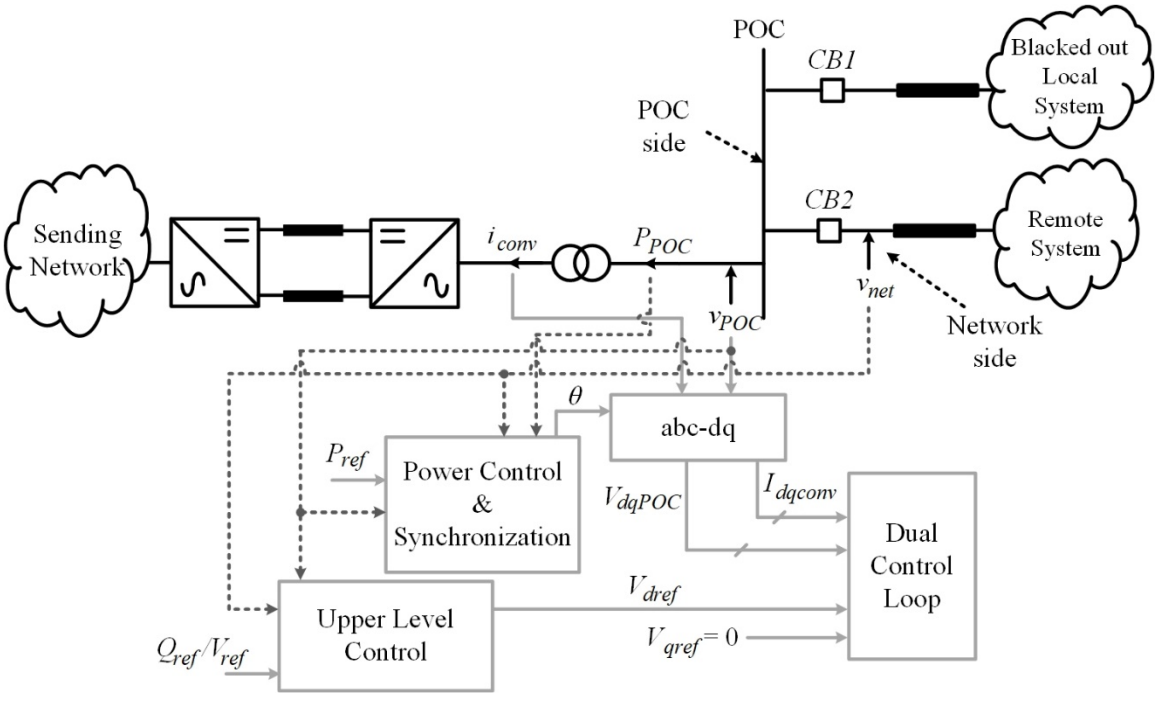

Figure 3.1: The arrangement of the proposed method and the measurement points

3.1 Power Control and Synchronization Concept

In traditional all-ac system, the synchronization is achieved by means of a transient power transfer [63] . Since the synchronous machines can maintain operation in various ac network conditions, it makes sense to develop a control method based on a synchronization process of two synchronous machines, and hence uses the "Virtual Synchronous Machine" described in section 2.1.3.2.1. This becomes crucial when black starting a connection to a purely passive network (i.e., impedance load) because there is no ac voltage to synchronize, e.g. other synchronous machines at the beginning. The proposed power control and synchronization is fundamentally an emulation of the swing equation discussed in Chapter 2. However, as the machine frequency is very close to the system frequency, the per-unit torque error in (2) of the previous chapter is essentially equal to the per-unit power. Therefore, the swing equation in per-unit form can be written as (6).

$$J\frac{d\Delta\omega}{dt} + D\Delta\omega = \Delta P \tag{6}$$

Where,

J: the total inertia
D: damping coefficient
Δω: the speed deviation
ΔP: the difference between reference and measured power

Using Laplace transformation, (6) can be written as,

$$J \cdot s \cdot \Delta\omega + D \cdot \Delta\omega = \Delta P \tag{7}$$

Simplified (7),

$$\Delta\omega = \frac{1}{J \cdot s + D}\Delta P \tag{8}$$

Therefore, the system frequency can be generated by (8),

$$\omega = \omega_{ref} + \Delta\omega \tag{9}$$

The reference angle, θ, can be calculated by integration of (9) as shown in (10).

$$\theta = \int \omega \cdot dt \tag{10}$$

The proposed power control and synchronization loop is shown in Figure 3.2. This method, similar to a synchronous generator, uses the internal synchronization mechanism of the ac system instead of using a PLL to generate the system frequency. A speed deviation, $\Delta\omega$, is generated by the power control and synchronization loop and added to the reference speed, $\omega_{ref} = 2\pi f_0$ (f_0: fundamental frequency), to generate the reference angle, θ, which is used to resolve the dq-components of the voltages and currents.

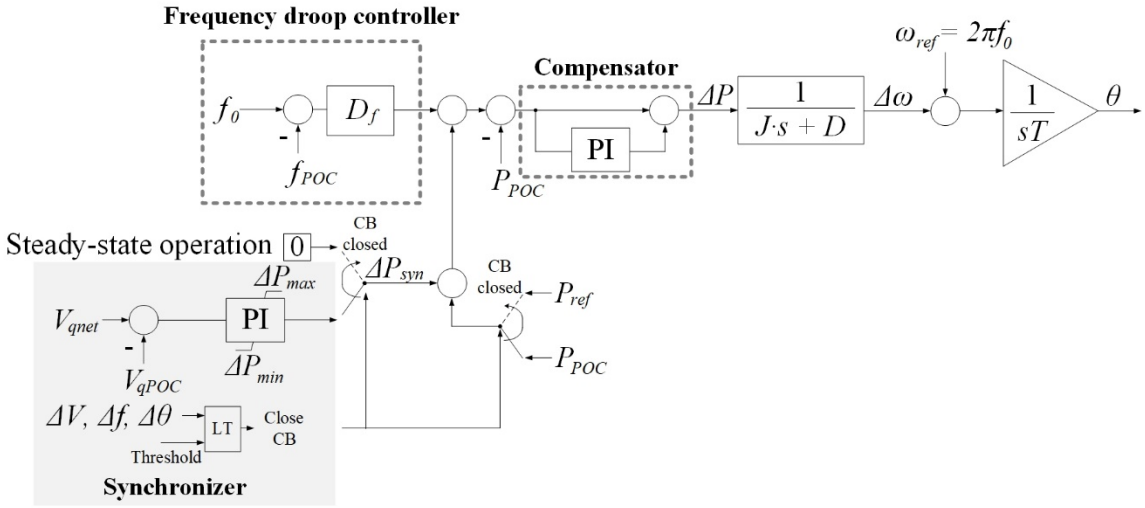

Figure 3.2: The proposed synchronization block diagram. Here, f_m, P_m and P_{ref} are measured system frequency, measured active power at the line side of the interface transformer and the reference power respectively. The V_{qnet} and V_{qconv} are the q-component of the voltage measured at the network side and POC side of the circuit breaker respectively.

The PI element in Figure 3.2 is a compensator, which is introduced to eliminate any accumulating error between ordered and measured power during the steady-state operation, particularly when the system frequency has changed. Note that, as mentioned in the previous chapter, this method, unlike classical d-q control, regulates the real power by

changing $\Delta\omega$, which in turn introduces a phase shift $\Delta\theta$ between the internally generated voltage and the bus voltage. In steady-state, this leads to the q-component of voltage becoming zero, and the d-component becoming the magnitude of the output voltage.

The performance of power control and synchronization during the different stages of operation is elaborated in the next section.

3.1.1 Achieving synchronized operation if connecting to external generation

If the system to be energized by MMC is fully blacked out (i.e., no ac sources present), the power control function is disabled, because the power delivered is only a function of applied voltage magnitude. Therefore, $\Delta\omega$ is set to zero, and the power control and synchronization output angle θ is equal to $2\pi f_0 t$.

If MMC is connected to a local generation or to a remote network, a synchronized closing of the circuit breaker CB is required. This requires that the network side voltage V_{net} and MMC side voltage V_{POC} be equal in magnitude and phase. This eliminates undesired transients and high currents from the circuit breaker's closing which could damage the converter valves. Once the two voltages become equal, indicated by the error between voltage magnitudes (ΔV), frequencies (Δf) and phase angles ($\Delta\theta$) becoming less than the threshold, a closing command is sent to the CB and the two systems are synchronized.

Magnitude Adjustment: The reference voltage magnitude V_{ref} in Figure 3.1 is set to equal the measured network side voltage magnitude, V_{net}.

Phase Adjustment: The grayed area in Figure 3.2 is responsible for phase adjustment. Prior to the closing of CB, ΔP_{syn}, increases or decreases the reference power which results in adjusting $\Delta\omega$ so that the converter and network side voltages are aligned (V_{dPOC} with V_{dnet}, and V_{qPOC} with V_{qnet}) as shown in Figure 3.3a, which results in the angle θ aligning with the instantaneous angle of the network side voltage. Using this θ as the reference angle in the d-q transformation results in the q-component of the POC voltage becoming zero. When the magnitude and phase are equalized, the circuit breaker CB can be closed.

After closing CB, further control of real power to the network is accomplished by changing the reference power, P_{ref}. The angle θ is now controlled by the power error (= P_{ref}

– P_{POC}). If a droop characteristic is desired, for example when operating with other nearby generators, a frequency droop can be added to the power reference.

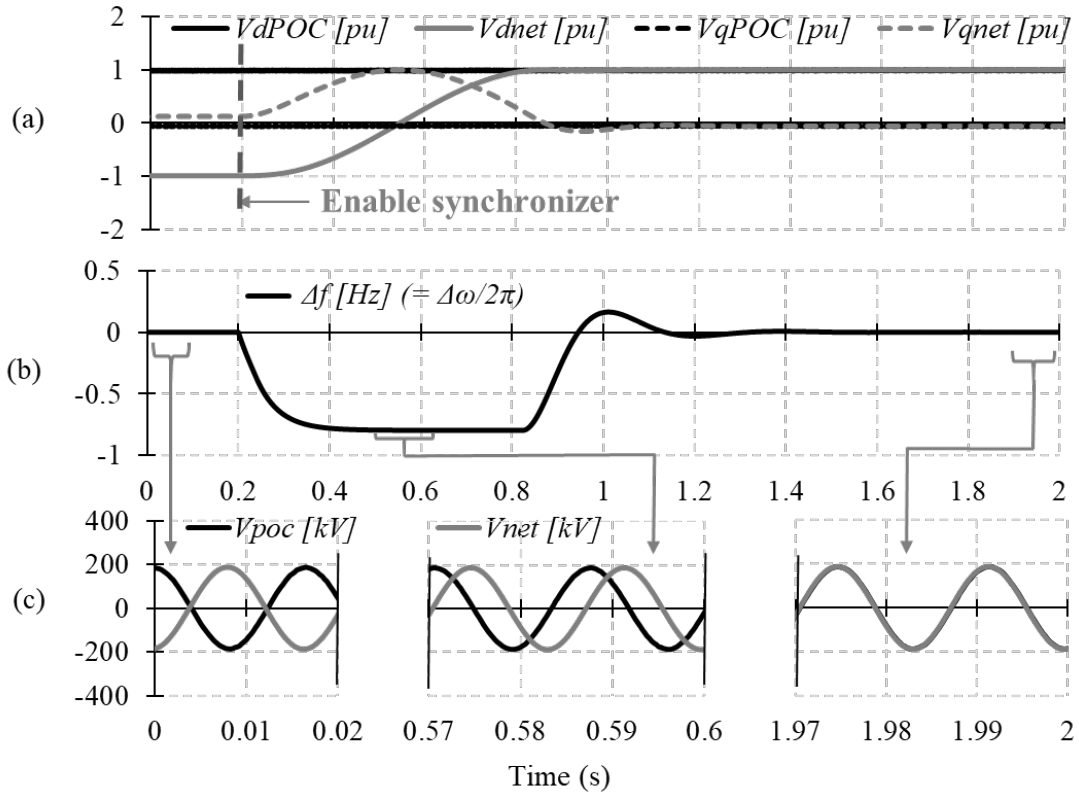

Figure 3.3: Operation of synchronizer. (a) V_{dnet}, V_{qnet}, V_{dPOC} and V_{qPOC} are the *dq*-component of the voltage measured at the network side and POC side of the circuit breaker respectively (b) Output of power control and synchronization ($\Delta\omega$) (c) Phase "a" voltages of CB's POC and network side voltage.

3.2 Voltage Control with Current Limiting

Figure 3.4 illustrates the simplified MMC connection with its interface transformer. *L* is the total series inductance on MMC side, i.e, the sum of the equivalent arm inductance and the leakage impedance in the interface transformer.

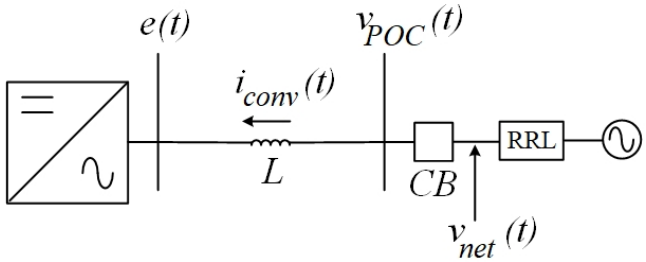

Figure 3.4: Simplified MMC interfaced to network.

If current limiting is not required, then the voltage order, $V_{dref,}$ from the upper level control as in Figure 3.1, and θ from the power control and synchronization can be used to generate the reference voltage waveform for MMC. However, with this, during faults or other conditions, there is no mechanism to limit the current. Hence, the dual controller in Figure 3.1 is proposed and used in this thesis, which consists of a voltage control block followed by a decoupled current control block, whose purpose is to limit the overcurrent in the converter. The voltage control loop is first presented below, after which the current control loop will be presented.

3.2.1 Voltage Control Loop

The voltage control loop is introduced to generate the *dq*-reference currents from the voltage references V_{dref} and V_{qref} (= 0) as shown in Figure 3.5. It outputs the *dq*-components of the reference current for the decoupled current control block that follows. A proportional integral (PI) control block adjusts I_{dref} and I_{qref} outputs in a manner to make the measured and reference voltages equal. The current limit ensures that these values do not exceed their maxima. The angle θ from the power control and synchronization is used in the *d*-*q* transformation. Note, as mentioned earlier, the *q*-component of the grid voltage is controlled to zero.

3.2.2 Decoupled Current Control Loop

The current loop is as reported earlier in [61][62], and depicted in the shaded region in Figure 3.5. The highlighted decoupled current control loop accepts the *d*- and *q*-axis references from the preceding voltage controller. If the current order from the voltage controller exceed the maximum current ceiling, the current limiting function reduces the reference currents and ensures that the current only attains the ceiling value. In this thesis, the current is limited to the ceiling I_{max}, whereas the phase angle φ of the original current references is maintained. However, other mechanisms where either $I_{drefmax}$ or $I_{qrefmax}$ is selected differently can be incorporated if so desired. The *dq*-components of internal voltages, $\boldsymbol{E_{dq}}$, are derived by compensating for the series impedance drop across the total

MMC side inductance, L, as in (11). $\boldsymbol{V_{dqPOC}}$ and $\boldsymbol{I_{dqconv}}$ are the dq-components of POC voltage and converter side currents respectively [61][62].

$$E_d = V_{dPOC} - \omega L I_{qconv} - V_d'$$
$$E_q = V_{qPOC} + \omega L I_{dconv} - V_q' \tag{11}$$

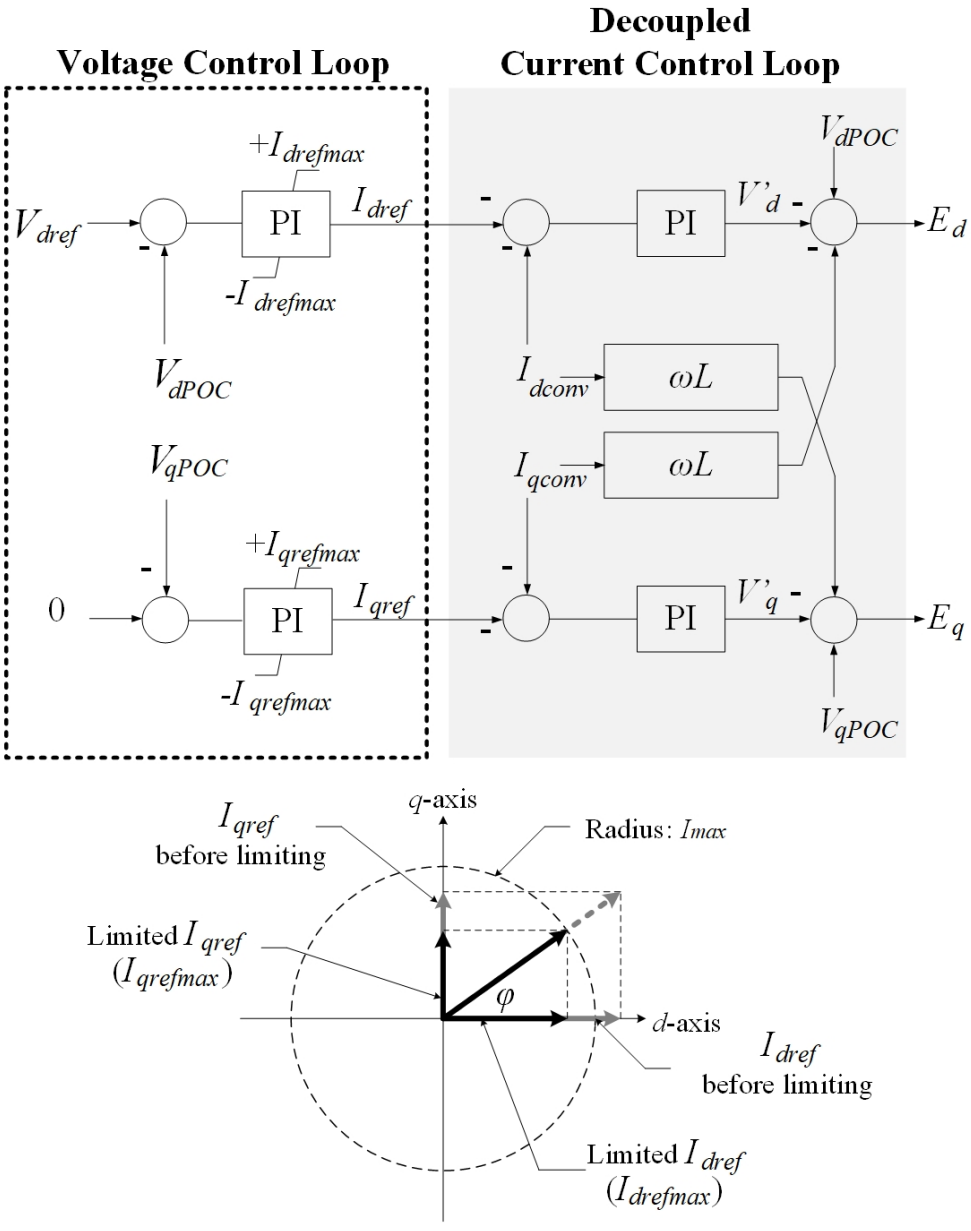

Figure 3.5: The proposed dual control for current limiting block diagram. Here I_{dconv}, I_{qconv}, V_{dPOC} and V_{qPOC} are the valve side currents and the POC voltages in dq-reference frame. I_{max} is the valve side maximum current.

3.3 Initial EMT Simulation Study

Figure 3.6 shows a simple test case developed to demonstrate the grid-forming control approach, and power control and synchronization loop discussed above. The MMC link is connected to an external source (SCMVA = 200 MVA) through circuit breaker CB. Table 3.1 summarizes the MMC link specifications.

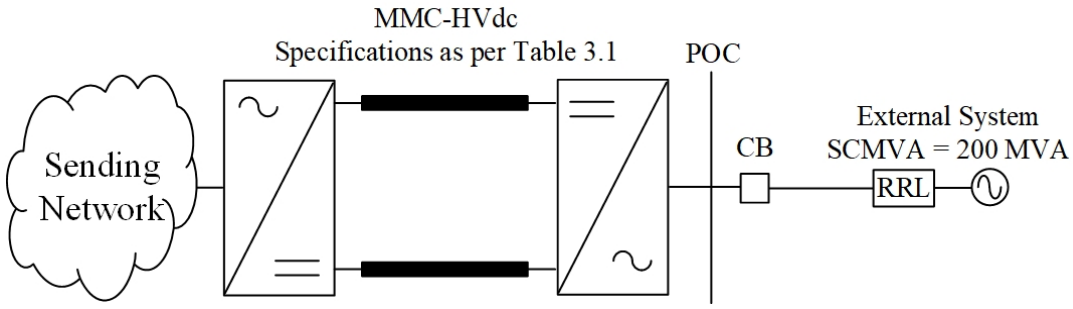

Figure 3.6: Simple test system schematic

Table 3.1: Simple test system specification

MMC-HVdc link	200 MW, ±120 kV, 250 km transmission line, symmetrical monopole Rectifier control mode: V_{dc}, V_{ac} Inverter control mode: as describe in section 3.1 and 3.2 Transformer valve side rated current: 1.5 kApk Transformer magnetizing current: 1%
External network	SCMVA = 200 MVA, 230 kV, 60 Hz

3.3.1 Synchronizing Control with Current Limiting

Figure 3.7 shows waveforms for the simple test case depicted in Figure 3.6. Initially CB is open, the converter de-blocks at t = 1 sec, the synchronizer is enabled at t = 7 sec, a step change in power to 30 MW is applied at t = 10 sec (Figure 3.7a), a step change in ac voltage reference is applied at t = 12 sec, and another step change in power to 50 MW is applied at t = 15 sec.

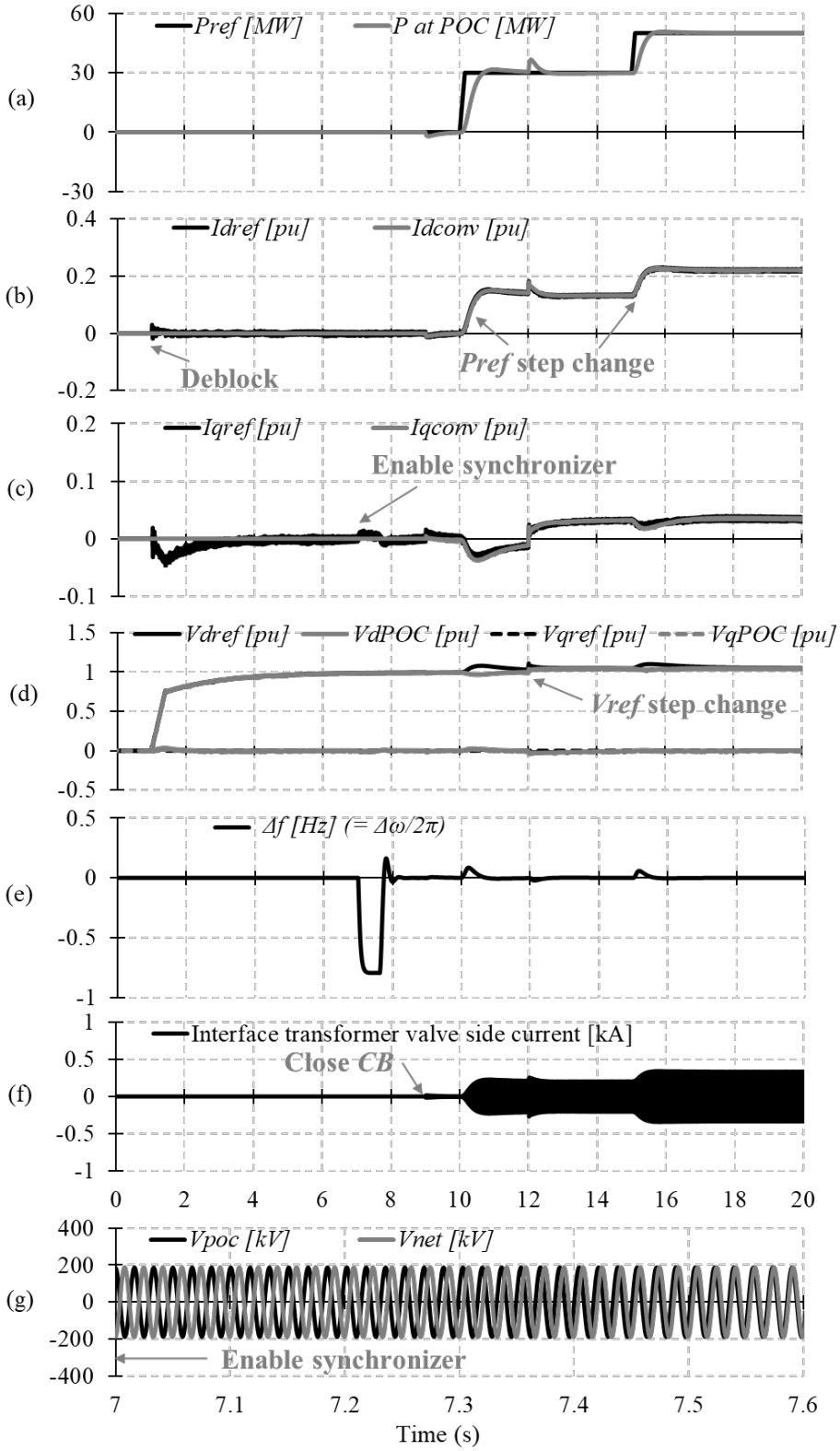

Figure 3.7: The dual loop control response. (a) Reference power and measured power at POC (b & c) *Dq*-component of reference current and converter side current (d) *Dq*-component of reference voltage and POC voltage (e) Output of power control and synchronization ($\Delta\omega$) (f) Instantaneous current at the converter side (f) Phase "a" voltages of CB's POC and network side voltage

3.3.1.1 Voltage Regulation with Open Circuit Breaker

What does it mean to have current control with an open breaker if the current controller is always in operation? It will be shown that the proposed scheme automatically results in a zero current order for I_d and I_q under the open breaker condition. Therefore, no special feature is required to bypass the current controller during this situation.

With the CB open and power order at zero, the converter is de-blocked (t = 1 sec) and produces a voltage V_{POC} on MMC side of CB. The magnitude of V_{POC} is controlled by the upper level controller voltage as mentioned in Section 3.1 and 3.2, to be equal to the network side voltage (Figure 3.7d). In case, there is no network side voltage (i.e. dead load), V_{ref} will be set to the desired voltage reference. At t = 7 sec, the synchronizer is enabled as discussed and successfully equalizes the phase angles on either side of CB, as is evidence by the plot of phase "a" voltages (Figure 3.7g). Since the CB is open, the current flowing through the converter is zero. The PI controller in the voltage control loop adjusts I_{dref} and I_{qref} so that the POC voltage on MMC side reaches its reference. The controller actions automatically result in the PI blocks of the current controller having inputs I_{dref} and I_{qref} becoming zero (Figure 3.7b and Figure 3.7c). This causes the current controller outputs E_d and E_q to become constant, which are the references for the internal MMC generated voltage. Due to zero current, E_d and E_q are also MMC side voltages, V_d and V_q, which achieve their magnitudes of 1 and 0 per-unit respectively (Figure 3.7d).

3.3.1.2 Synchronized Operation after Breaker Closing

Circuit breaker CB is closed at t = 9 sec, and the current remains at zero (Figure 3.7f). The voltage reference V_{ref} is adjusted to 1 per-unit and the power order is ramped to 30 MW at the rate of 200 MW/s (Figure 3.7d). $\Delta\omega$ is adjusted by the power control and synchronization to allow transferring of 30 MW power to the external system (Figure 3.7e). The dual loop controller ensures that V_{POC} regulates to its reference value of 1 per-unit (Figure 3.7d). At t = 12 sec, V_{ref} is changed to 1.05 per-unit to demonstrate the response of the voltage control loop. The d-axis controls V_d to the new reference value. I_{qref} automatically increases to inject reactive power to maintain V_q at zero. Finally, P_{ref} is

ramped form 30 MW to 50 MW at t = 15 sec. I_{dref} and I_{qref} settle at new values to meet this new power flow.

3.3.1.3 Reason for Synchronizer

Figure 3.8 shows how the synchronizer is useful. If an attempt is made to close breaker CB at t = 0.1 sec without any effort at equalizing the voltages across the breaker (Figure 3.8a-i), on closing CB, there is an excessive overcurrent peak of 19 kA (Figure 3.8a-ii), which exceeds the transformer valve side rated current of 1.5 kA by a factor of 12. When the synchronizer is activated, it automatically brings the voltage across the open breaker to zero (Figure 3.8b-i). The subsequent closing of the breaker results in a smooth synchronization with essentially zero current (Figure 3.8b-ii).

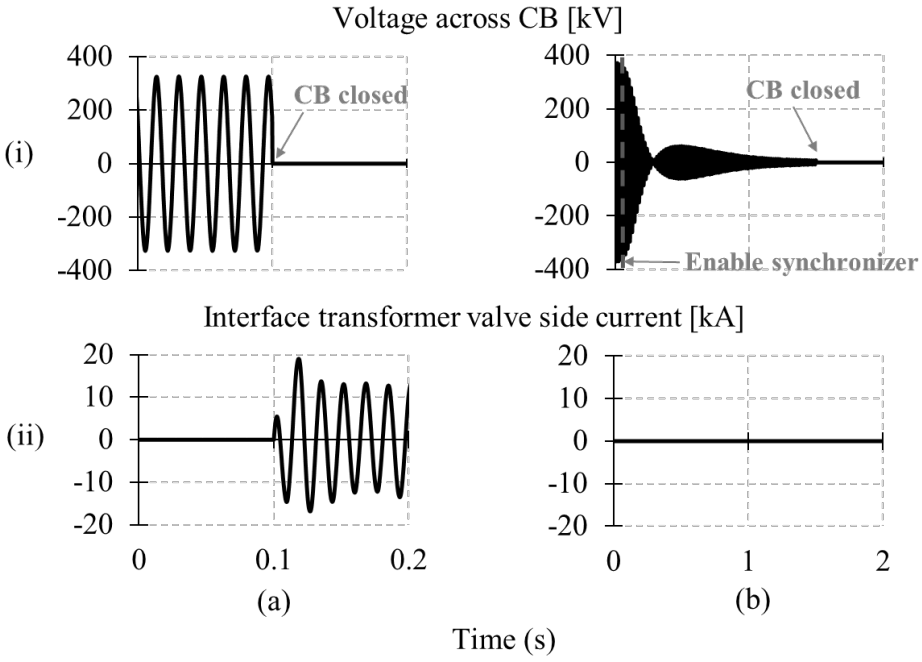

Figure 3.8: Closing circuit breaker a) without Synchronizer b) with Synchronizer. Voltage across CB (top), and valve side current (bottom)

3.3.2 Operation in the event of Frequency Change

The power control and synchronization loop allows the inverter to operate in the manner of a synchronous machine, which automatically adjusts its “internal voltage” and

"phase angle" to the network conditions without the requirement of an external synchronizing element such as a PLL. Figure 3.9 shows the response of the power control and synchronization loop to the frequency step change.

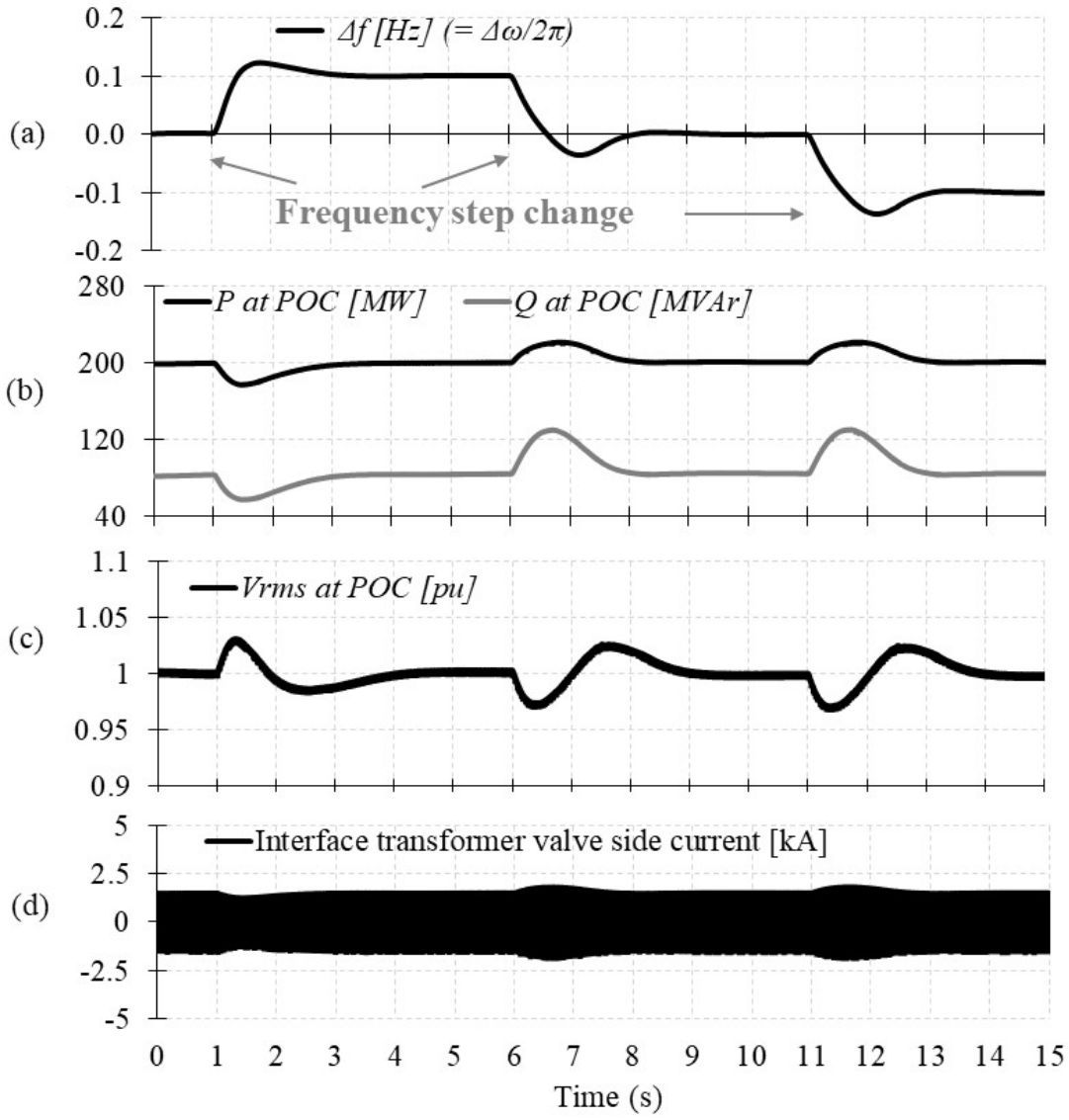

Figure 3.9: Response of power control and synchronization loop to a system frequency step change (a) System frequency deviation (b) Measured active and reactive power at POC (b) RMS voltage at POC (V_{base} = 230 kV) (d) Instantaneous current at the converter side.

A t = 1 sec, 6 sec and 11 sec, the frequency is changed to 60.1 Hz, 60 Hz and 59.9 Hz respectively to demonstrate the response of the power control and synchronization loop. The output of power control and synchronization, $\Delta\omega$, is automatically adjusted to allow for change in frequency (Figure 3.9a). The initial transient change in power is

because of change in frequency. The power controller ensures that the inverter output power regulates to its original reference value of 200 MW (Figure 3.9b). The dual loop controller ensures that V_{POC} regulates to its reference value of 1 per-unit (Figure 3.9c and Figure 3.9d).

3.3.3 Operation in the event of Reference Power Change

Figure 3.10 shows the response of power control and synchronization loop to the power change.

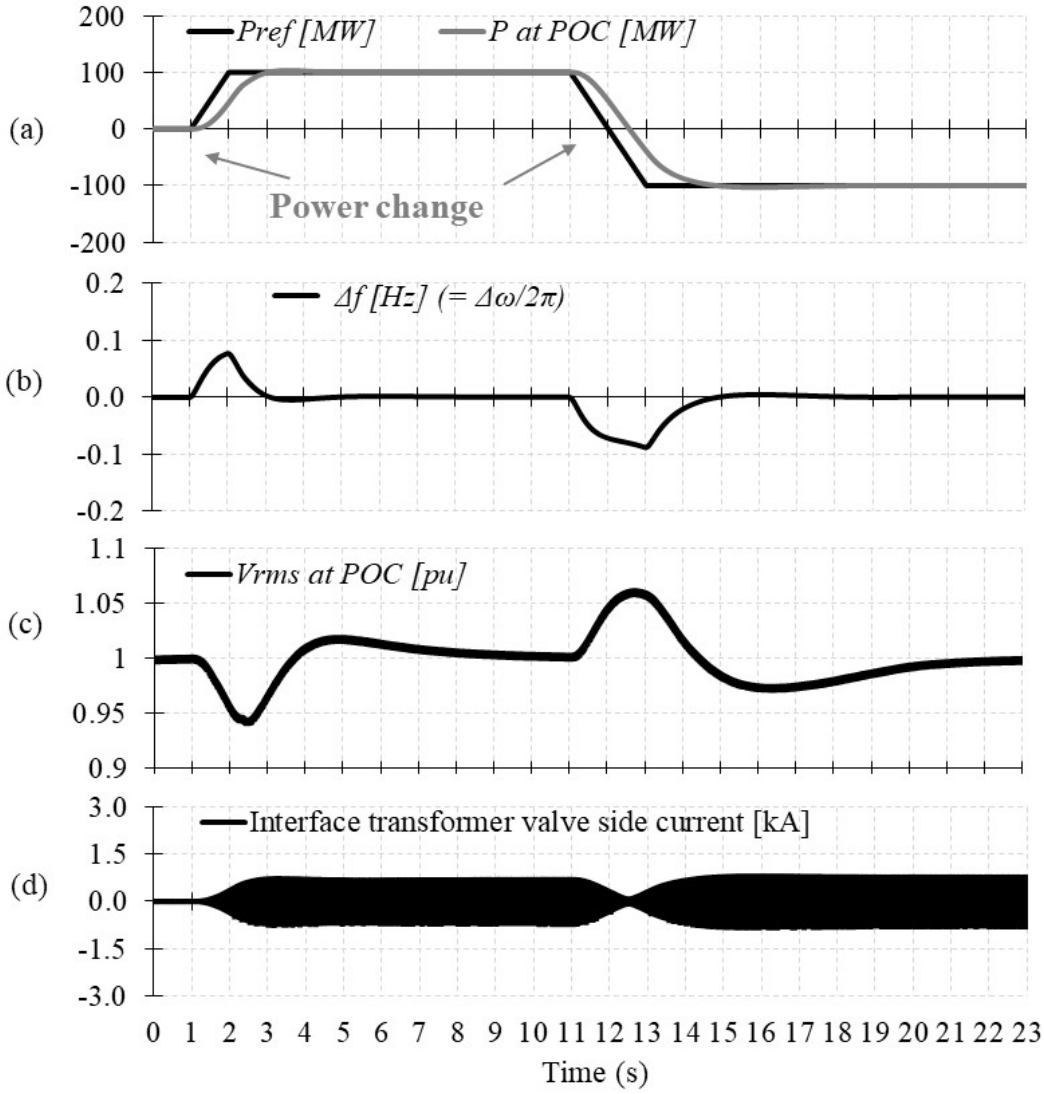

Figure 3.10: Response of power control and synchronization loop to a power change
(a) Reference and measured active power at POC (b) System frequency deviation (b) RMS voltage at POC (V_{base} = 230 kV) (d) Instantaneous current at the converter side.

A t = 1 sec and 11 sec, the power order is ramped to 100 MW and -100 MW respectively at the rate of 100 MW/s (Figure 3.10a). The ramp rate is selected such that V_{POC} remains in 0.95 – 1.05 per-unit range, and also prevents 200 MVA system from any voltage collapse. The inverter adjusts its internal phase angle (Figure 3.10b) to allow for change in power. The dual loop controller ensures that V_{POC} regulates to its reference value of 1 per-unit (Figure 3.10c and Figure 3.10d).

3.3.4 Fault Ride-Through

To investigate worst-case fault recovery, single- and three-phase faults are applied at the inverter bus with MMC under full-load conditions. The fault duration is set to 120 ms to capture the worst-case dynamic performance as per certain grid codes [67]. Figure 3.11 and Figure 3.12 show the dynamic response of the proposed grid-forming control to a three-phase and single-phase to ground fault at t = 0.1 sec respectively.

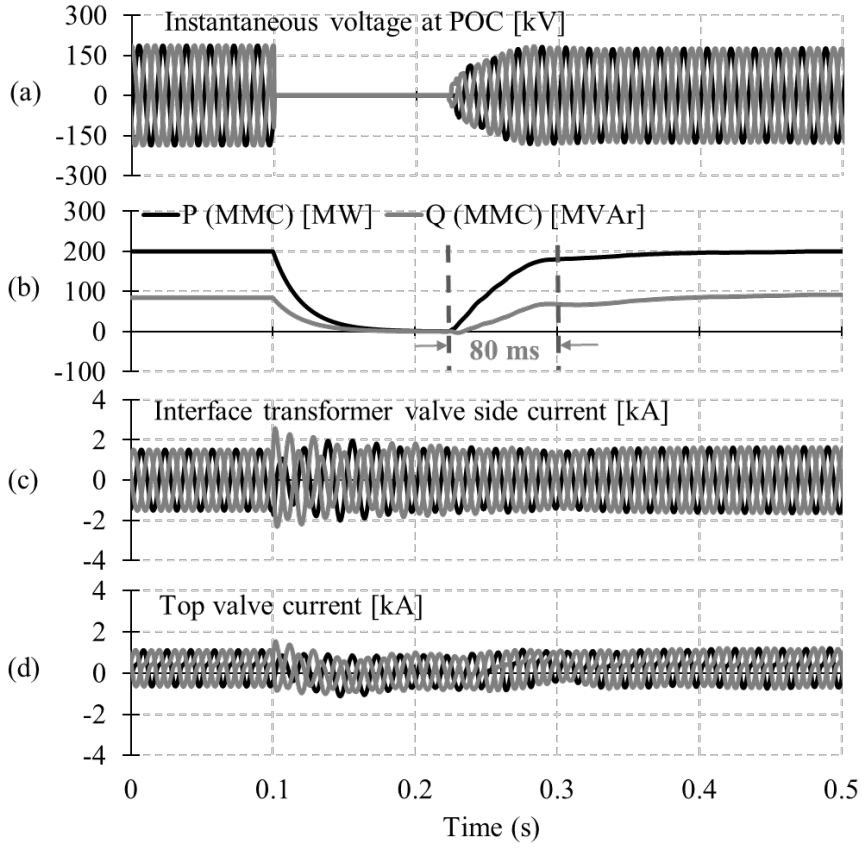

Figure 3.11: Results of a three-phase to ground fault

During the fault, the valve current is successfully limited by the current controller loops to 1.65 kA. After the fault clearance, the recovery is successful and 90% power is achieved in 80 ms and 60 ms for the three-phase and single-phase faults respectively.

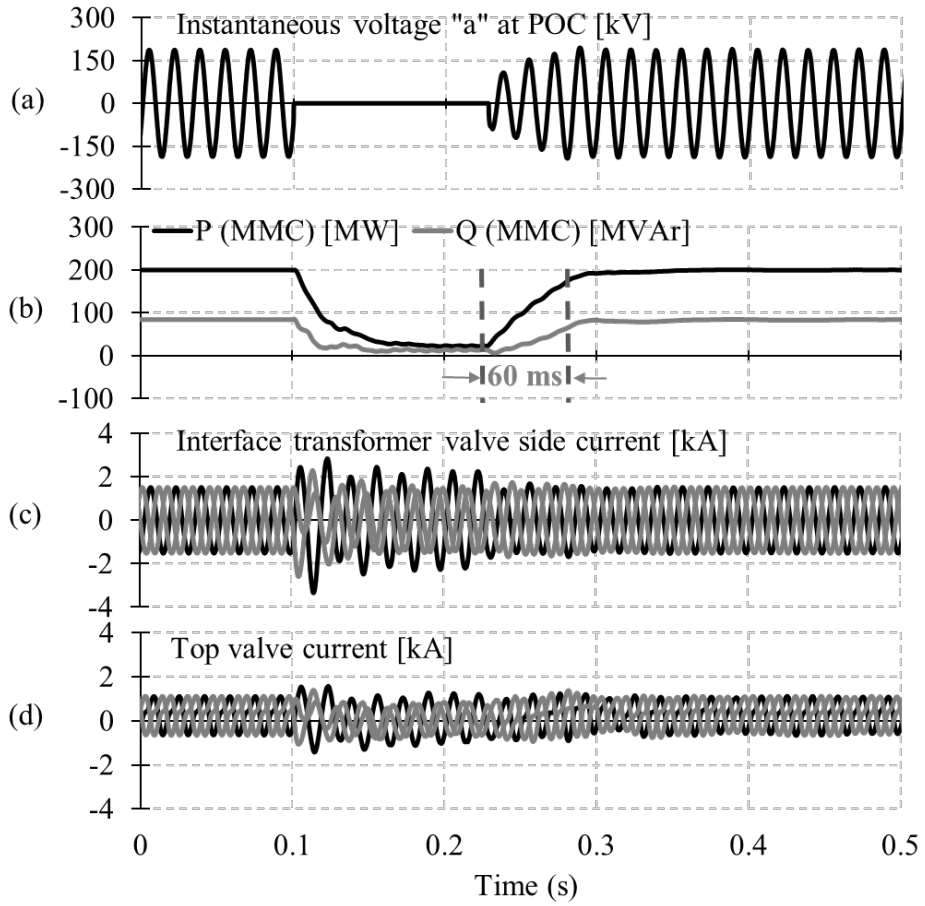

Figure 3.12: Results of a single-phase to ground fault

3.3.5 Impact of Ac Network Short Circuit MVA

The aim of this section is to demonstrate the effectiveness of proposed method under various network short circuit MVA (SCMVA) levels. Initially, the control method proposed in section 3.1 and 3.2 are tuned for the test system described in section 3.3, i.e., SCMVA = 200 MVA, P_{rated} = 200 MW. For this system, the 200 MVA level is given as the lowest MVA into which the converter is expected to operate. Without changing any control parameters, e.g. gain, time constant, ramp rates, etc., the control response is tested

for a power reference change from 0 to 200 MW for SCMVA of 200 MVA to 700 MVA with a power ramp rate of 100 MW/s.

Surprisingly, as the SCMVA increases beyond 600 MVA, the performance deteriorates with the initial control gains as shown in Figure 3.13. As SCMVA increases, the control response becomes less damped which causes I_{dref} to saturate to I_{max} (Figure 3.13c) due to the current limiting necessary to protect IGBT values. This causes the POC voltage to drop to 0.6 per-unit (Figure 3.13b). Although, the system recovers at t = 9 sec, there is a full power reversal from t = 5 sec to 9 sec which is not desired.

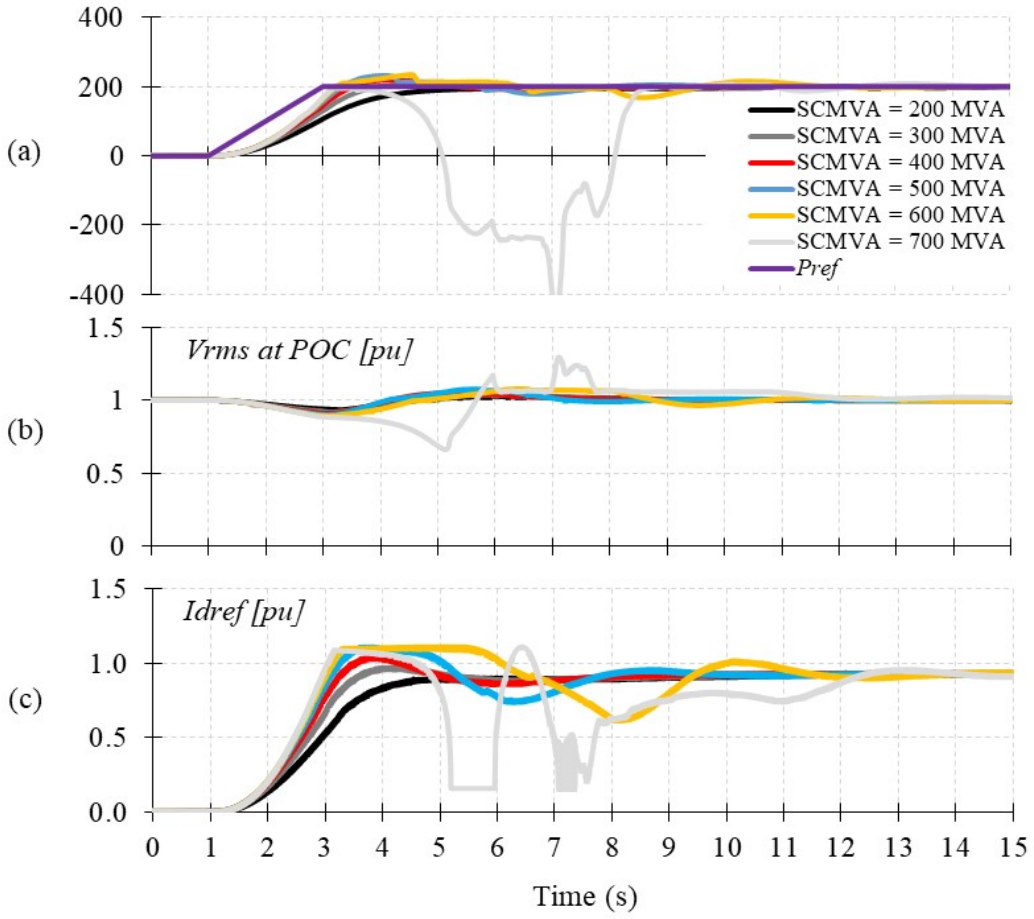

Figure 3.13: Impact of network SCMVA on proposed grid-forming method, ramp rate = 100 MW/s

One solution is to allow the control parameters change automatically when operating in a higher SCMVA. Reference [73] discusses this approach, but shows that

detecting a change in SCMVA on-line is challenging and may take up to several cycles. The system could go unstable in the meantime, so this is not recommended. Alternatively [73] also shows that the breaker status signals in the SCADA system can quickly be used to estimate the SCR, but the sudden change of gains itself can introduce an undesirable transient. An easier alternative to change the gains dynamically is to reduce the power ramp rate, and to prevent excessive overshoot during full power change (form 0 to 200 MW). Figure 3.14 shows the response for SCMVA of 600 MVA to 1000 MVA for a ramp rate of 50 MW/s. It shows a successful operation without any stability issue.

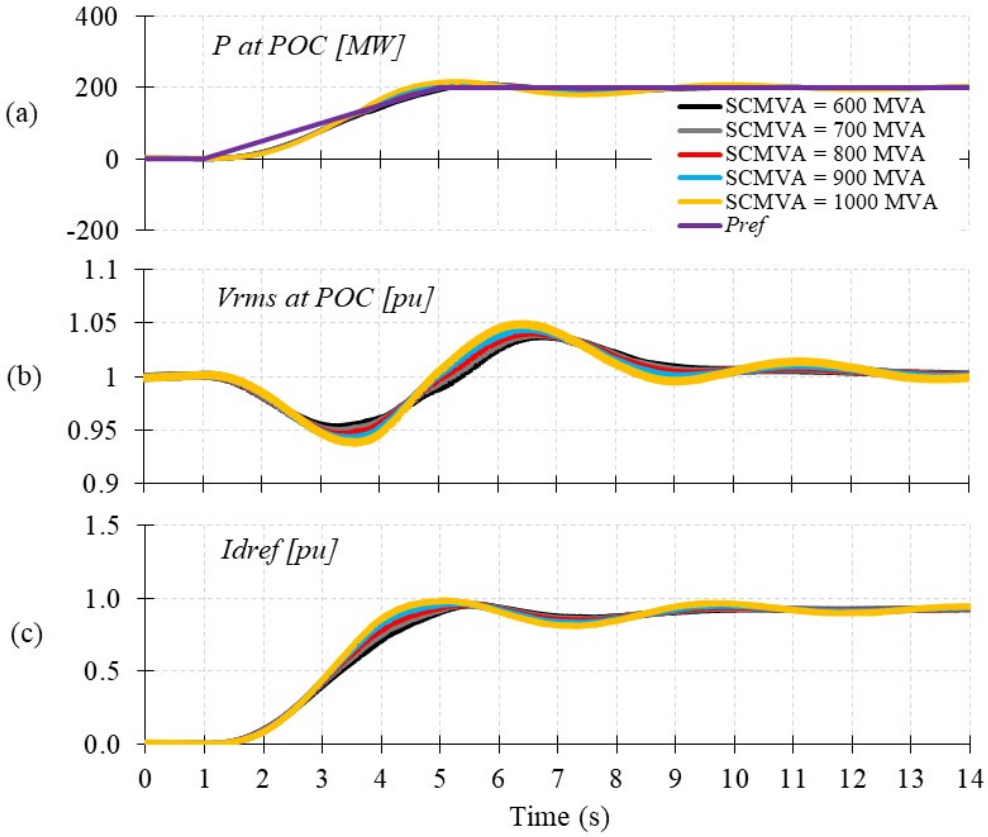

Figure 3.14: Impact of network SCMVA on proposed grid-forming method, ramp rate = 50 MW/s

Finally, the VSC can continue its normal operation in a system whose structure and operating point changes unpredictably, including going from a grid-following scenario to an islanded scenario. For instance, it is possible that the VSC becomes disconnected from the network, which can result in an islanded system with only local loads.

Assume that the MMC, shown in Figure 3.15 is operating in grid-forming under full-load conditions and connected to the external system (SCMVA = 1000 MVA) and a 50 MW local load connected to POC.

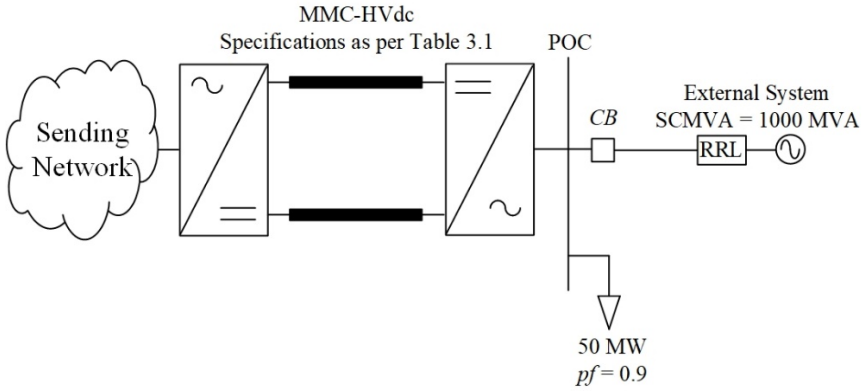

Figure 3.15: Simple test system schematic

The circuit breaker CB is opened at t = 0.2 sec (Figure 3.16a) and reject 150 MW power transfer to the external system. After opening circuit breaker CB, VSC continues operating in the grid-forming mode and supplies the local load (Figure 3.16a through Figure 3.16c).

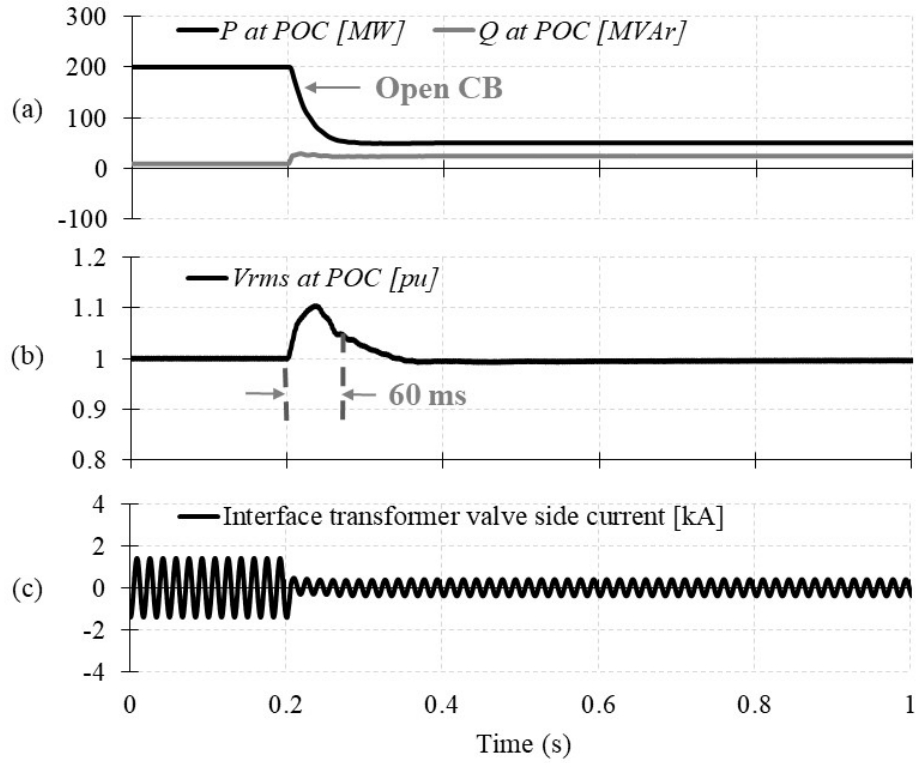

Figure 3.16: Response of proposed grid-forming control when disconnecting from the external source

3.3.6 Analysis of Anomalous Behavior in Strong Systems

Traditional HVdc control (i.e., grid-following converter) demonstrates less stability problems at higher SCR values. In contrast, as shown by Figure 3.13, the grid-forming converter shows surprisingly poorer performance for the higher SCRs. To analyze this further, an eigenvalue analysis is performed on a simplified representation shown in Figure 3.17.

A state-space equation of the MMC-HVdc system is derived, which considers the power synchronization and control dynamics, the dual control system, and the dynamics of the ac network. Figure 3.17a shows the full MMC inverter representation in this section and Figure 3.17b shows its equivalent circuit used for developing the small-signal model. The ac source is modeled as a Thévenin impedance consisting of R_s and L_s. The MMC side is modeled by the total inductance, L, and a source v_c representing the MMC's internal voltage. The control block diagrams discussed in section 3.1and 3.2 are used for the small-signal model.

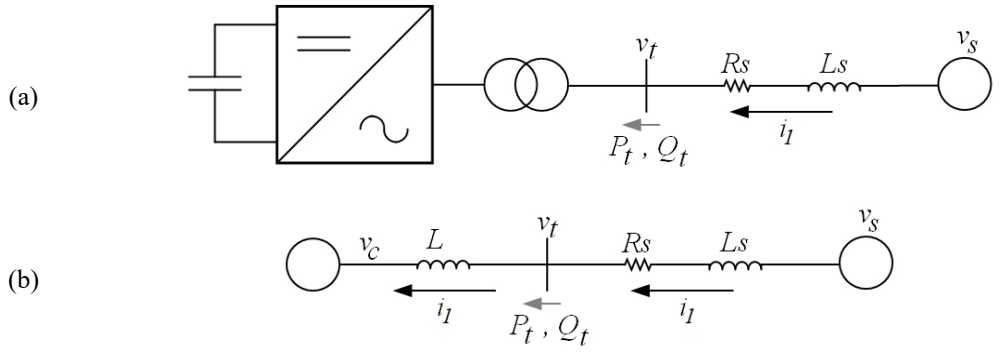

Figure 3.17: Simplified system for eigenvalue analysis (a) Full MMC inverter representation (b) The equivalent circuit for small-signal analysis

3.3.6.1 State-Space Model

In order to develop the small-signal state-space equations for the system, the equations must first be linearized around the operating point. The operating point is V_t = 1.0 p.u. ac voltage and P_t = 1.0 p.u. dc power. This will yield the state-space model of the complete MMC system in the form of (12).

$$\Delta \dot{\boldsymbol{X}} = \boldsymbol{A} \cdot \Delta \boldsymbol{X} + \boldsymbol{B} \cdot \Delta \boldsymbol{U} \tag{12}$$

Here, the state vector is with 11 control state variables and 2 ac network variables. The input variable is $\boldsymbol{\Delta U} = [\Delta P_{ref}\, \Delta V_{reff}]^T$. The $\boldsymbol{A}$ and $\boldsymbol{B}$ matrices as well as the elements of the state vector $\boldsymbol{\Delta X}$ are derived in Appendix A. The derivation of the state-variable equations is given in section A.1 through A.5 of the Appendix A.

3.3.6.2 Model Analysis and Validation

The system shown in Figure 3.17b is used for the analysis and validation. For validation, the small-signal model results are compared with those obtained from an EMT model where the full MMC is represented in detail.

The system parameters used for model validation are shown in Table 3.2, and the control parameters are summarized in Table 3.3. All parameters are in per-unit, with interface transformer rated voltage and MVA as base.

Table 3.2: System parameters for model verification

Equivalent ac source magnitude	1.0 p.u., 60 Hz
Equivalent ac system SCMVA	Ranging from 200 MVA to 1000 MVA
Ac system impedance angle	80°
Terminal voltage (V_t)	1.0 p.u. at 0°
Total MMC reactance	0.197 p.u.

Table 3.3: Optimized gains for the control parameters

Upper loop controller gains (K_{pAC}, K_{iAC})	(2.5, 10)
Voltage loop controller gains ($K_{pvd} = K_{pvq}$, $K_{ivd} = K_{ivq}$)	(1.0, 10)
Current loop controller gains ($K_{pid} = K_{piq}$, $K_{iid} = K_{iiq}$)	(0.8, 10)
Power synchronization and control loop gains (J, D)	(0.04, 1.0)

In order to validate the small-signal model, the time-domain response of the small-signal model is calculated using MATLAB and compared with the time-domain response of the full non-linear model simulated using EMT program. A few sample results of the transients in active power (P_t) following set point changes are shown in Figure 3.18. The simulations are for SCMVA = 500 MVA and 750 MVA. The results show that the small-signal model is highly accurate as the two traces are essentially identical. The calculated eigenvalues are also consistent with the results from EMT simulations. The simulated plot in Figure 3.18b shows a period of oscillation of 1.18 s. This is in complete agreement with the period derived from the natural frequency of the dominant mode of $(-0.6 \pm j5.3)$ from small-signal analysis, for which the period is also 1.18 s ($= 2\pi/5.3$). Likewise, the decay rate of the amplitude is also consistent with the real part of the dominant eigenvalue.

(a)

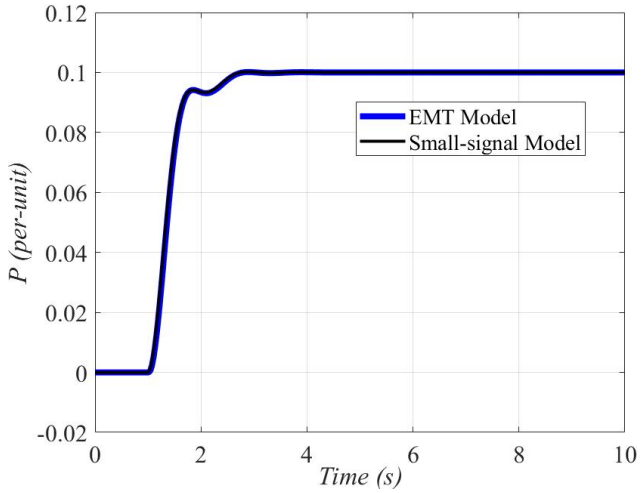

(b)

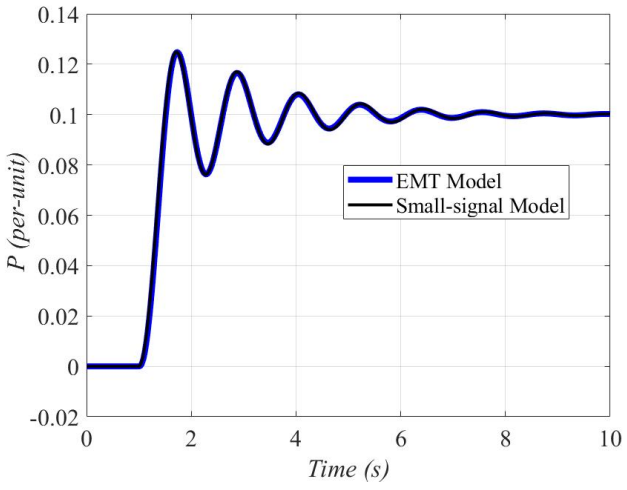

Figure 3.18: Comparing small-signal model with detail EMT simulation for (a) SCMVA = 500 MVA (b) SCMVA = 750 MVA

3.3.6.3 Impact of SCMVA on the Stability of Grid-forming Control

The locus of dominant eigenvalues of the P_t = 1.0 p.u. operating point for the system SCMVAs ranging from 200 MVA to 1000 MVA is shown in Figure 3.19. For SCMVA of 905 MVA, the system is stable. However, when the SCMVA is increased to 910 MVA, the system becomes unstable. The plots clearly show that the system becomes more underdamped as the SCMVA increases, and eventually becomes unstable for SCMVA = 910 MVA. This is opposite to the situation for grid-following converters where the stability margin is better for high SCRs [21]. The eigenvalues of the P_t = 1.0 p.u. operating point for ac system SCMVA of 905 MVA and 910 MVA are listed in Table 3.4. The dominant oscillatory eigenvalues for each case are highlighted in gray in this table.

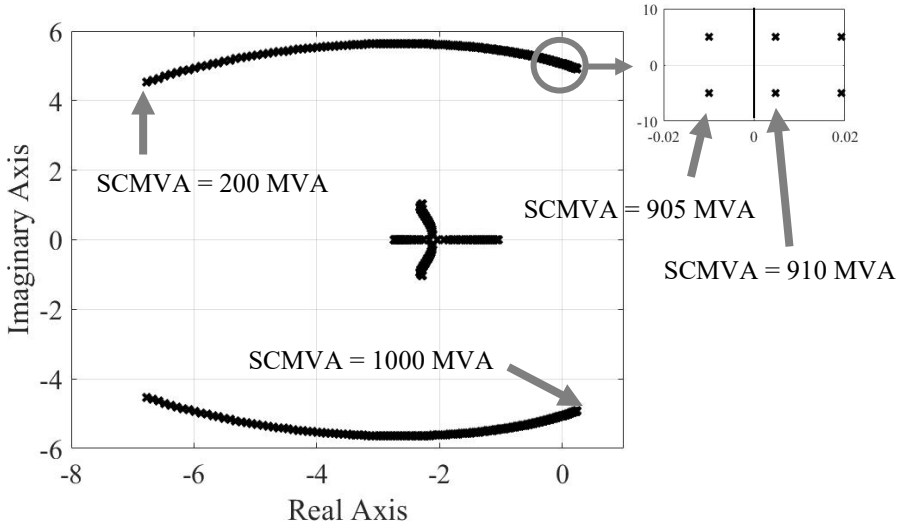

Figure 3.19: Locus of dominant eigenvalues for the grid-forming MMC

Table 3.4: Eigenvalues of the test system for P_t = 1.0 p.u. operating point

SCMVA = 905 MVA	SCMVA = 910 MVA
– 9289.68	– 9275.5
– 3366.8	– 3364.2
– 5000.0	– 5000.0
– 5000.0	– 5000.0
– 1031.1	– 1036.0
– 550.5	– 551.2
– 24.8	– 24.8
– 0.01 ± *j* 5.064	0.005 ± *j* 5.057
– 2.293 ± *j* 1.007	– 2.292 ± *j* 1.009
– 12.604 ± *j* 0.006	– 12.604 ± *j* 0.006

3.3.7 Transition from Grid-forming to Grid-following Mode

The convertor control mechanism described above and shown in Figure 3.2 and Figure 3.5 is perfectly capable of connecting into a strong network. However, network protocols may require traditional PLL based grid-following operation when operating into a strong ac network. In that case, the grid-forming control will only be initiated in islanded operation or operation into very weak ac networks. This section shows that it is possible to seamlessly transition between modes if required.

In grid-following mode, a PLL is used to synchronize the VSC's operation to the ac busbar voltage. Once the control transition is enabled, the seamless transfer ensures that the output of a PLL, θ_{PLL}, tracks the output of power control and synchronization block to avoid any severe disturbance. A seamless transfer block is shown in Figure 3.20. The gain, K, is selected to allow for a seamless transfer.

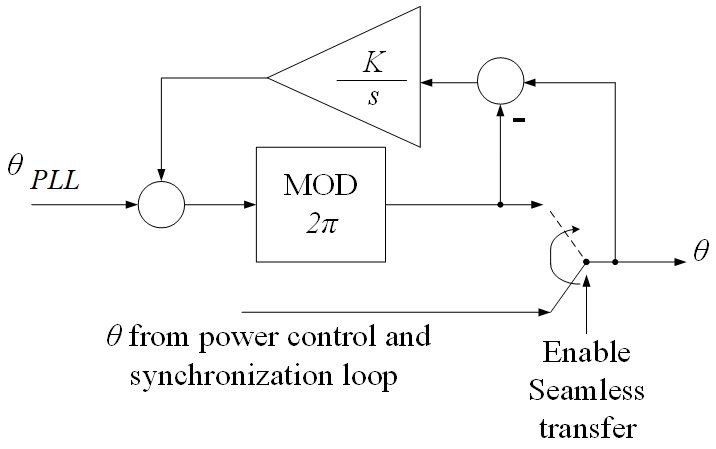

Figure 3.20: Seamless transfer block diagram

Assume that the external system short-circuit MVA (SCMVA) changes from 200 MVA to 400 MVA at t = 0.1 (Figure 3.21a and Figure 3.21b) due to the closing of a breaker which connects to another system. This result in a voltage dip prior to enabling the control transition as shown in Figure 3.21a through Figure 3.21c. The seamless transfer is enabled at t = 0.3 sec after closing the circuit breaker, which successfully equalizes the reference angles as is evidenced by Figure 3.21d. Finally, a control transition from grid-

forming to grid-following occurs at $t = 0.315$ sec. After the control transition occurs, VSC continues its operation in the grid-following mode as shown in Figure 3.21.

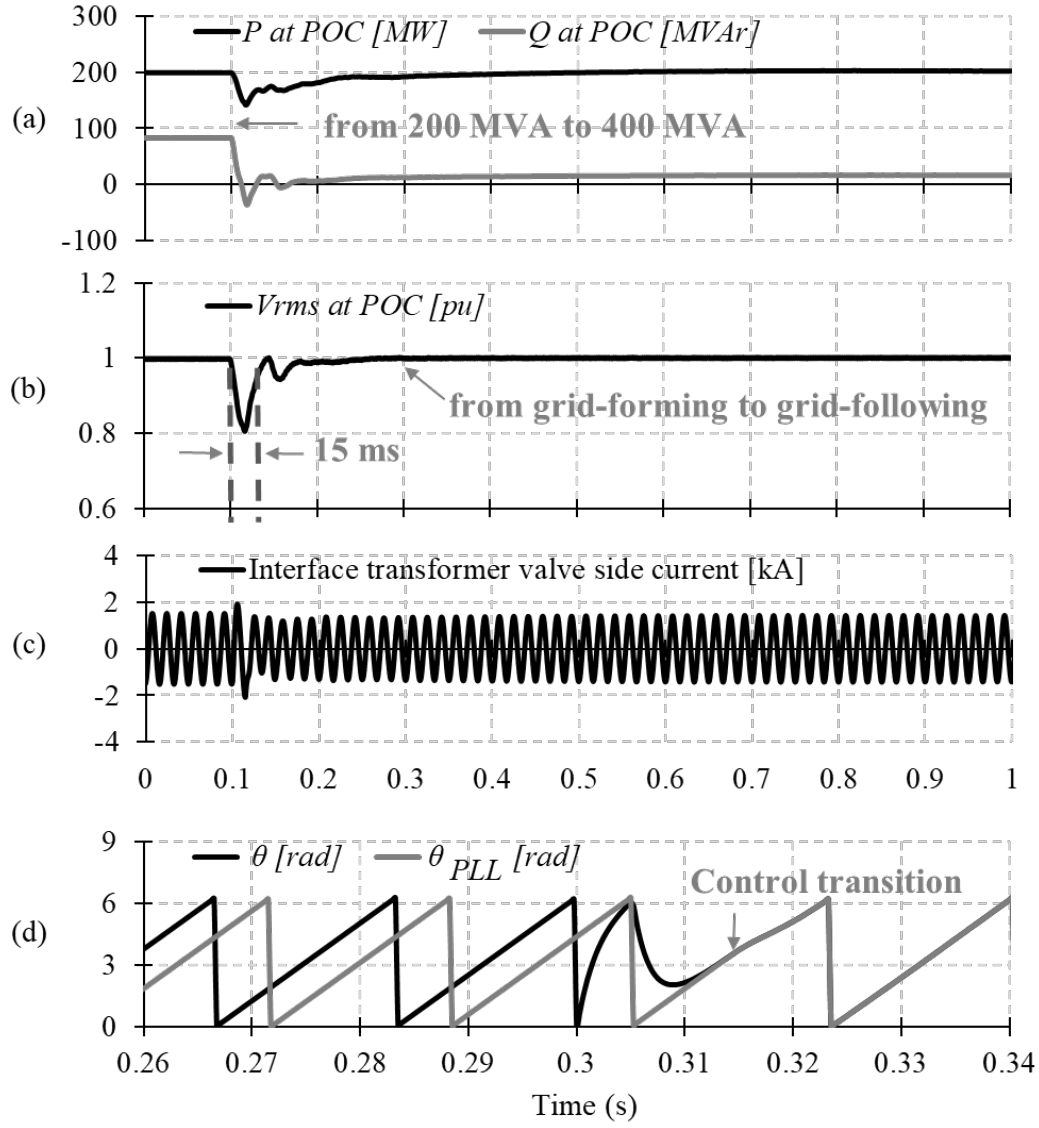

Figure 3.21: Results of control transition from grid-forming to grid-following mode

3.4 Chapter Concluding Remarks

Chapter 3 presents a novel grid-forming control methodology for black start restoration and operation in a very weak system with fault ride-through capability. A dual voltage and current control approach is proposed to prevent overcurrent in the MMC-HVdc converter. An improved synchronization approach is developed for black starting a weak network. The proposed method is implemented via a power synchronizer that automatically aligns the phase angle and the magnitude of voltages on both sides of the circuit breaker before closing to eliminate any excessive current flow. A simple test case is developed to demonstrate the control approach and the power control and synchronization loop. A series of EMT simulation tests are performed to examine the proposed method during black start and faults. The impact of network SCMVA on the proposed grid-forming method is also investigated, including change of the system configuration from a grid-following to an islanded system. It is also shown that if required, seamless transition from grid-forming to grid-following is possible. The next chapter compares the proposed grid-forming method with existing grid-forming with current limiting capability and describes the implemented optimization method for tuning the control parameters.

Chapter 4

Introducing Control Optimization and Comparing Different Current Limiting Methods

Chapter 3 described a new grid-forming methodology, and examined the control performance through a simple test case. As discussed in previous chapters, the MMC valve current cannot exceed its rated value during the disturbances. Therefore, it is critical to implement a current limiting function to protect the valves from damaging. This chapter describes the optimization method used in tuning control parameters to improve the performance of proposed methodology and compares the proposed approach to the following grid-forming control methods with the current limiting capability:

- Supervisory current limiting method
- Virtual impedance current limiting method

The simple test case developed in Chapter 3 is used to compare the performance of proposed grid-forming control approach to above-mentioned methods. Figure 4.1 and Table 4.1 summarize the test system for this investigation. Since the above-mentioned current limiting approaches do not have the ability to black start and synchronize to an external source, the circuit breaker CB is initially closed, and the MMC link is operating at its full capacity. Consequently, the current limiting comparison is performed for the worst-case fault recovery of three-phase fault at the inverter bus with the MMC under full-load conditions. The fault duration is set to 120 ms to capture the worst-case dynamic performance as discussed in Chapter 3.

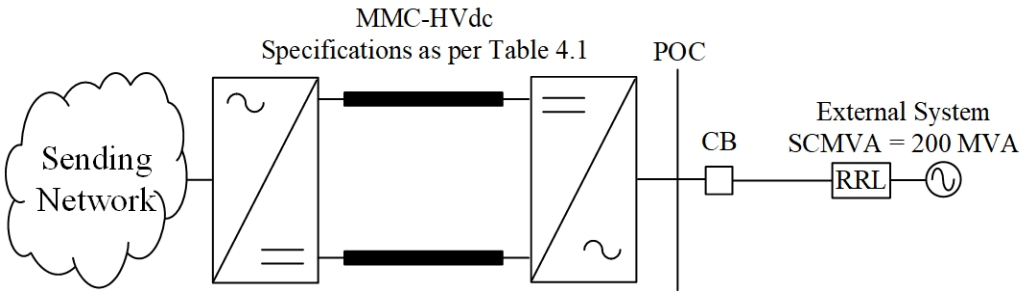

Figure 4.1: Simple test system schematic

Table 4.1: Simple test system specification

MMC-HVdc link	200 MW, ±120 kV, 250 km transmission line, symmetrical monopole Rectifier control mode: V_{dc}, V_{ac} Inverter control mode: as describe in section 4.2 and 4.3 Transformer valve side rated current: 1.5 kApk Transformer magnetizing current: 1%
External network	SCMVA = 200 MVA, 230 kV, 60 Hz

4.1 Optimization of Control Parameters

One of the challenges in any power converter is the selection of the appropriate parameters for its controllers. Since the systems are inherently non-linear, achieving this analytically by linear control analysis is difficult and has limited value. For example,

although eigen-value based analysis may be able to provide optimum gains for a given operating point, as the system is linearized around that point, it will not be able to select optimum gain when transitioning from one operating point to another. Therefore, the optimization of control parameters is more realistic for practical systems. Alternatively, the use of non-linear optimization methods as wrappers for EMT simulation programs is an increasingly used option [64]-[66]. In these approaches, the parameters of the EMT program can be modified between runs by the non-linear optimization program. The output of the EMT program is the objective function to be minimized, and is typically the integral square error between the desired and targeted outputs. This method is used to select optimum parameter for the controllers in this thesis. One advantage of this approach is that it can handle large signal models, as there is no linear-approximation in the EMT simulations. As an example, consider the selection of parameters for the current controller mentioned in section 4.2 and 4.3. An optimization of the control parameters is used to provide the most optimum control response during the disturbances for the controllers in each of the below-mentioned methods in this section. The Non-linear Simplex optimization method of Nelder and Mead [66] is chosen because it is suitable for optimization of several real variables. It requires the user to supply only function values, and not derivatives as many other optimization programs do [66]. Other optimization methods could have been used, such as Genetic algorithms, but the non-linear simplex optimization method proved to give sufficient optimized parameter values.

4.1.1 Non-Linear Simplex Method of Nelder and Mead used in EMT Simulation

This section discusses briefly how the method of Nelder and Mead is incorporated into the EMT simulation. The function to be optimized is not available as a defined function of the optimization variables, but is determined by the outcome of an EMT simulation. The section below briefly discusses the optimization algorithm used and it is followed by a section on how it interfaces to the EMT function evaluator.

4.1.1.1 Non-Linear Simplex Algorithm

In this method, an objective function is defined as an input signal to the Non-linear Simplex optimization method. At the end of each completed EMT simulation run, the optimization algorithm will determine a new set of output parameters each run and compare the difference in objective function value to the input tolerance. The value calculated by the objective function is then passed on to the Non-linear Simplex optimization algorithm for the next iteration.

The optimization algorithm uses a mathematical search technique to determine the new control parameters to reduce the value of objective function. The iteration continues until the change in objective function is less than the specified tolerance, then the optimization stops [65]. Figure 4.2 shows the flow chart of Non-linear Simplex optimization method used in EMT simulation.

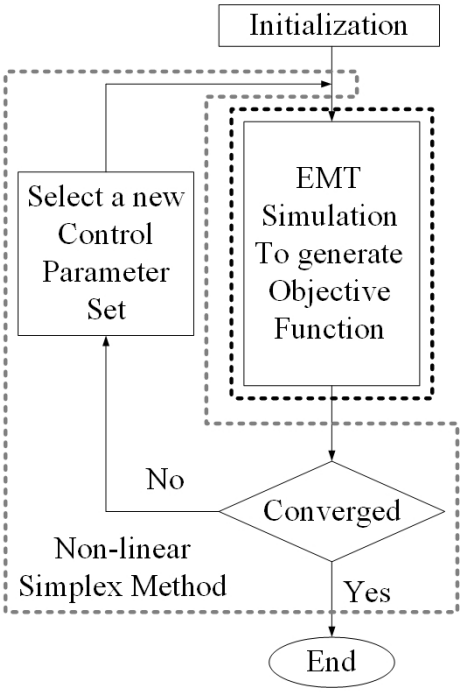

Figure 4.2: Non-linear Simplex optimization methods used in EMT simulation [65]

The Non-linear Simplex has the characteristics of a gradient following method, which moves the search in the direction of steep descent. However, unlike other gradient methods, it does not require the calculation of a derivative either analytically or

numerically. The essence of the method can be explained by considering the optimization of a 2 variable function $f(x_1,x_2)$ as in Figure 4.3. At the start, 3 points H, M and L, in the x_1 and x_2 space are selected (usually at random) and the function is evaluated at each point. The reasons for the names "H, M, L" will become clear. Consider the triangle HML that in n-space it is referred to as a "Simplex". Typically, one of these points, say $H = (x_{1h}, x_{2h})$ will have the largest value, one an intermediate value, say $f(x_{1m},x_{2m})$ at point $M = (x_{1m}, x_{2m})$ and one the lowest value $f(x_{1l}, x_{2l})$ at point $L = (x_{1l}, x_{2l})$. Obviously, if minimization is required, the point $H = (x_{1h}, x_{2h})$ must be discarded as it has the largest value. To do this, it is reflected through the midpoint of the side ML to point T and a new triangle (Simplex) TML is formed. Once again, the process is repeated, and we move away from the largest point by reflecting it across the line joining the other two vertices. If M turns out to be the new maximum function point, one would move to the point "S" in Figure 4.3.

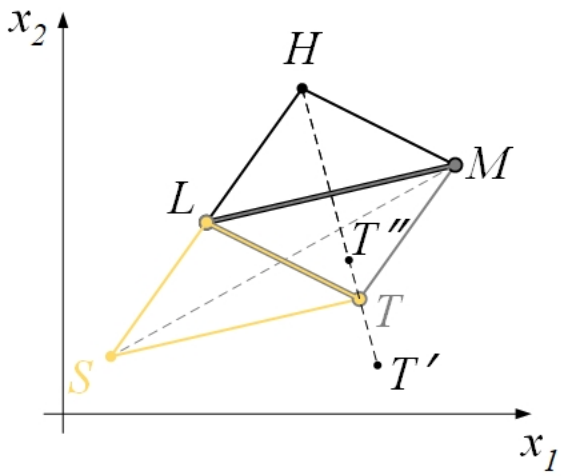

Figure 4.3: Illustration of Non-linear Simplex Optimization Method

If the direction of movement leads to a really low function value, the direction is considered a favorable one, i.e. $f(t) < f(L)$, an acceleration factor is applied by discarding T in favor of point T' where the distance $HT' = \alpha HT$. Sometimes, if the new point has a function value larger than the maximum of the previous simplex, i.e. $f(T) > f(M)$, the point T would be discarded and a contraction factor would be applied to get a new point T'' where $HT'' = \beta HT$. The optimization is said to have converged when the vertices of the Simplex no longer show a significant change in the function value.

Note that Non-linear simplex is very easy to code, but does converge rapidly to a local minimum. Hence, the optimization is carried out several times, each with a different starting Simplex at remote locations in the search space in the hope that different starting points might converge to a lower function value.

4.1.1.2 Using EMT Simulation as a Function Evaluator for the Optimization Program

Figure 4.4 shows an example of objective function developed for optimizing the control parameters of the supervisory current limiting method. The aim is to reduce the current overshoot following a fault and to have an adequate steady-state response. Hence, it penalizes the integral square error of the current from its desired reference. However, if the current magnitude is greater than 1.1 per-unit, an additional penalizing factor of 2 is used.

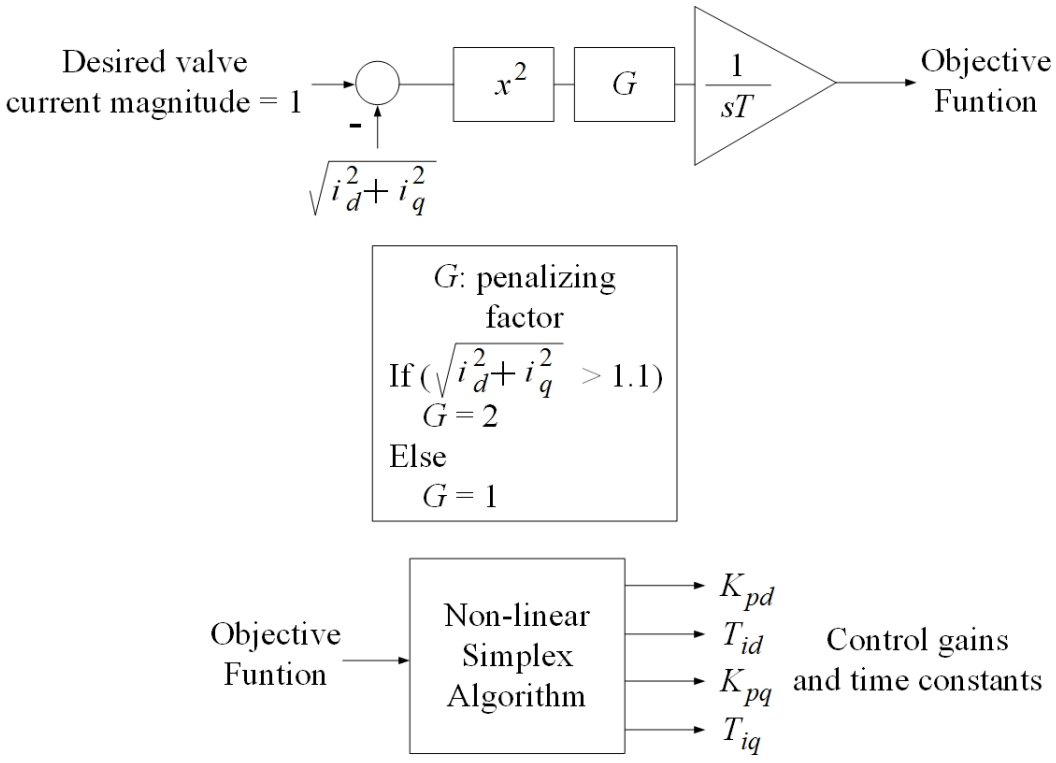

Figure 4.4: Objective function and optimization algorithm setup

Figure 4.5 shows the result of optimizing the control parameters of the supervisory current limiting method for a three-phase to ground fault on a test system shown in Figure 4.1. Prior to using Non-linear Simplex optimization method, there is an overcurrent peak of 12 kA, which exceeds the valve rated current of 1.5 kA by a factor of 8 (Figure 4.5a).

The optimization algorithm adjusts the control gains and time constants such that the transient peak of valve current is set to 3 kA (Figure 4.5b). Therefore, an optimization of the control parameters provides the most optimum control response during the disturbances for the controllers.

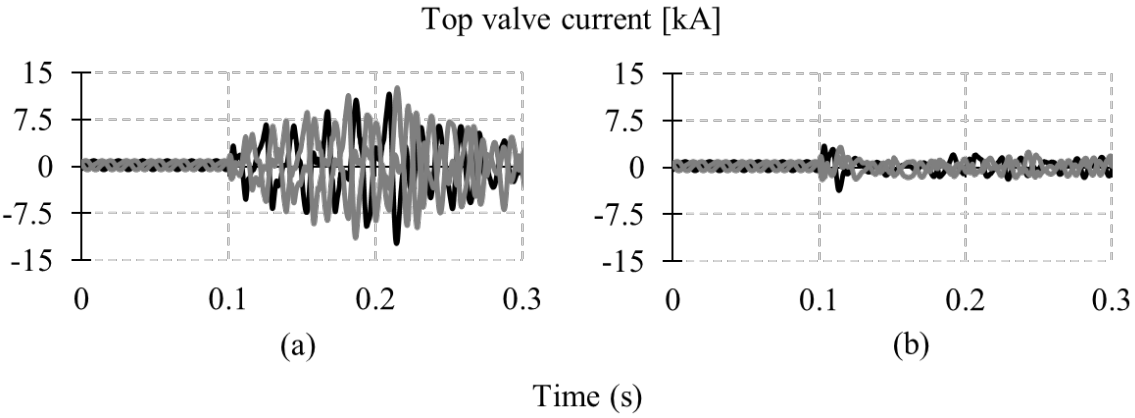

Figure 4.5: Optimization of the control parameters: (a) valve current due to 3-phase to ground fault with initial parameters (b) with optimized parameters

4.2 Supervisory Current Limiting Method

The concept of supervisory current limiter has been introduced in [70][72]. In this method, a supervisory control is designed to monitor the magnitude of valve side current continuously during the steady-state and faults as shown in Figure 4.6.

As long as the magnitude of valve current does not exceed the maximum current ceiling, I_{max}, the grid-forming control strategy shown in Figure 2.9 is used to generate the *dq*-components of VSC's internal voltage, $\boldsymbol{E_{dq}}$. If the current magnitude exceeds I_{max}, the supervisory control sends a signal to switch the control to one shown in Figure 2.7. This allows decoupled current control loop to provide fault ride-through capability and maintain the valve current within the limit during the fault.

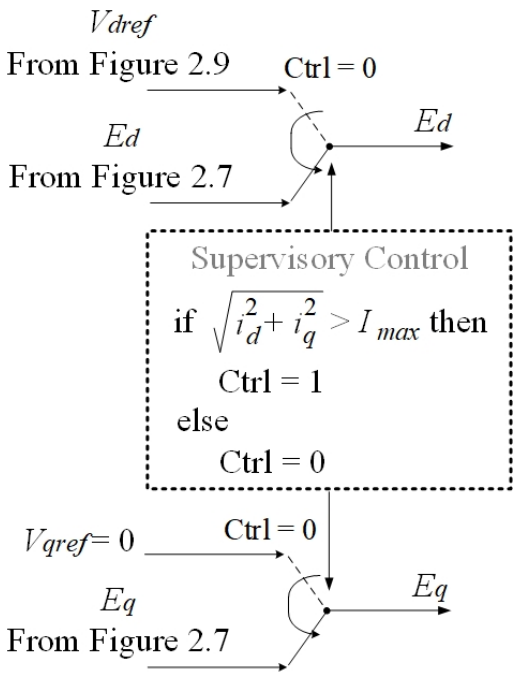

Figure 4.6: Supervisory control structure [71]

Figure 4.7 compares the result of proposed grid-forming method to the supervisory current limiting approach during a three-phase to ground fault at POC. Figure 4.7a shows the dynamic response of the proposed grid-forming control. During the fault, the valve current is successfully limited by the current controller loops to 1.65 kA.

Figure 4.7b shows the dynamic response of the supervisory current limiting approach. Although this approach maintains the valve current within the limit during the fault (Figure 4.7b-iii and Figure 4.7b-iv), there is an overcurrent peak of 3 kA at the instance of switching to decoupled current controller, which exceeds the transformer valve side rated current of 1.5 kA by a factor of 2, compared to the proposed grid-forming method.

The proposed method offers a simple approach to control the magnitude of current by automatically regulating the *dq*-reference currents through a voltage control loop. Therefore, it eliminates any potential valve overcurrent due to control mode transition or inadequate initialization of the controls at the instance of transition.

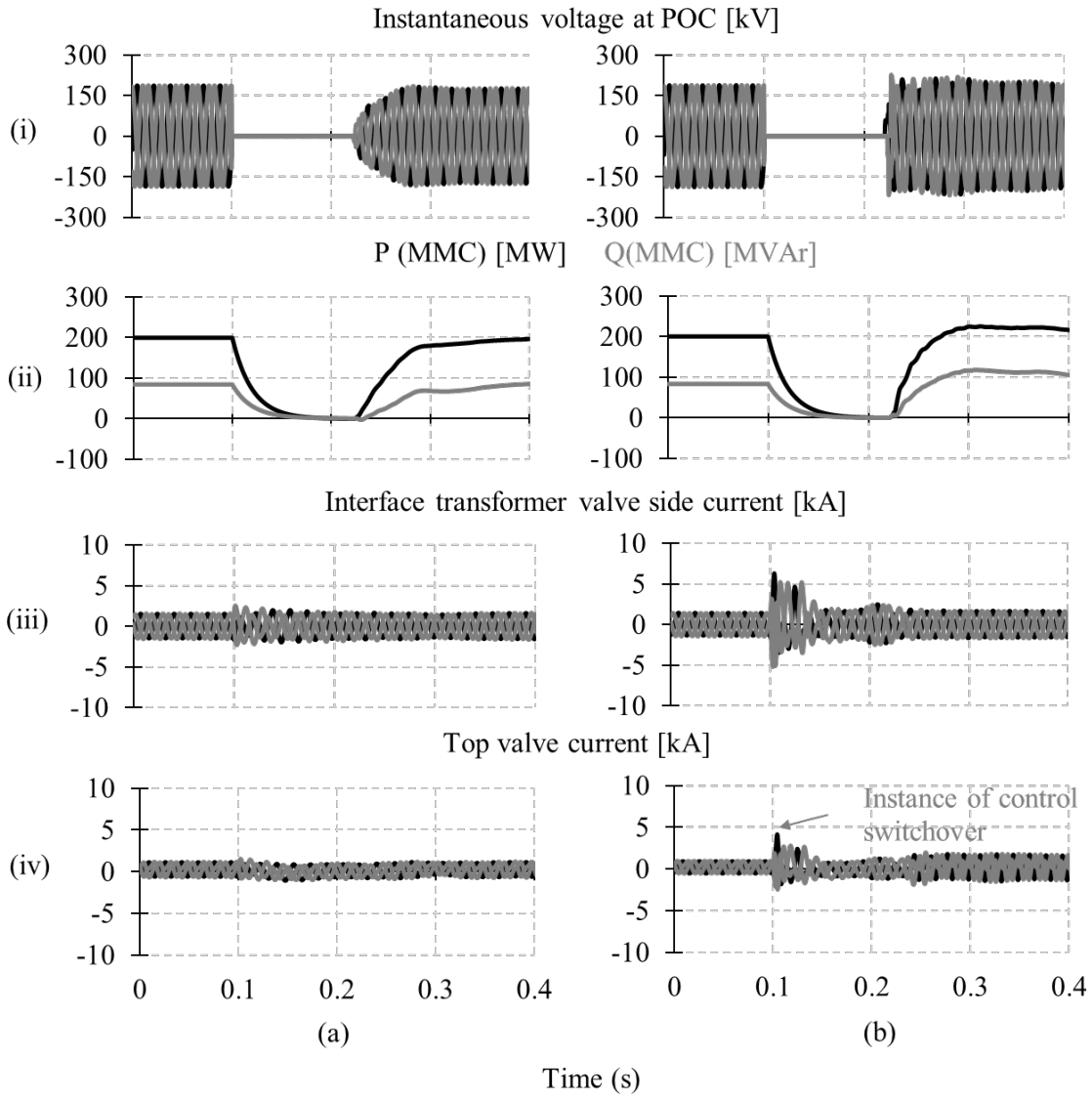

Figure 4.7: Comparing proposed grid-forming method with supervisory current limiting method due to a three-phase to ground fault a) results of proposed grid-forming method b) results of supervisory current limiting method

4.3 Virtual Impedance Current Limiting Method

The concept of virtual impedance current limiting has been discussed in section 2.1.3.2. In this method, an external voltage regulator is implemented to maintain the POC voltage magnitude to its reference value. During the steady-state operation, the converter operates in grid-forming mode shown in Figure 2.9 and the virtual impedance control mode

is only enabled when the magnitude of valve current exceeds the selected threshold current, $I_{threshold}$ (Figure 4.8).

Figure 4.8 shows the implementation of the virtual impedance calculation as per [28]. Reference [28] elaborates how the magnitude of virtual impedance and *X/R* ratio can affect stability. Furthermore, a low *X/R* ratio results in more resistive impedance that can affect coupling between active and reactive power control loops and causes stability issues [28]. Therefore, a comprehensive small-signal analysis is required to develop the virtual impedance control [28]. This becomes challenging for a larger system whose structure and operating point changes unpredictably. It can also result in excessive reactive power sharing when operating in parallel with synchronous generators.

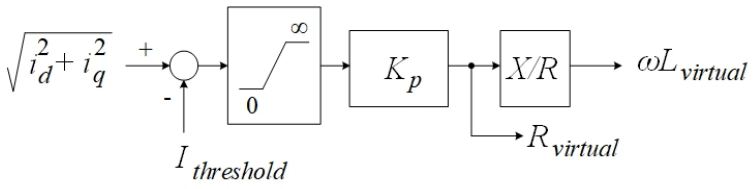

Figure 4.8: Implementation of the virtual impedance calculation [28]

Figure 4.9 compares the result of proposed grid-forming method to the virtual impedance current limiting approach during a three-phase to ground fault at POC. Figure 4.9a shows the dynamic response of the proposed grid-forming control. During the fault, the valve current is successfully limited by the current controller loops to 1.65 kA.

Figure 4.9b shows the dynamic response of the virtual impedance current limiting approach. Although this approach maintains the valve current within the limit during the fault (Figure 4.9b-iii and Figure 4.9b-iv), there is an overcurrent peak of 5 kA at the instance of enabling virtual impedance, which exceeds the transformer valve side rated current of 1.5 kA by a factor of 3, compared to the proposed grid-forming method.

Once the magnitude of valve current is less than $I_{threshold}$, the value of $R_{virtual}$ and $\omega L_{virtual}$ goes to zero, which results in an injection of 350 MVAr reactive power for a duration of 50 ms. After fault recovery, the MMC generated power shows 65 Hz oscillation that begins to damp out quickly.

Similar to the previous section, the proposed method offers a much simpler approach to control the magnitude of current by automatically regulating the *dq*-reference currents

through a voltage control loop. Therefore, it eliminates any potential valve overcurrent due to enabling/disabling virtual impedance or inadequate initialization of controls at the instance of transition.

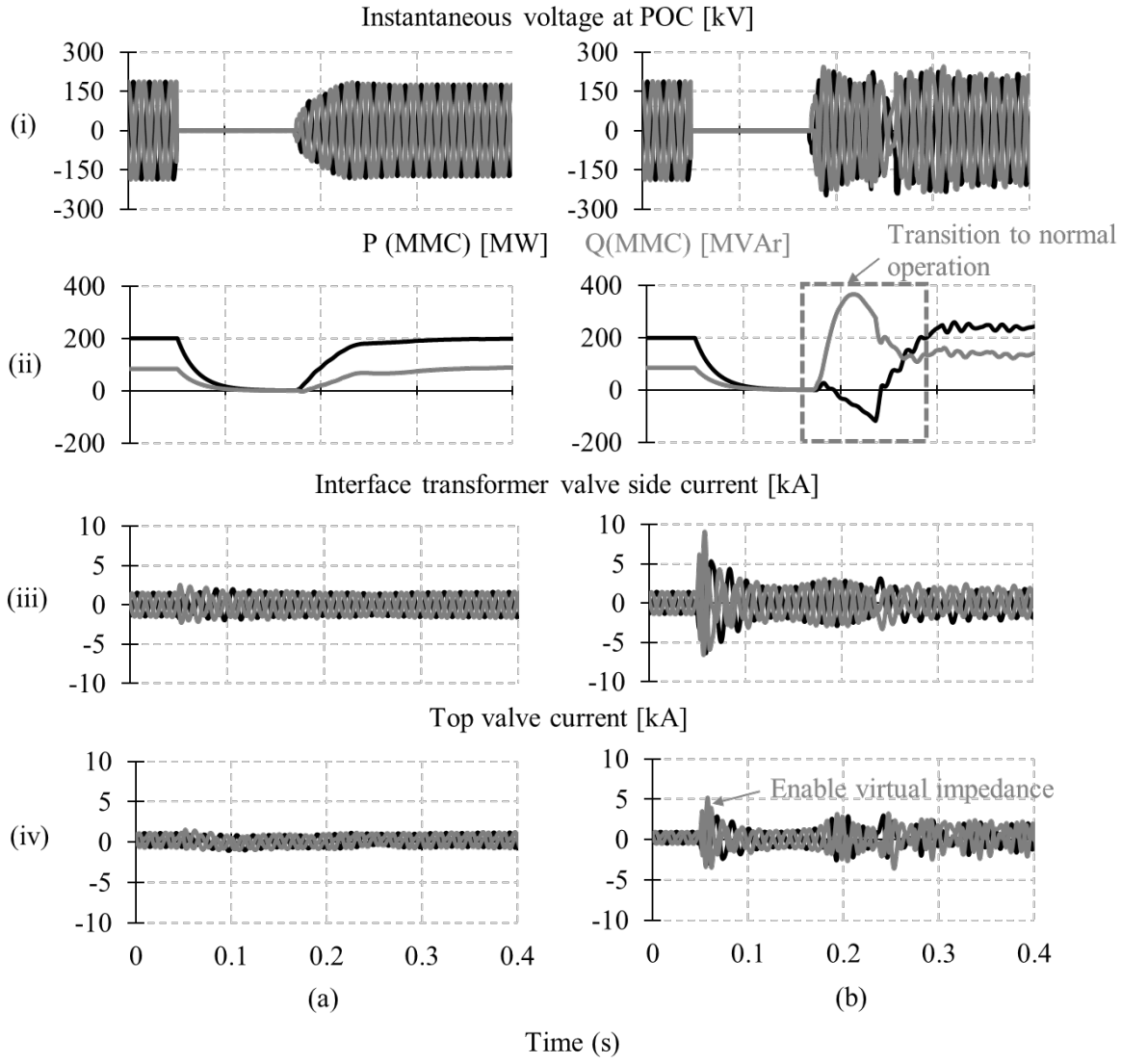

Figure 4.9: Comparing proposed grid-forming method with virtual impedance current limiting method due to a three-phase to ground fault a) results of proposed grid-forming method b) results of virtual impedance current limiting method

4.4 Chapter Concluding Remarks

Chapter 4 describes the optimization method used to tune the control parameters and improving the performance of proposed control methodology. It also compares the performance of proposed grid-forming method with the supervisory current limiting and virtual impedance current limiting approaches. The new proposed method offers a simple design approach in achieving current limiting, which results in easier control tuning and a superior performance. The next chapter investigates the described methods in the realistic systems consisting of a local area with generation, a tie to a remote network, presence of renewable energy sources and LCC-HVdc system.

Chapter 5

Different Black Start Scenarios

Earlier research has investigated connections to simplified systems. Real world systems can be more complex and have regions that are completely blacked out and remote islands of generation that have been started earlier, or were never blacked out. This chapter considers methods for restarting in such networks using the methodologies described in Chapter 3. A series of EMT simulations on realistic test systems are conducted to verify the robustness of the proposed methods.

5.1 Case Study 1: Black Start of a Local and Remote Ac Network using MMC

An EMT simulation test case (Figure 5.1) is developed to represent a black start restoration in a realistic system. The example system is modified from an actual system described in [68].

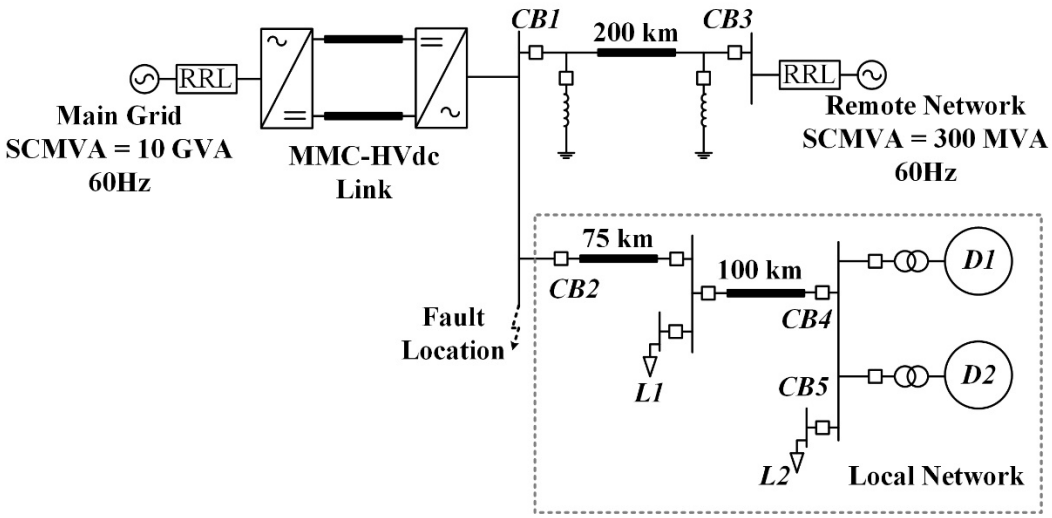

Figure 5.1: EMT simulation for Case Study 1

Table 5.1 and Table 5.2 summarizes the test system specification, which embodies the features of an actual network.

A 200 MW, ±120 kV dc link is used to transfer power from the main grid to the inverter side. The inverter bus can transfer power to a remote network with 300 MVA short circuit capability via a 200 km transmission line. It is also connected via a 75 km transmission line to a local system consisting of a 80 MW load (L_1), and further via a 100 km line to a bus with a 40 MW load (L_2) and two diesel generators. The control structure for the rectifier control and the dc line parameters are described in section 2.1.3.1 and [58].

Assume that this local network is fully blacked out, and breakers CB_1 to the remote network and CB_2 to the local load are open. The local diesel generators are disconnected

as they do not have sufficient capacity to supply the total load (L_1 and L_2). The line reactors are sized to provide sufficient reactive power support to maintain the open-end voltage in the range 0.95 to 1.05 per-unit when energized from the remote system, i.e. CB_3 is closed. The dynamic response of the grid-forming control is also investigated following single- and three-phase faults at the inverter bus.

Table 5.1: Case Study 1 – Short-Circuit MVA (SCMVA) Contribution

Remote network SCMVA contribution at POC	200 MVA
Local network SCMVA contribution at POC	115 MVA

Table 5.2: Case Study 1 – Test System Specification

MMC-HVdc link	200 MW, ±120 kV, 250 km transmission line, symmetrical monopole Rectifier control mode: V_{dc}, V_{ac} Inverter control mode: as describe in Chapter 3 Transformer valve side rated current: 1.5 kApk Transformer magnetizing current: 1%
Ac lines data	R_1 = 0.05 Ω/km, X_1 = 0.49 Ω/km, B_1 = 3.37 µS/km R_0 = 0.51 Ω/km, X_0 = 1.79 Ω/km, B_0 = 3.37 µS/km (Lengths as in Figure 5.1)
Diesel Generators	$D1$, $D2$ = 25 MVA, 0.6 kV, 60 Hz Simple governor and exciter X_d = 1.71 pu, X'_d = 0.25 pu, X''_d = 0.16 pu X_q = 0.94 pu, X''_q = 0.15 pu T'_{d0} = 2.8 sec, T''_{d0} = 0.02 sec, T''_{q0} = 0.01 sec
Line reactors	28 MVAr, 230 kV
Loads	$L1$ = 80 MW (4 x 20 MW), pf = 0.9 $L2$ = 40 MW (2 x 20 MW), pf = 0.9

5.1.1 Investigation of Black Start Restoration Options

The EMT test system is utilized to verify the functionality and performance of the proposed grid-forming control through a series of EMT simulation.

Two different black start options for the local network are considered, one in which the converter picks up the blacked out local system before connecting to the remote system, and the second, in which it first makes the connection to the remote system. Finally, the fault ride-through capability is confirmed through a single- and three-phase to ground faults. This section describes the EMT simulation results and observations during the restoration.

5.1.1.1 Option 1: Local System Energization Followed by Remote System

In this option, the transmission line at the converter side is energized first by closing Circuit Breaker CB_2, to pick up the local load (L_1). Local diesel generators (D_1 and D_2) are then connected into the local system and pick up the load (L_2). Lastly, the local system is synchronized to the remote system, CB_1 is turned on, and the VSC's power is ramped up to establish the required power flow of 120 MW to the remote system. Figure 5.2 depicts the EMT simulation results for the full re-energization using Option 1.

The switching transients at t = 1 sec and 8 sec are due to energization of the 75 km and 100 km transmission lines. The 80 MW load (L_1) is switched in increments of 20 MW from t = 3 to 6 sec to limit ac voltage dip to 0.9 per-unit. The local diesel generators are synchronized at t = 9 and 13 sec. The 40 MW load (L_2) is then switched in increments of 20 MW by the diesel generators at t = 10 and 15 sec. Finally, the local system is synchronized to the remote network at t = 20 sec by closing circuit breaker CB_1 and begins transferring 120 MW through the remote tie. One observation is that the presence of a local load required the power ramp rate to be reduced to 50 MW/s. The higher ramp rate resulted in instability. Overall, the blacked out local system is completely energized within 17 sec, whereas the full network resumes normal transmission in 23 sec.

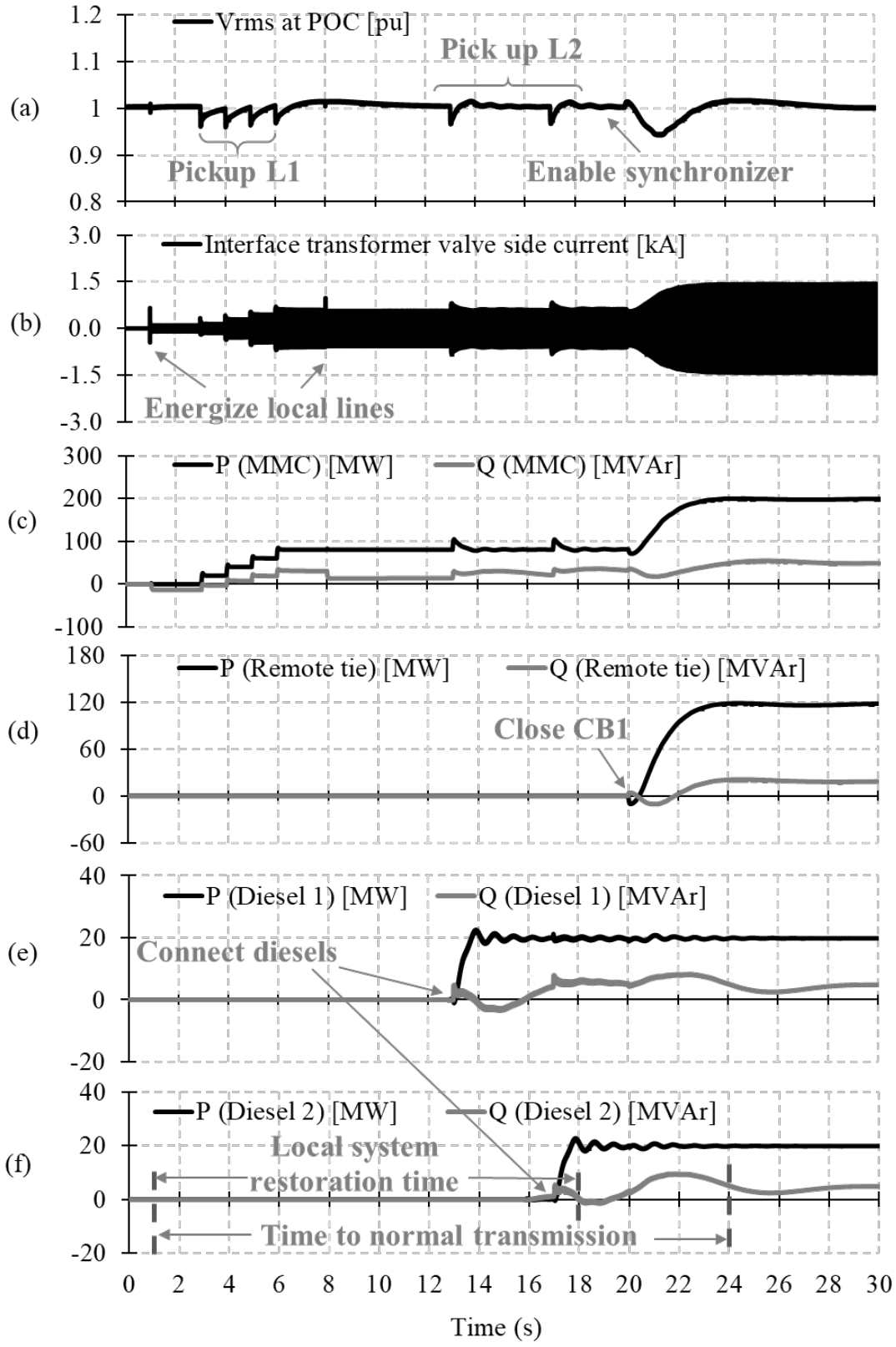

Figure 5.2: Results of local system energization followed by remote system

5.1.1.2 Option 2: Remote System Energization Followed by Local System

In this scenario, the MMC is first connected to the remote system through the 200 km tie line. The MMC's power set point is adjusted to transfer 120 MW to the remote network. Next, circuit breaker CB_2 is closed to black start the local network by first picking up the load (L_1). This is followed by sequentially synchronizing local diesel generators (D_1 and D_2). Once D_1 and D_2 are connected, circuit breaker CB_5 is closed to pick up load (L_2).

Figure 5.3 shows the EMT simulation results for Option 2. The synchronization to the remote network occurs at t = 1 sec and power is ramped to 120 MW. It was observed that to pick up the remote network, the power ramp rate could be set to 200 MW/s, which is faster than in Option 1 where it had to be reduced to 50 MW/s. The 75 km transmission line to the local load is then energized at t = 5 sec. As in Option 1, load (L_1) is picked up in increments to avoid excessive ac voltage drop from t = 7 to 10 sec. The diesel generators are synchronized at t = 13 and 18 sec; immediately followed by switching in the 40 MW load (in increments of 20 MW) at t = 14 and 19 sec. Notice that, overall, the restoration is faster with normal power transmission established in 5 sec, although the blacked out local load takes longer (19 sec) to be restored compared to Option 1.

5.1.1.3 Summary of Black Start Restoration Options

Both restoration options are successful in restoration of the local and remote network, and can be selected based on the priority of the restoration plan. For example, if the priority is to energize the totally blacked out local system, then Option 1 can be used for the restoration. It should be noted that ramping power into the remote network must be done at a slower rate when the local load is present in order to avoid voltage collapse. However, Option 2, where connection to the remote load is established first, takes longer for the local system to be energized, but reduces the total restoration time, due to the faster ramping of the power order initially. Utilities perform different system-wide black start restoration studies to identify the restoration path to be implemented.

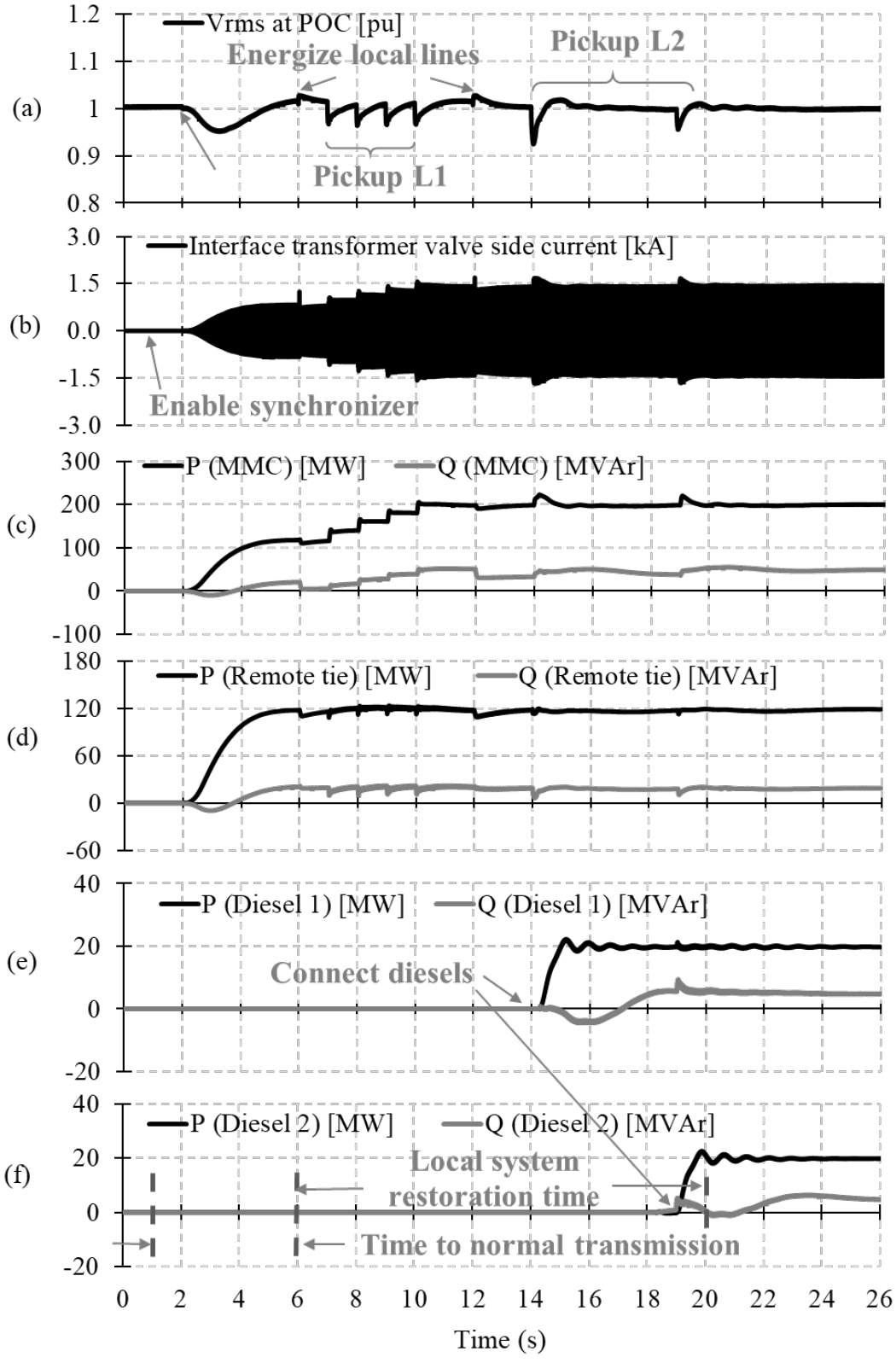

Figure 5.3: Results of remote system energization followed by local system

5.1.2 Fault Ride-Through

To investigate worst-case fault recovery, single- and three-phase faults are applied at the inverter bus with the MMC under full-load conditions. The fault duration is set to 120 ms to capture the worst-case dynamic performance as per certain grid codes [67].

Figure 5.4 and Figure 5.5 show the dynamic response of the proposed grid-forming control to a three-phase and single-phase to ground fault at t = 0.1 sec respectively. During the fault, the valve current is successfully limited by the current controller loops to 1.65 kA. After the fault clearance, the recovery is successful and 90% power is achieved in 80 ms and 60 ms for the three-phase and single-phase faults respectively.

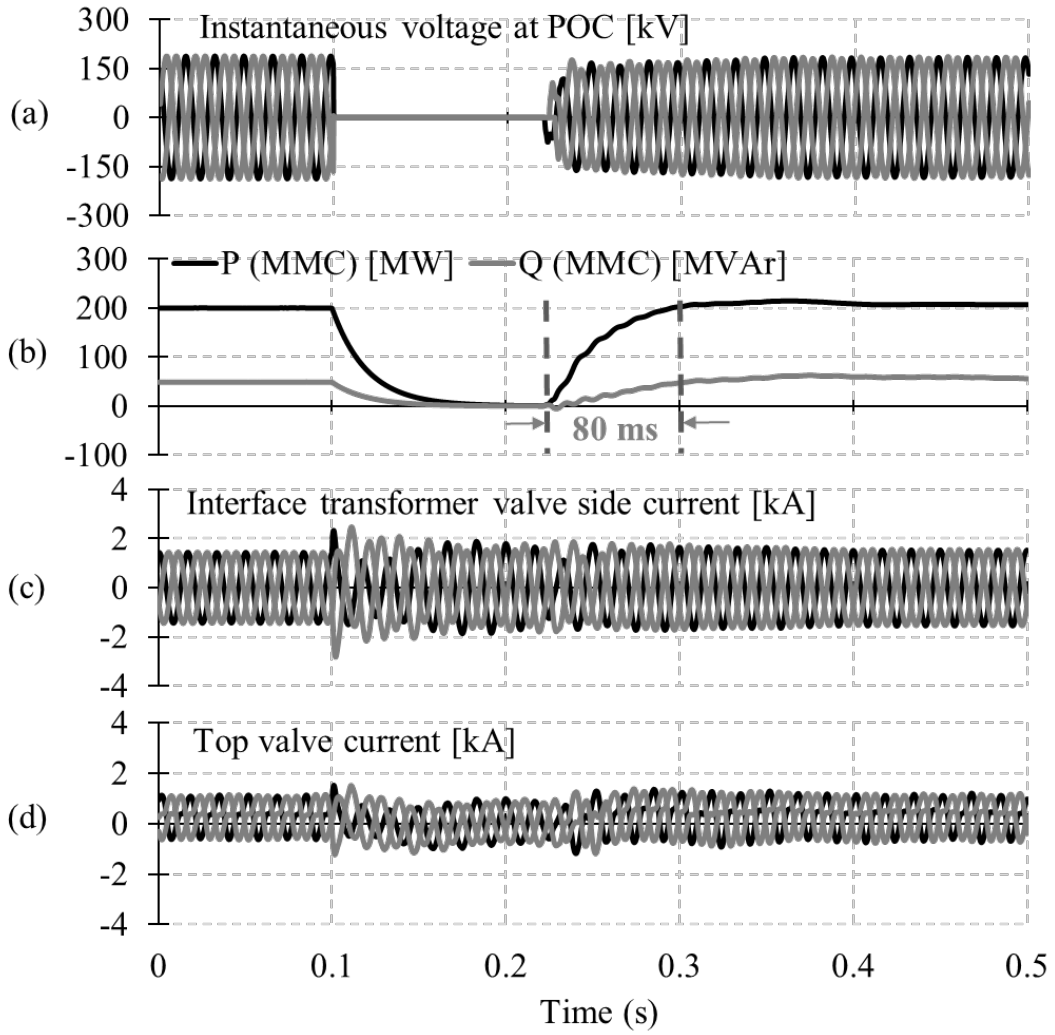

Figure 5.4: Results of a three-phase to ground fault

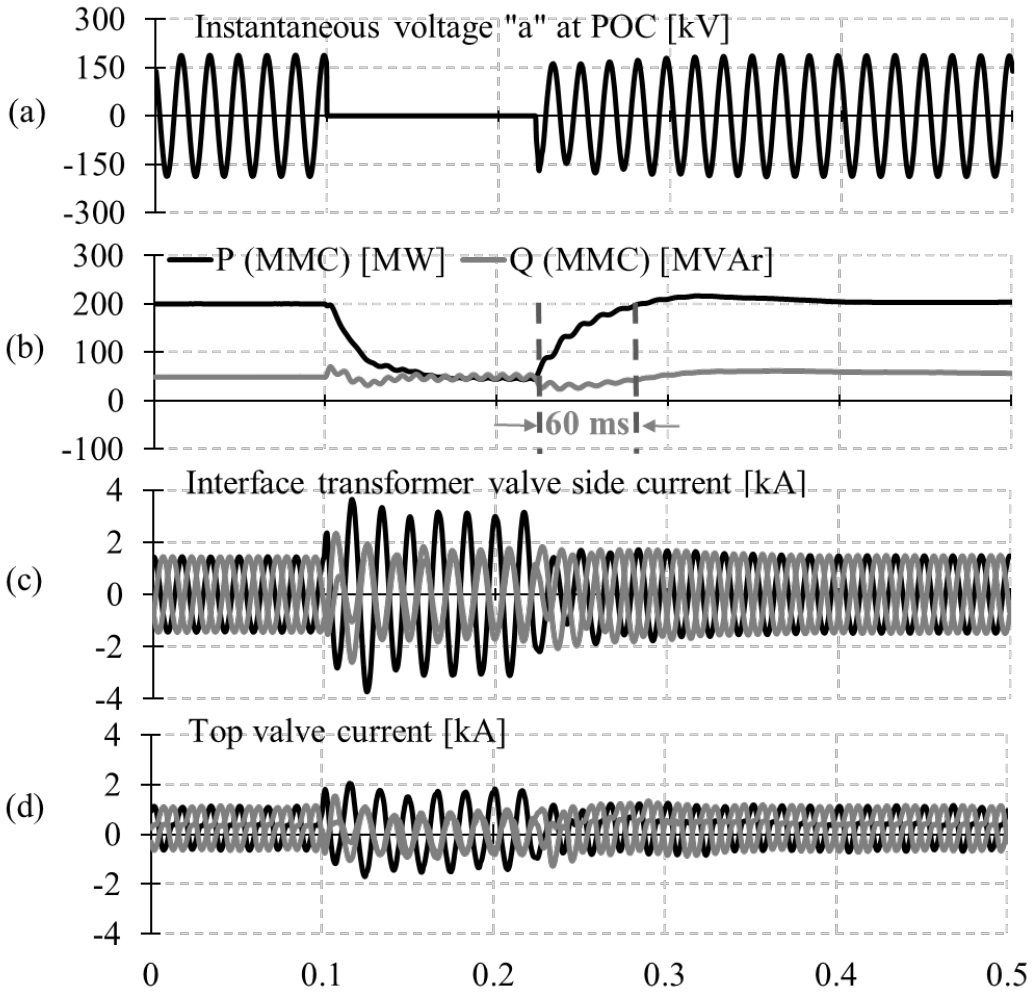

Figure 5.5: Results of a single-phase to ground fault

5.1.3 Disconnection from the Remote System

This section investigates the response of proposed grid-forming control when the transmission line connecting to the remote network is disconnected by opening CB_1 at $t = 0.1$ sec. Prior to opening of CB_1, the system operates in steady-state as discussed in section 5.1.1.1 and 5.1.1.2.

Figure 5.6 shows the dynamic response of the proposed grid-forming control to a loss of 120 MW by opening CB_1. There is an initial overvoltage of 1.08 per-unit at the instant of disconnection, which it returns to rated value within 120 ms due to the MMC voltage control loop, and the system recovers successfully and continues its operation (Figure 5.6). The local diesel generation power shows 1.25 Hz oscillation that begins to damp out.

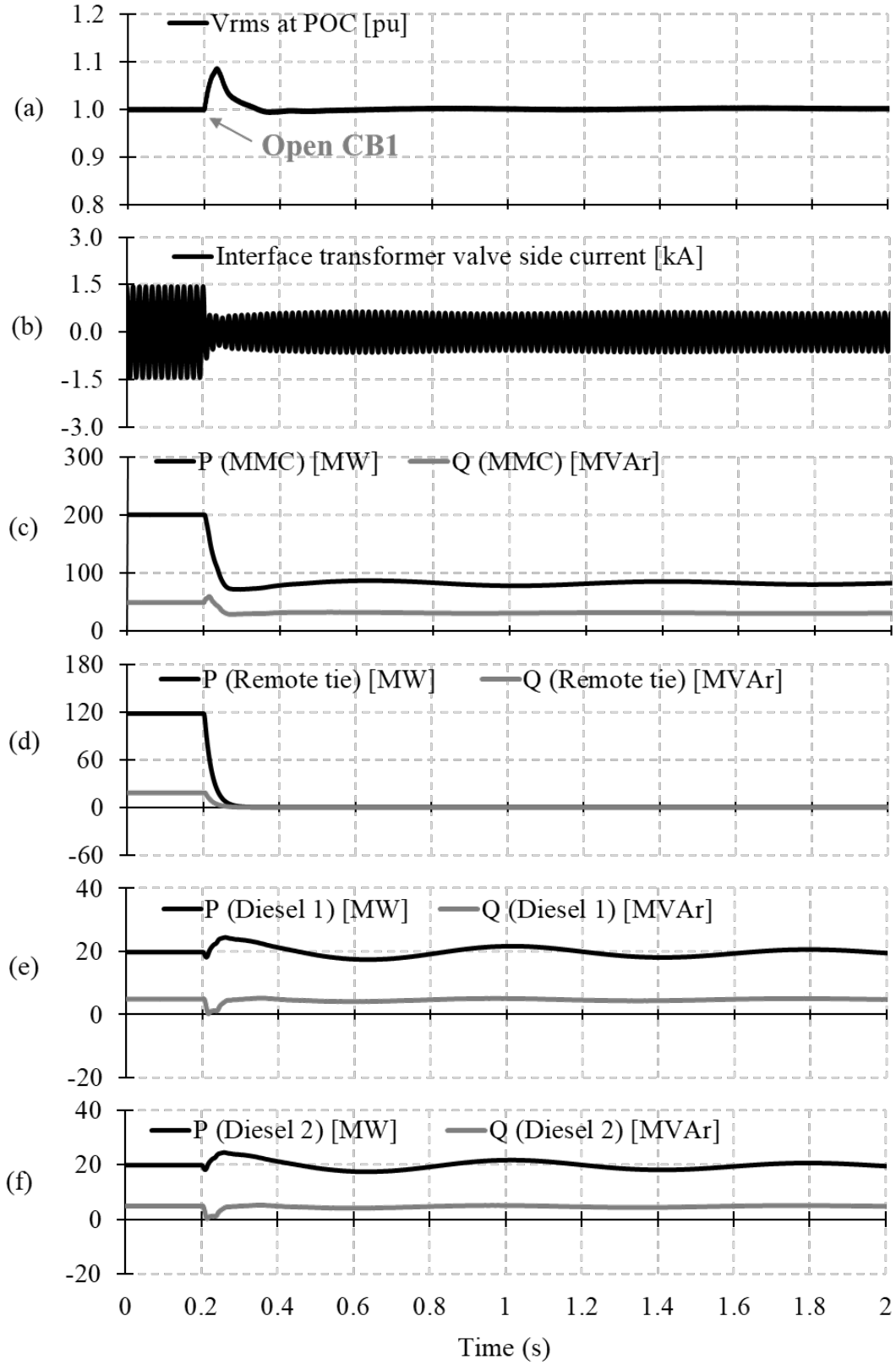

Figure 5.6: Results of 120 MW load rejection by opening CB_1

5.2 Case Study 2: Black Start of Windfarm System and a Remote Ac Network Using MMC

An EMT simulation test case of a realistic system is developed to represent use of a grid-forming converter connected into an offshore and onshore generation and several HVdc links of both, VSC and LCC type. The system is modified from an actual system described in [69] as shown in Figure 5.7. Although the converters could have bidirectional transmission capability, the thesis discusses the more common scenario where power from the onshore and offshore generation is being evacuated, and hence the labels “Rectifier” and “Inverter” on the various converters are as indicated.

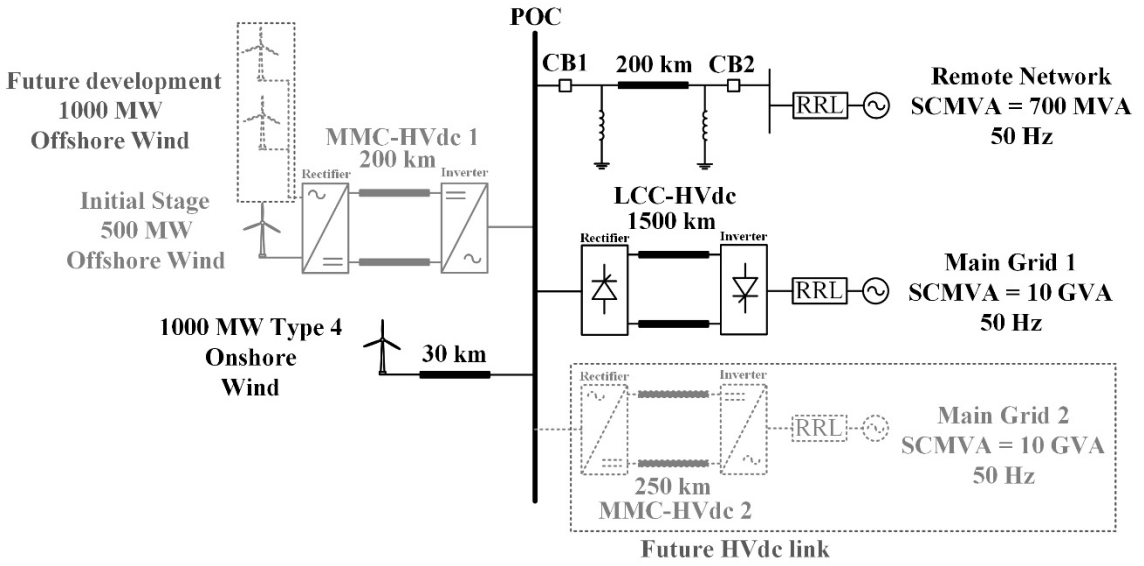

Figure 5.7: EMT simulation for Case Study 2

In the initial stage of offshore windfarm implementation, the total offshore generated power is at 500 MW. A 1500 MW, ±320 kV MMC-HVdc 1, 200 km long dc cable is designed to transfer offshore wind power to POC considering the future increase of offshore wind power.

In this stage, the power at the POC comes from a 1000 MW onshore windfarm connected via a 30 km underground ac cable, and from the 500 MW offshore generation

through MMC 1. A 1500 MW power is transferred to Main Grid 1, via a 1000 MW, ±500 kV, 1500 km overhead LCC-HVdc connection; and a 500 MW to a remote network with 700 MVA short circuit capability via a 200 km ac connection.

The MMC1's rectifier and the dc line parameters are described in section 2.1.3.1 and [58]. LCC's control structures are described in [40]. Table 5.3 gives the test system specification.

Table 5.3: Case Study 2 – Test System Specification

Remote network SCMVA contribution at POC	500 MVA
MMC-HVdc 1	1500 MW, ±320 kV, 200 km dc cable, symmetrical monopole Rectifier control mode: V_{dc}, Q Inverter control mode: grid-forming as describe in Chapter 3 Offshore windfarm control mode: grid-forming as describe in Chapter 3 Transformer valve side rated current: 4.9 kApk Transformer magnetizing current: 1%
LCC-HVdc	1000 MW, ±500 kV, 1500 km transmission line, symmetrical monopole Rectifier and inverter control mode: as describe in [40]
Ac lines data	R_1 = 0.04 Ω/km, X_1 = 0.37 Ω/km, B_1 = 4.5 µS/km R_0 = 0.41 Ω/km, X_0 = 1.36 Ω/km, B_0 = 4.5 µS/km (Lengths as in Figure 5.7)
Ac cables data	R_1 = 0.05 Ω/km, X_1 = 0.12 Ω/km, B_1 = 59 µS/km R_0 = 0.5 Ω/km, X_0 = 1.48 Ω/km, B_0 = 59 µS/km (Lengths as in Figure 5.7)
Onshore & Offshore windfarms	5 MW Type 4 as describe in [36]
Line reactors	66 MVAr, 380 kV

5.2.1 Operation of MMC-HVdc 1 without Grid-forming Capability in the Initial Implementation of Offshore Windfarm

Originally, MMC 1's inverter operates in a non-grid-forming mode, the loss of the 200 km transmission line to the remote network (say, following a fault), means that there is no voltage reference for the PLLs of the other (non-grid-forming MMC 1, onshore type 4 and LCC) to synchronize. Therefore, this results in the tripping of all converters and subsequent loss of the entire 1500 MW of generation as shown in this section.

A permanent three-phase to ground fault occurs at t = 0.1 sec for a duration of 120 ms. The fault is cleared by opening CB_1 and CB_2 permanently at t = 0.22 sec (Figure 5.8a). As there is no grid-forming capability, disconnection of the 200 km transmission line to the remote network (Figure 5.8b) results in the POC frequency exceeding the protection level of windfarms. As per certain grid codes [67], if the POC frequency exceeds 52 Hz, the windfarms trip and results in the loss of the entire 1500 MW of generation (Figure 5.8c through Figure 5.8e).

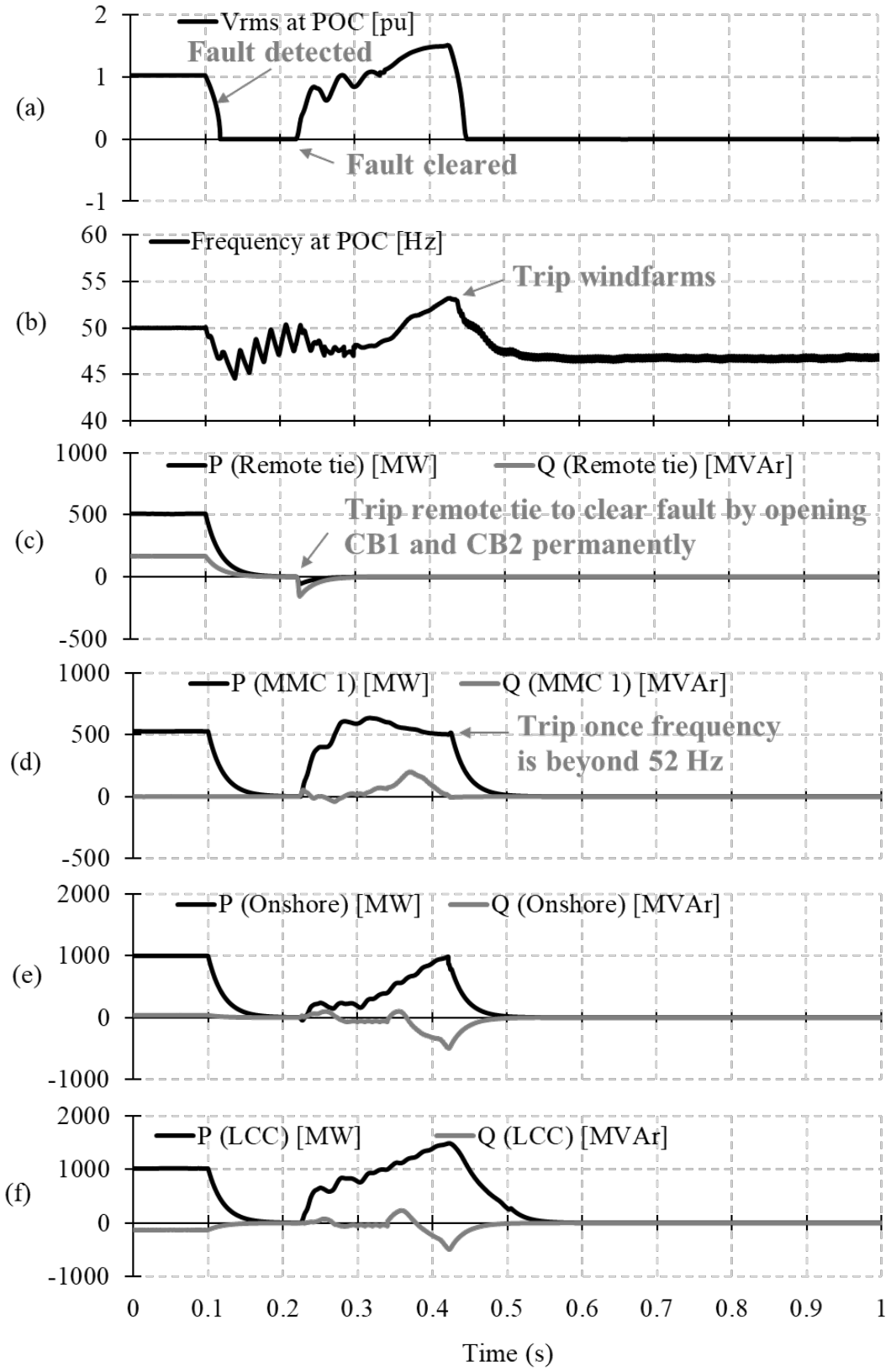

Figure 5.8: Results of the loss of remote tie due to a three-phase to ground fault followed by tripping the remote tie

5.2.2 Operation of MMC-HVdc 1 with Grid-forming Capability in the Initial Implementation of Offshore Windfarm

Now consider that MMC 1 is designed to:

- Provide grid-forming support so that the PLL tracking is avoided if a 200 km transmission line is disconnected.
- Provide black start support for the existing system (discussed in section 5.2.3).

This section demonstrates the importance of grid-forming support to avoid the problems discussed in section 5.2.1.

Assume that the system is operating at full capacity and MMC 1's inverter is in grid-forming mode. A permanent three-phase to ground fault occurs at t = 0.1 sec for a duration of 120 ms. The fault is cleared by opening CB_1 and CB_2 permanently at t = 0.22 sec (Figure 5.9a). After disconnecting (Figure 5.9c), MMC 1's inverter continues operating in the grid-forming mode (Figure 5.9d) by generating the three-phase voltage and establishing the system frequency (Figure 5.9b) so that the PLL of other converters can be synchronized.

The onshore power is reduced after fault clearing to match the LCC link capacity at t = 0.22 sec (Figure 5.9e and Figure 5.9f).

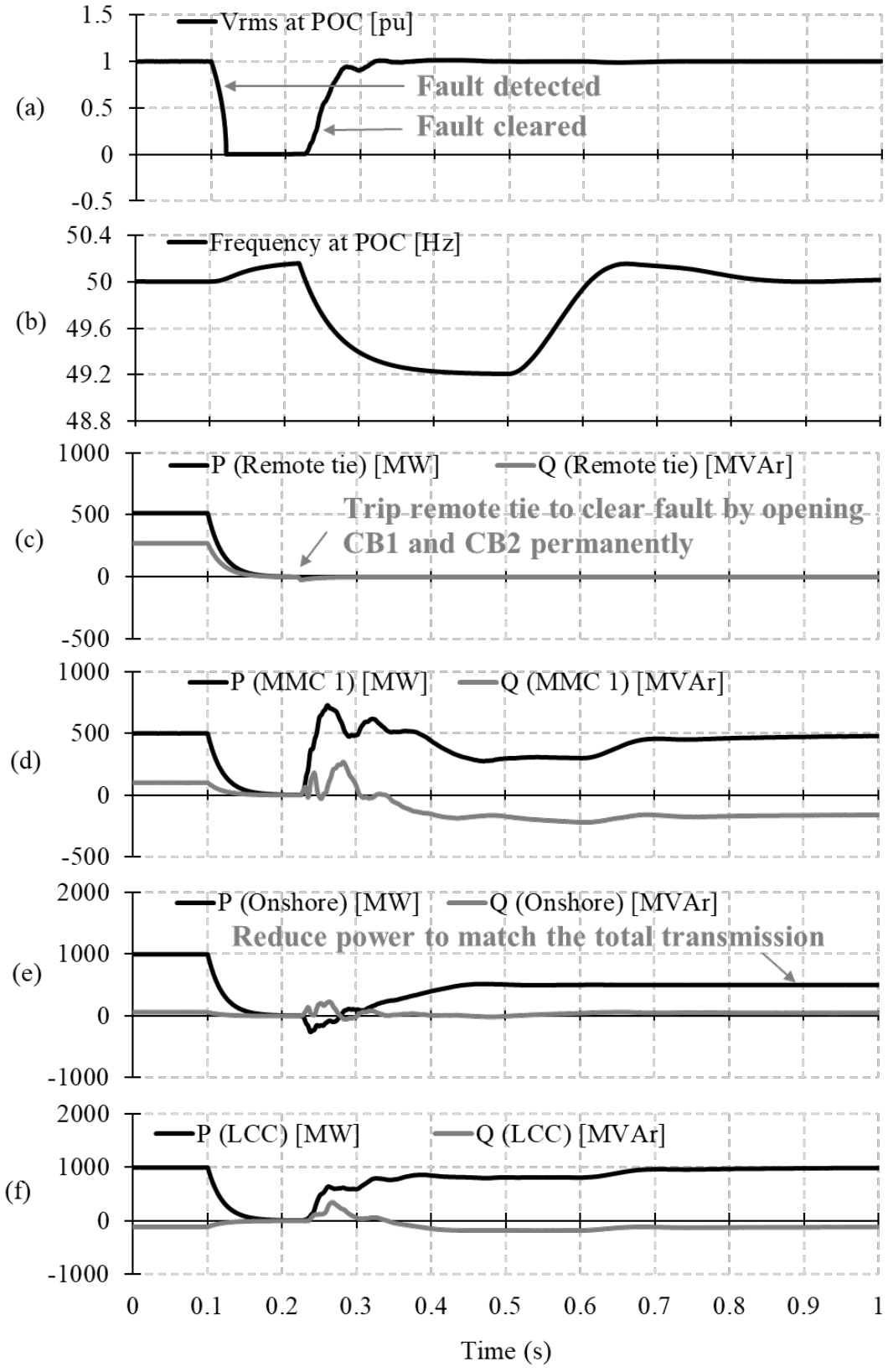

Figure 5.9: Results of the loss of remote tie due to a three-phase to ground fault followed by tripping the remote tie

5.2.3 Investigation of Black Start Restoration Using MMC-HVdc 1

Assume that the test system in Figure 5.7 is fully blacked out, and breaker CB_1 to the remote network is open. The line reactors are sized to provide sufficient reactive power support to maintain the open-end voltage in the range 0.95 to 1.05 per-unit when energized from the remote system, i.e. CB_2 is closed.

In this scenario, assume the offshore windfarm operates in grid-forming mode. This allows the energization of MMC 1 link. The dc voltage on MMC-HVdc 1 link is obtained from the rectifier side, connected to the offshore windfarm, while the inverter operates in the grid-forming mode and provides the ac voltage at the POC to which the LCC rectifier and onshore windfarm can synchronize. Next, the POC bus is synchronized to the remote network through the 200 km tie line by turning on CB_1. Lastly, the offshore and onshore wind power is ramped to establish the required power flow of 500 MW to the remote system, and 1000 MW though the LCC link. Figure 5.10 shows the EMT simulation results for this scenario.

The synchronization to the remote network occurs at $t = 2.2$ sec by closing circuit breaker CB_1, and the offshore and onshore wind power is ramped to 500 MW and 1000 MW at $t = 2.5$ sec respectively. Overall, the blacked out system is completely energized within 4 sec, whereas the full network resumes normal transmission in 5 sec.

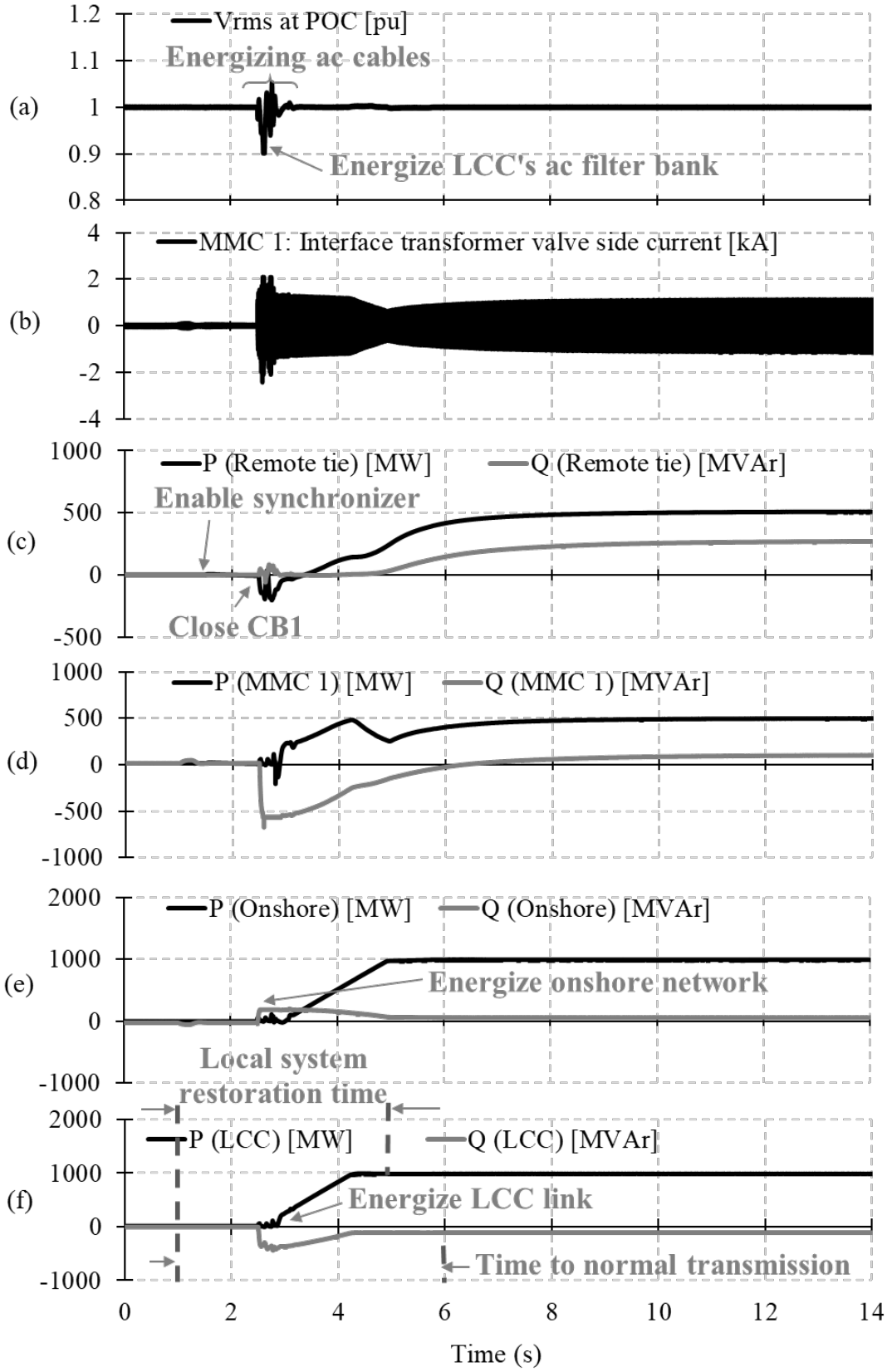

Figure 5.10: Results of black start restoration using MMC-HVdc 1

5.2.4 Investigation of Black Start Restoration Using MMC-HVdc 2

In the final stage of offshore windfarm implementation, the total offshore generated power is increased to 1500 MW. Hence, the MMC-HVdc 2 is a proposed new link so that it can connect and transfer the extra 1000 MW power to Main Grid 2 via a 1500 MW, ±320 kV MMC link, 250 km overhead transmission line as shown in Figure 5.11. It can also pick-up the power through the remote tie if the line is out-of-service. Table 5.3 gives the test system specification.

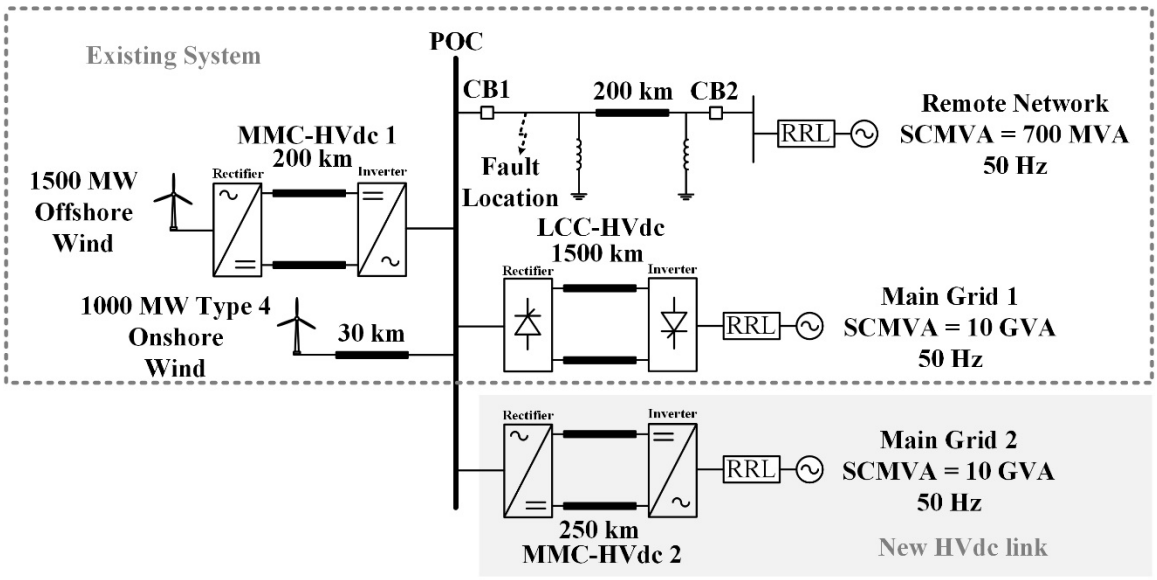

Figure 5.11: EMT simulation for Case Study 2: Addition of new MMC-HVdc 2 link

In this stage, the power at the POC comes from a 1000 MW onshore windfarm connected via a 30 km underground ac cable, and from a 1500 MW MMC 1. The POC bus can transfer power to a remote network with 700 MVA short circuit capability via a 200 km transmission line. It is also connected to a larger grid labelled Main Grid 1 via a 1000 MW, ±500 kV LCC, 1500 km overhead transmission line.

The MMC 2 is also designed to operate in grid-forming mode to increase the system reliability because in the absence of MMC 1, the loss of the 200 km transmission line to

the remote network means that there is no voltage reference for the PLLs of the other (non-grid-forming converters of onshore windfarm and LCC-HVdc) to synchronize. Therefore, this can result in the tripping of all converters and subsequent loss of the entire generated power. The new MMC 2 is introduced to:

- Provide additional grid-forming support so that the PLL tracking is avoided if a 200 km transmission line is disconnected, and be able to pick up the extra power (discussed in section 5.2.5).
- Provide additional black start support for the existing system.
- Transfer additional wind generation to Main Grid 2.

Assume that the network shown in Figure 5.11 is fully blacked out, and breaker CB_1 to the remote network is open. The line reactors are sized to provide sufficient reactive power support to maintain the open-end voltage in the range 0.95 to 1.05 per-unit when energized from the remote system, i.e. CB_2 is closed.

Two different black start options are considered, one in which MMC 2 is used to energize the LCC link, offshore and onshore windfarms before connecting to the remote network, and the second, in which it first makes the connection to the remote network. Although the converters could have bidirectional transmission capability, the thesis discusses the more common scenario where power from the onshore and offshore generation is being evacuated, and hence the labels “Rectifier” and “Inverter” on the various converters are as indicated.

5.2.4.1 Option 1: LCC Link, Offshore and Onshore Windfarms Energization Followed by Remote System

In this option, Main Grid 2 energizes the MMC 2 link while MMC 2 rectifier operates in the grid-forming mode and provides the ac voltage at the POC to which the LCC rectifier and MMC 1 inverter can synchronize. Once all converters are synchronized, evacuation of the generated power from the offshore and onshore windfarms can be initiated and power is transferred from the POC to Main Grid 1 and 2 through LCC and MMC 2 links. Lastly, the POC bus is synchronized to the remote system, CB_1 is turned on, and the offshore windfarm power is ramped up to establish the required power flow of 500 MW to the remote system. Figure 5.12 depicts the EMT simulation results for the full re-energization using Option 1.

The transients at $t = 1$ sec to 2 sec are due to energization of the offshore and onshore passive network. The offshore and onshore windfarms are de-blocked at $t = 2$ sec. Both LCC and MMC 2 links together begin transferring 1000 MW each to Main Grid 1 and Main Grid 2 at $t = 2$ sec. Finally, the energized system is synchronized to the remote network at $t = 7.5$ sec by closing circuit breaker CB_1 and begins transferring 500 MW through the remote tie by increasing the offshore windfarm power to 1500 MW. Overall, the blacked out system is completely energized within 4 sec, whereas the full network resumes normal transmission in 11 sec.

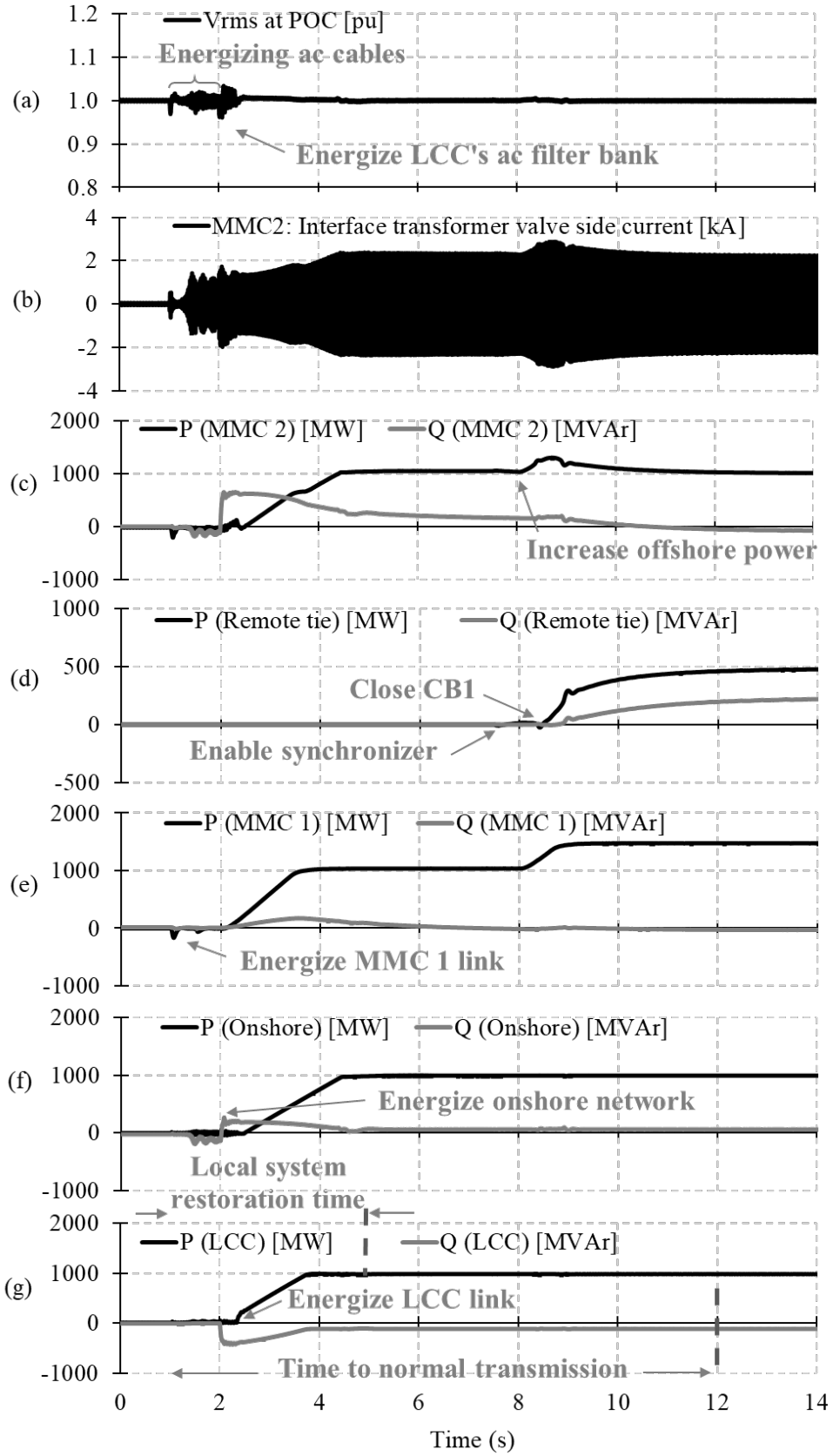

Figure 5.12: Results of system energization followed by remote system

5.2.4.2 Option 2: Remote System Energization Followed by LCC link, Offshore and Onshore Windfarms

The dc voltage on MMC-HVdc 2 link is obtained from the inverter side system and MMC 2 rectifier operates in the grid-forming mode and energizes the POC. Next, the POC bus is synchronized to the remote network through the 200 km tie line by turning on CB_1. Lastly, the offshore and onshore wind power is ramped to establish the required power flow of 500 MW to the remote system, 1000 MW though the LCC link, and a 1000 MW through MMC 2 link. Figure 5.13 shows the EMT simulation results for Option 2.

The synchronization to the remote network occurs at $t = 2$ sec by closing circuit breaker CB_1, and the offshore and onshore wind power is ramped to 1500 MW and 1000 MW at $t = 2$ sec respectively. Notice that, overall, the restoration is faster with normal power transmission established in 5 sec.

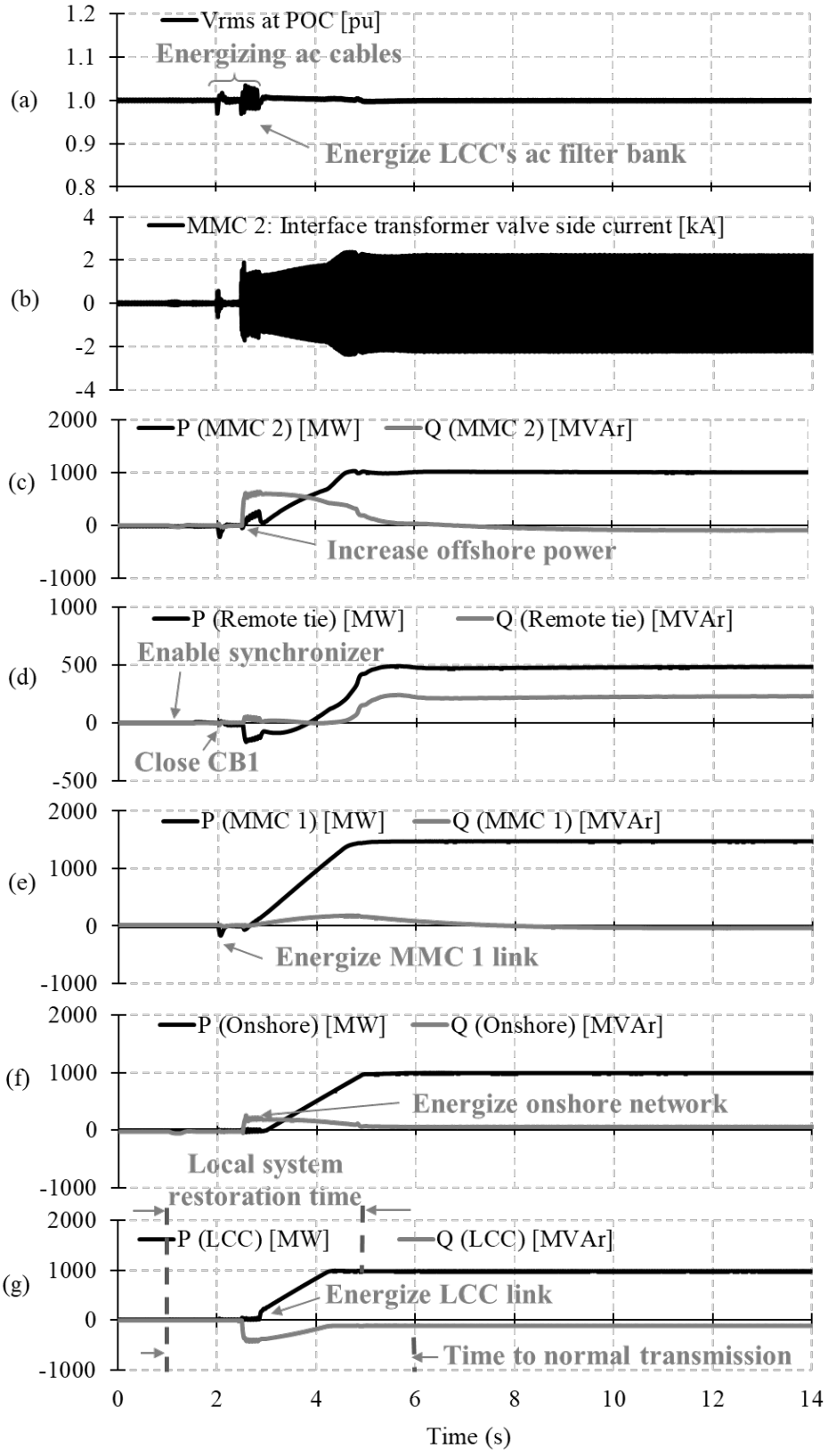

Figure 5.13: Results of remote system energization followed by LCC link, offshore and onshore system

5.2.4.3 Summary of Black Start Restoration Options

All restoration options are successful in restoration of the LCC link, offshore and onshore systems and remote network, and can be selected based on the priority of the restoration plan. It should be noted that the case study 2 allows for a significantly faster restoration process due to the presence of inverter-based generation.

5.2.5 Disconnection from Remote System due to a Fault when MMC-HVdc 2 operates in Grid-forming mode

This section demonstrates the importance of grid-forming support so that PLL tracking is avoided. It considers the case when MMC-HVdc 1 is operating in a non-grid-forming mode. The 200 km transmission line to the remote network becomes the only source to provide the voltage reference for the PLLs of the other converters to synchronize.

As discussed earlier, MMC 2 is designed to provide additional grid-forming support if a 200 km transmission line is disconnected, and be able to pick up the extra power.

Assume that the system is operating at full capacity and MMC 2 is in grid-forming mode. A permanent three-phase to ground fault occurs at t = 0.1 sec for a duration of 120 ms. The fault is cleared by opening CB_1 and CB_2 permanently at t = 0.22 sec (Figure 5.14a). After disconnecting (Figure 5.14d), MMC 2 continues operating in the grid-forming mode by generating the three-phase voltage and establishing the system frequency (Figure 5.14b) so that the PLL of other converters can be synchronized.

The offshore, onshore and LCC link continue their normal operation after fault clearing at t = 0.22 sec (Figure 5.14e through Figure 5.14g), while the MMC 2 picks up the remote tie power as shown in Figure 5.14b and Figure 5.14c.

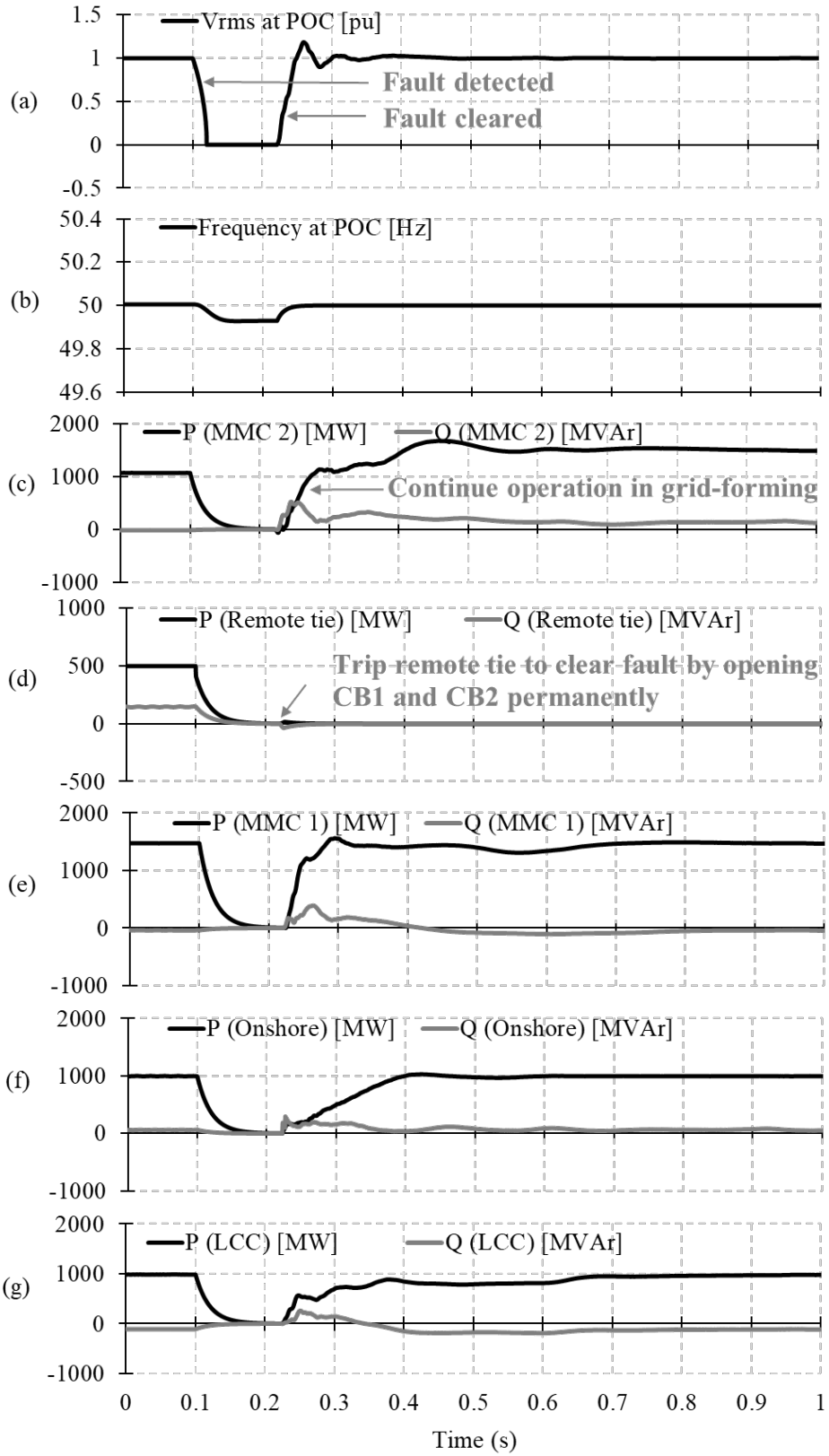

Figure 5.14: Results of grid-forming control due to a three-phase to ground fault followed by tripping the remote tie

5.2.6 Fault Ride-Through

This section demonstrates the fault ride-through capability of the proposed grid-forming control through single- and three- phase to ground faults.

To investigate worst-case fault recovery, single- and three-phase faults are applied at the POC bus with the system under full-load conditions. The fault duration is set to 120 ms to capture the worst-case dynamic performance as per certain grid codes [67].

Figure 5.15 and Figure 5.16 show the dynamic response of the proposed grid-forming control to a three-phase and single-phase to ground fault at $t = 0.1$ sec respectively. During the fault, the valve current is successfully limited by the current controller loops to 5.4 kA. After the fault clearance, the recovery is successful and 90% power is achieved in 80 ms for the three-phase and single-phase faults.

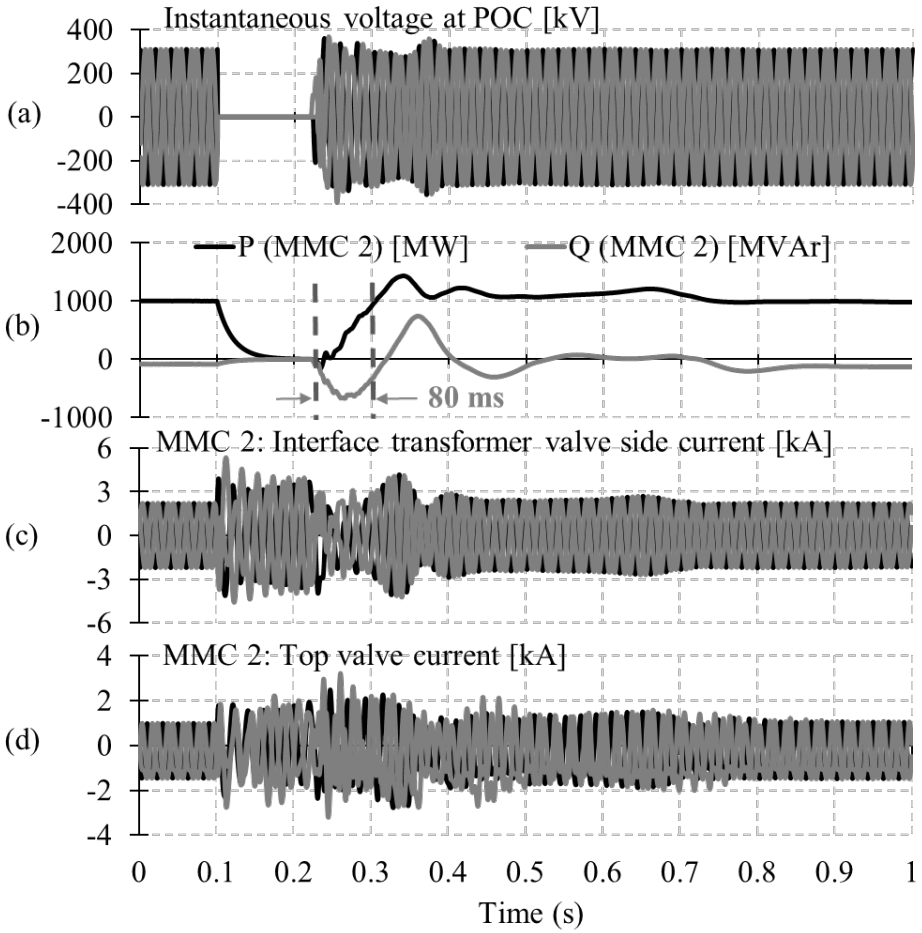

Figure 5.15: Results of a three-phase to ground fault

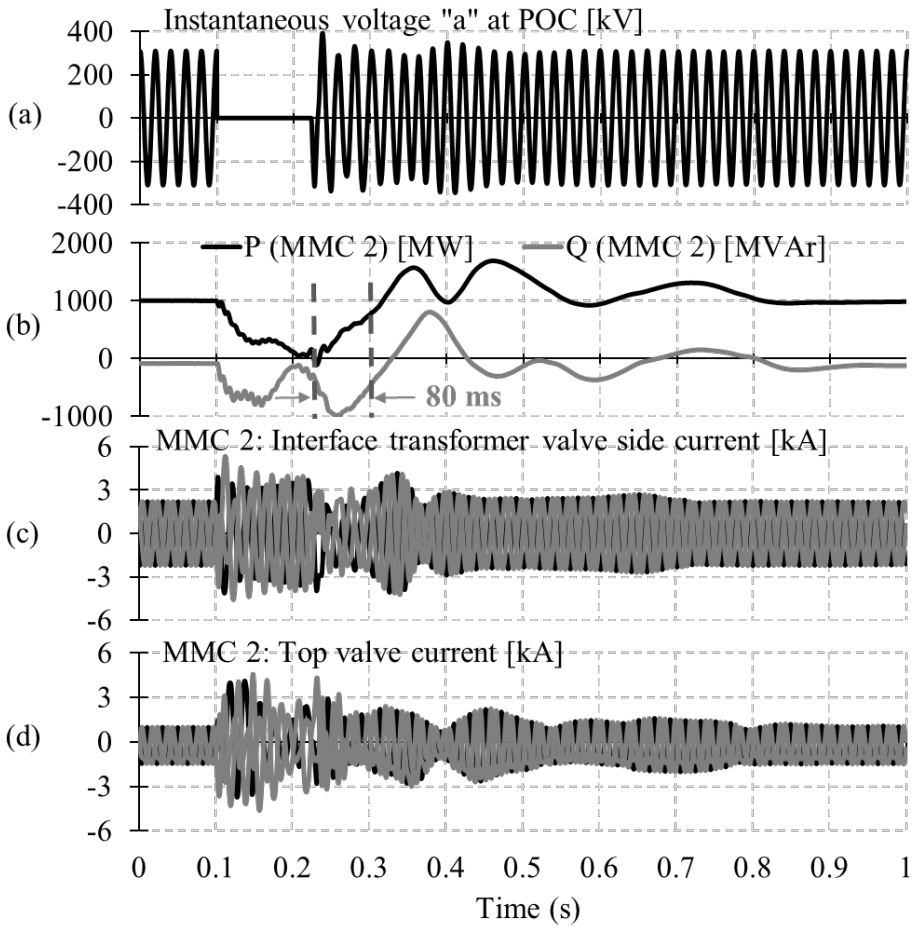

Figure 5.16: Results of a single-phase to ground fault

5.2.7 Synchronizing Multiple MMC-HVdc Converters in the Grid

If the converters of MMC-HVdc1 and MMC-HVdc2 connected to the POC are both grid forming, the question arises to how they can be synchronized with each other. This section demonstrates the capability of proposed grid-forming method for synchronization these two MMC converters. This feature is important when dealing with a restoration of multi-infeed HVdc system.

Consider both MMC 1's inverter and MMC 2's rectifier operating in grid-forming mode as highlighted in Figure 5.17. Assume that the test system in Figure 5.17 is fully blacked out as described earlier. Three different scenarios are considered:

- Synchronization of MMC 1's inverter and remote system followed by MMC 2's rectifier

- Synchronization of MMC 2's rectifier and remote system followed by MMC 1's inverter
- Synchronization of MMC 1's inverter and MMC 2's rectifier followed by remote system

These scenarios are discussed in the following sections.

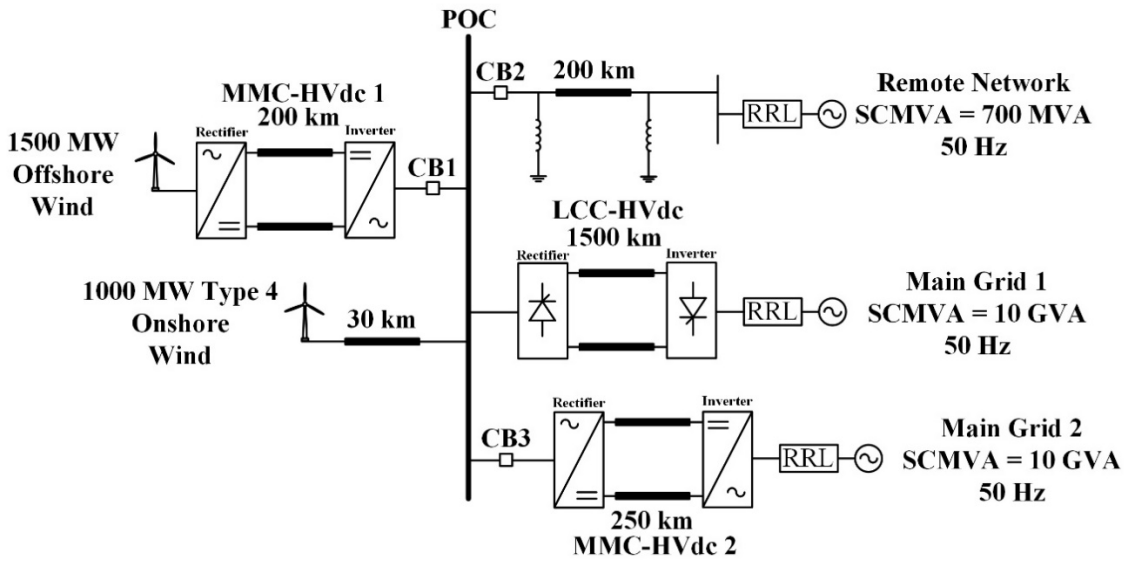

Figure 5.17: EMT simulation for operating MMC-HVdc 1 and MMC-HVdc 2 in grid-forming mode

5.2.7.1 Scenario 1: Synchronization of MMC 1 and Remote System Followed by MMC 2

Initially, MMC 1's inverter is used to operate in the grid-forming mode and provide ac voltage at the POC to which the LCC rectifier and onshore windfarm can synchronize, i.e. CB_1 is closed. Similar to section 5.2.3, the POC bus is synchronized to the remote network through the 200 km tie line by turning on CB_2, and the offshore and onshore wind power is ramped to establish the required power flow of 500 MW to the remote system, and 1000 MW though the LCC link (Figure 5.18d through Figure 5.18g).

Lastly, the synchronization to the MMC 2's rectifier occurs by closing circuit breaker CB_3 at t = 14 sec, and the offshore wind power increases by 1000 MW to be transferred to Main Grid 2 via MMC 2 at t = 14 sec respectively as shown in (Figure 5.18b and Figure 5.18c).

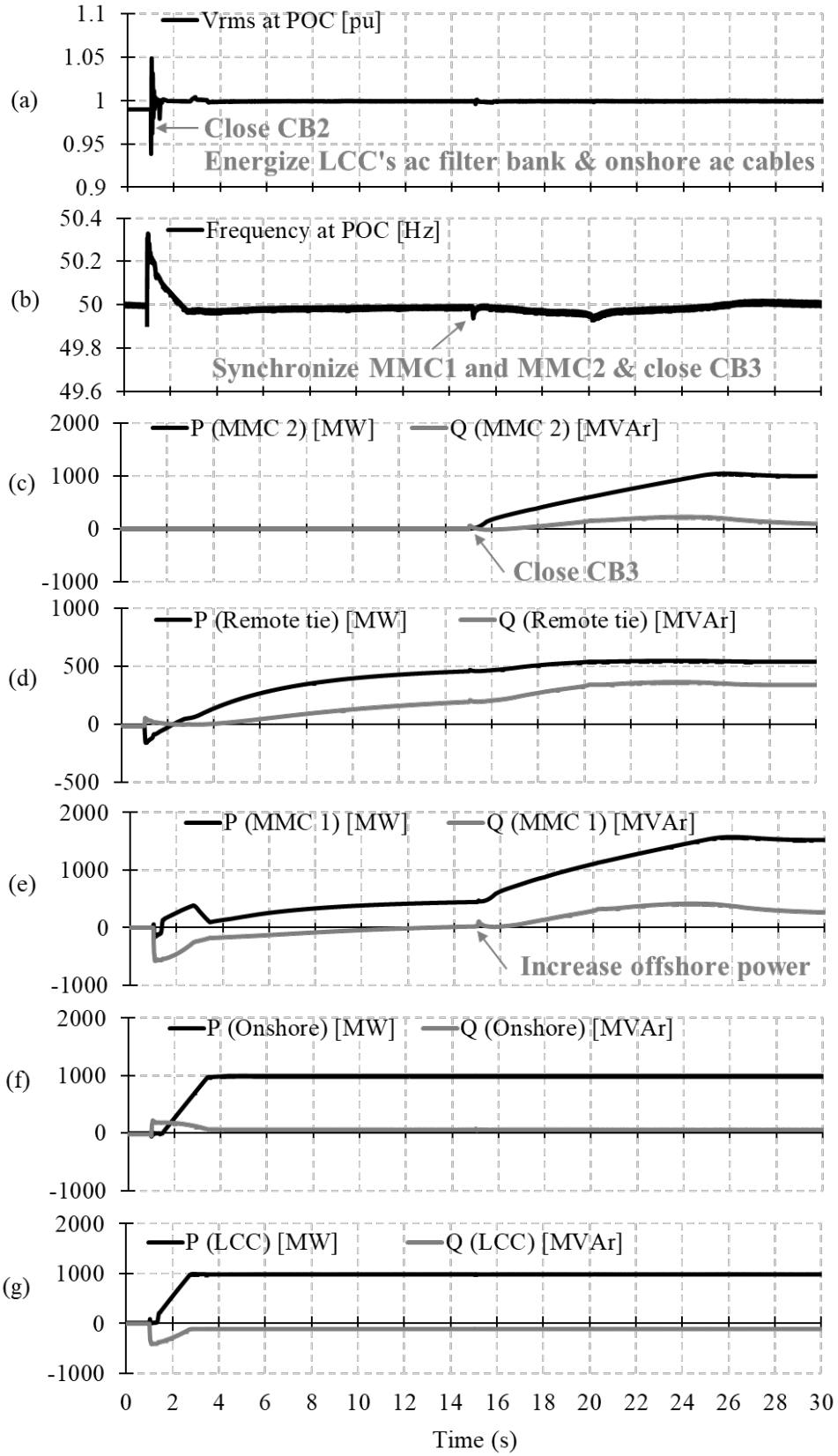

Figure 5.18: Results of synchronizing MMC 1 and remote system followed by MMC 2

Overall, the proposed grid-forming method allows for successful synchronization of two MMC-HVdc links. In addition, the blacked out system is completely energized within 4 sec, whereas the full network resumes normal transmission in 30 sec.

5.2.7.2 Scenario 2: Synchronization MMC 2 and Remote System Followed by MMC 1

Initially, MMC 2's rectifier is used to operate in the grid-forming mode and provide ac voltage at the POC to which the LCC rectifier and the onshore windfarm can synchronize, i.e. CB_3 is closed. As explained previously, the POC bus is synchronized to the remote network through the 200 km tie line by turning on CB_2, and the offshore and onshore wind power is ramped to establish the required power flow of 1000 MW though the LCC link (Figure 5.19d through Figure 5.19g).

Lastly, the synchronization to the MMC 1's inverter occurs by closing circuit breaker CB_3 at t = 6 sec. The offshore wind power is ramped to 1500 MW to transfer 1000 MW to Main Grid 2 via MMC 2 and 500 MW to the remote system through a 200 km tie line respectively as shown in (Figure 5.19b and Figure 5.19c).

Overall, the proposed grid-forming method allows for successful synchronization of two MMC-HVdc links. Similar to scenario 1, the blacked out system is completely energized within 4 sec, whereas the full network resumes normal transmission in 30 sec.

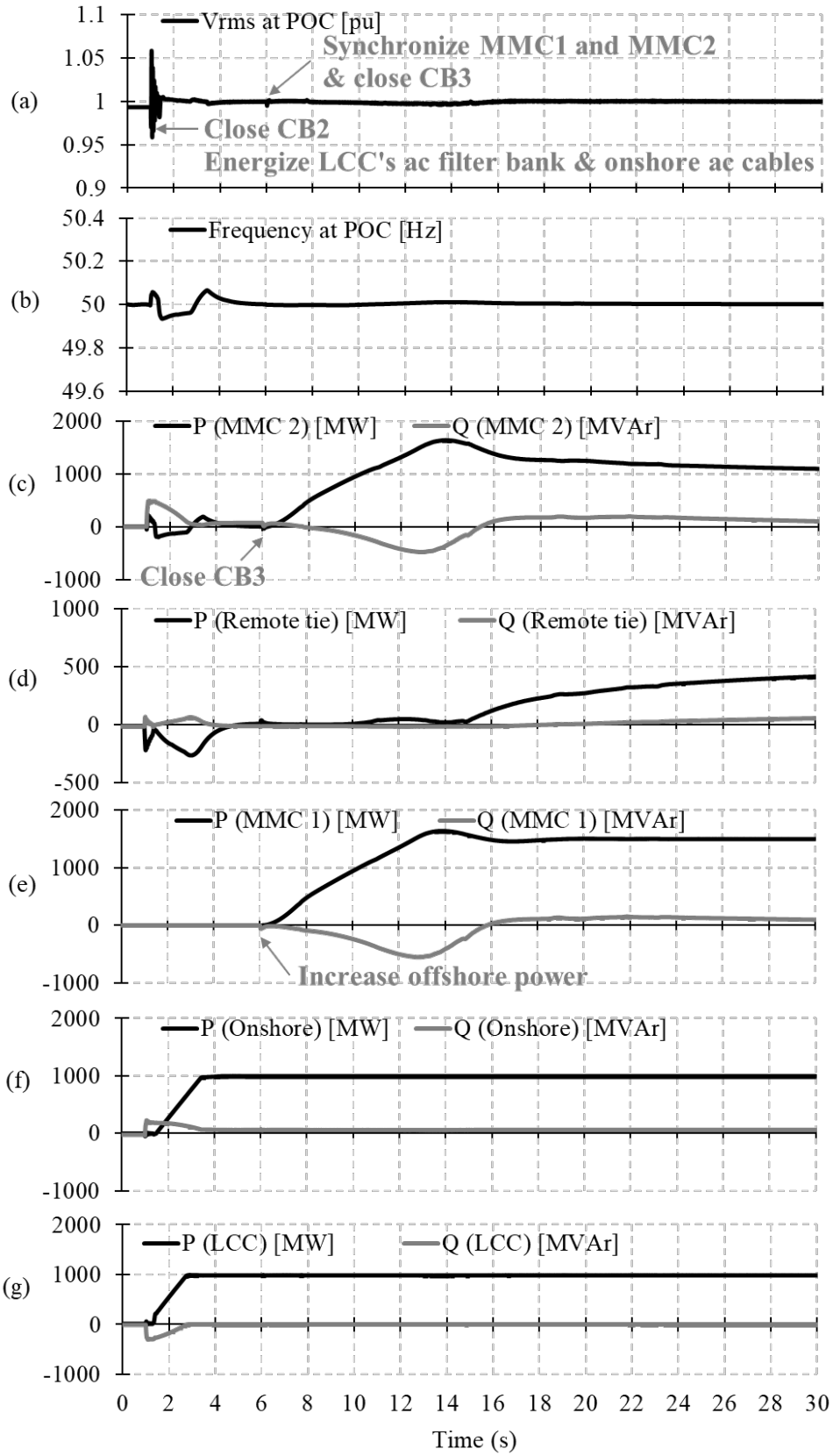

Figure 5.19: Results of synchronizing MMC 2 and remote system followed by MMC 1

5.2.7.3 Scenario 3: Synchronization of MMC 1 and MMC 2 Followed by Remote System

Initially, both MMC 1's inverter and MMC 2's rectifier are synchronized and connected to POC in the grid-forming mode to provide ac voltage to which the LCC rectifier and onshore windfarm can synchronize, i.e. CB_1 and CB_3 are closed. Lastly, the synchronization of POC bus to the remote system occurs at t = 5 sec through the 200 km tie line by closing circuit breaker CB_2 at t = 5 sec (Figure 5.20a and Figure 5.20b). The offshore and onshore wind power is ramped to establish the required power flow of 1000 MW though the LCC link, 1000 MW to Main Grid 2 via MMC 2 and 500 MW to the remote system through a 200 km tie line respectively (Figure 5.20c through Figure 5.20g).

Overall, the proposed grid-forming method allows for successful synchronization of two MMC-HVdc links. However, the restoration is faster with normal power transmission established in 10 sec, and is thus much faster than the previous two scenarios.

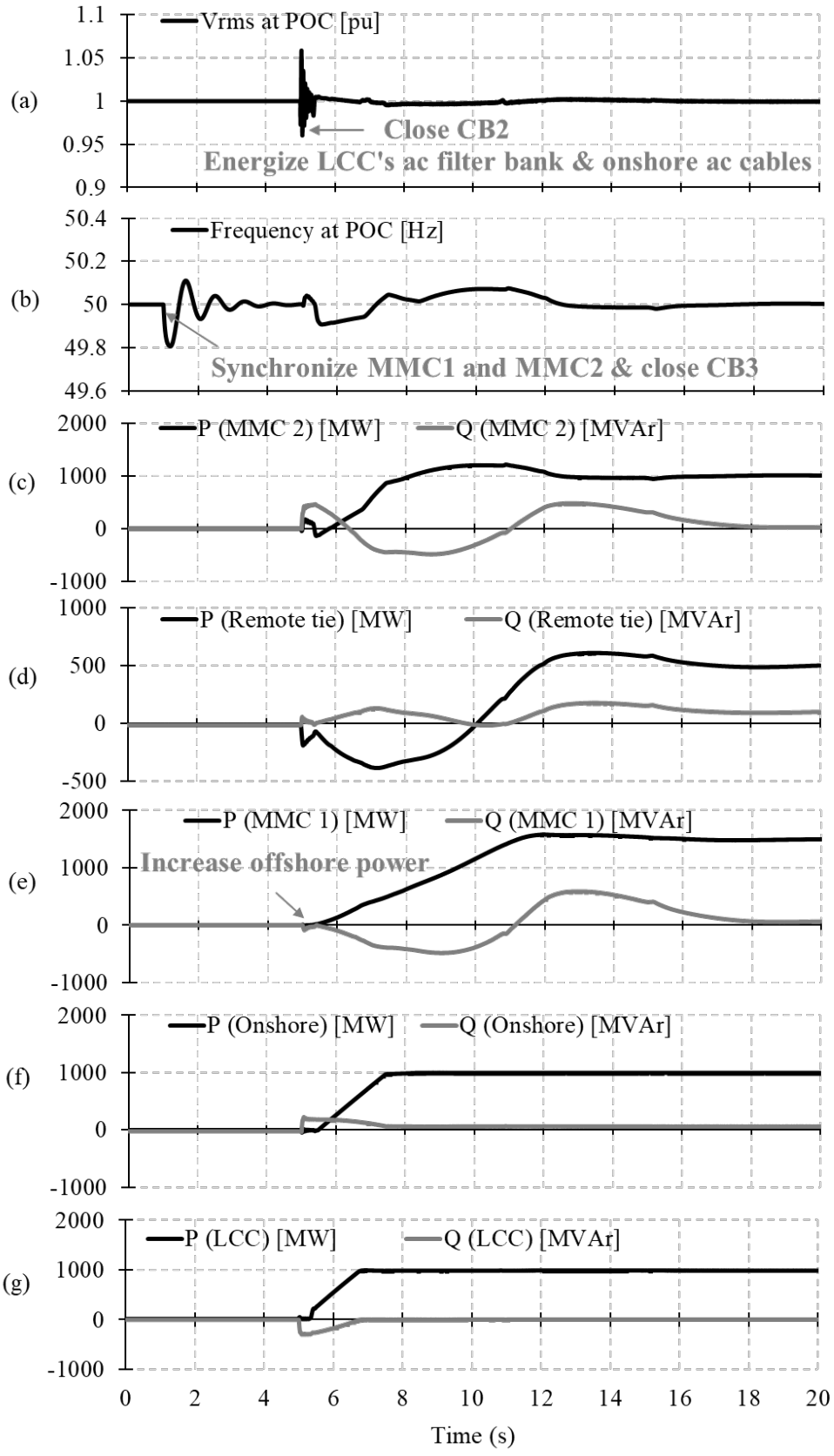

Figure 5.20: Results of synchronizing MMC 1 and MMC 2 followed by remote system

5.2.7.4 Summary of Synchronizing Scenarios

All restoration options are successful in restoration of the LCC link, offshore and onshore systems and remote network, and can be selected based on the priority of the restoration plan when both MMC 1's inverter and MMC 2's rectifier are in grid-forming mode. It should be noted that when all synchronizations are established first, e.g. MMC 1 to MMC 2 and then to the remote system, the total restoration time is reduced significantly to about 10 sec from about 30 sec.

It should be noted that in the cases studied in this Chapter, the controls of the two MMC converters could be adjusted to give stable operation. In a real expansion scenario, one of the converter could have pre-dated the other by several years. In these cases, sometimes the control structure and settings may not be precisely known, either due to lost information or manufacturer's policies to only provide 'black box' type models on a simulator. Care must be taken to coordinate with all parties involved so that the controller settings can be modified to ensure a robust operation.

5.3 Chapter Concluding Remarks

Chapter 5 investigates the performance and reliability of the proposed grid-forming method in two complex real world systems through a series of EMT simulation tests. The first case study is focused on the application of proposed method in a traditional ac system consisting of a local area with generation, and a tie to a remote network. Two black start restoration approaches are investigated. Option 1, in which the local load is picked up first, followed by the remote network; and option 2, in which the remote network is picked up first followed by the local load. Both options successfully restore power to the local and remote networks, and can be selected based on the priority of the restoration plan. However, it was observed that full power transfer to the remote network can be made faster if the converter is not loaded first with the local load as in option 2.

The second case study is to demonstrate the functionality of the proposed method in an inverter-based system consisting of an offshore and onshore wind power generation, a LCC and MMC link and a tie to a remote network to transfer the generated power. Two different black start options are considered, one in which the MMC is used to energize the

LCC link and windfarms before connecting to the remote network, and the second, in which it first makes the connection to the remote network. Similar to case study 1, both restoration options are successful in restoration of the LCC link, offshore and onshore system, and remote network. It should be noted that the case study 2 allows for a significantly faster restoration process due to the presence of inverter-based generation compares to the case study 1.

In addition, the fault ride-through capability of the proposed approach is demonstrated through application of worst-case single- and three-phase to ground faults for all case studies. Restoration to full power can be achieved within 80 ms following the fault clearance.

Finally, the main role of grid-forming control in establishing system frequency is demonstrated by tripping the tie connection to the remote network due to a permanent fault. It is shown that in the absence of a converter with grid-forming capability, the loss of 200 km transmission line to the remote network results in no intrinsic generation to generate synchronous voltage reference for the PLLs to synchronize. Therefore, the frequency of POC fluctuates beyond the protection level of windfarms such that the windfarms trip and results in the loss of the entire generation.

In addition, the case of multiple grid-forming inverters are successfully investigated in a multi-infeed HVdc system. Various synchronization sequences were investigated, and it is found that the fastest black start recovery occurred when all synchronizations are established first, i.e. MMC 1 to MMC 2 and then to the remote system. The next chapter summarizes the research achievements and future work.

Chapter 6

Concluding Remarks and Future Work

This chapter presents the state of the research achieved and discusses future directions for the potential graduate thesis.

6.1 Research Achievements Presented in this Thesis

A detailed literature review was carried out to understand the concept of grid-forming state-of-the-art and gaps in present knowledge. It was concluded that a new grid-forming methodology was required to address the challenges of the existing methods. It included the ability to limit the current during the fault, allow synchronizing either to an

external network or to a purely passive network, work as part of a larger system whose structure and operating point can change unpredictably, and work well for black start scenarios. A challenge faced by grid-forming converters is how to limit the current. Several methods has been proposed such as supervisory current limiting and virtual impedance current limiting method.

Consequently, this thesis proposed a voltage control methodology, which produced the reference currents for the decoupled current controller used to overcome the challenges of existing methods. The current block was shown to be superior to both supervisory current limiting control and virtual impedance based control. The method also provided fault ride-through capability. In addition, an improved synchronization approach was developed for black starting a weak network. The proposed method was implemented via a power synchronizer that automatically aligned the phase angle and the magnitude of voltages on both sides of the circuit breaker before closing to eliminate any excessive current flow.

Additionally, since the analytical approach is only effective around a given operating point and cannot select the optimum gains when the operating condition changes from one to another, the optimization of control parameters becomes more realistic for complex systems. Therefore, this thesis used the Non-linear Simplex algorithm of Nelder and Mead to optimize the control parameters of the proposed methodology. This method was selected because it allows for optimization of multiple real variables. Also, only function values are needed for the algorithm, and not the derivatives compared to other optimization programs. Therefore, it is significantly easier to implement.

Furthermore, this thesis investigated the application of proposed method in two case studies. The first case study was focused on the application of proposed method in a traditional ac system consisting of a local area with generation, and a tie to a remote network. Two black start restoration approaches were investigated. Option 1, in which the local load was picked up first, followed by the remote network; and option 2, in which the remote network was picked up first followed by the local load. Both options successfully restored power to the local and remote networks, and could be selected based on the priority of the restoration plan. However, it was observed that full power transfer to the remote

network could be made faster if the converter was not loaded first with the local load as in option 2.

The second case study was to demonstrate the functionality of proposed method in an inverter-based system consisting of an offshore and onshore wind power generation, a LCC and MMC link and a tie to a remote network to transfer the generated power. Two different black start options were investigated, one in which MMC was used to energize the LCC link and windfarms before connecting to the remote network, and the second, in which it first made the connection to the remote network. Both restoration options were successful in restoration of the collector system and remote network, and could be selected based on the priority of the restoration plan. It was observed that the inverter-based generation allowed a significantly faster restoration process. Therefore, the HVdc transmission, where available, could be an attractive alternative compared to the ac transmission.

In addition, the fault ride-through capability of the proposed approach was demonstrated through application of worst-case single- and three-phase to ground faults in all case studies. The proposed method successfully limited the valve current by the current controller loops, and the restoration to full power was successfully achieved following the fault clearance. Also, this thesis explored the impact of network SCMVA on the proposed method, and demonstrated possible solution in case of stability concern when connecting to network with higher SCMVA. For instance, if required, this thesis demonstrated the successful control mode transition from grid-forming to grid-following and vice versa without disturbing the system normal operation.

Furthermore, the main role of grid-forming control in establishing system frequency was demonstrated by tripping the tie connection to the remote network due to a permanent fault. It was shown that in the absence of a converter with grid-forming capability, if there were no intrinsic generations to generate synchronous voltage reference for the PLLs to synchronize, the islanded system frequency fluctuated beyond the protection level of windfarms and subsequently resulted in the loss of the entire windfarm generation. In addition, black start restoration for a system with multiple grid-forming inverters was also investigated. This feature would be important when dealing with a restoration of multi-infeed HVdc system. Three scenarios were considered. First, the synchronization of MMC

1's inverter and remote system followed by MMC 2's rectifier. Second, the synchronization of MMC 2's rectifier and remote system followed by MMC 1's inverter. Finally, the synchronization of MMC 1's inverter and MMC 2's rectifier followed by remote system. It was found that the fastest black start recovery occurred when all synchronizations were established first, i.e. MMC 1 to MMC 2 and then to the remote system.

Moreover, the performance of proposed method was compared to the supervisory current limiting and virtual impedance current limiting approaches. It was determined that the new proposed method offers a simple design approach in achieving current limiting, which results in easier control tuning and a superior performance.

Finally, the test systems were implemented based on real world setup to cover all possible configurations under worst network conditions to examine the performance of the proposed methodology. Due to the complexity of test systems, an optimization method was developed to tune the control parameters to provide the most robust performance for such network conditions. Each network presents its unique challenges; therefore, to expand the proposed methodology to other networks, the designers must verify the performance of the proposed methodology by performing a comprehensive set of system-wide EMT studies.

6.2 Future Work

The work reported in this thesis was largely carried out using EMT simulation. Controller design was carried out through non-linear optimization. To complete the topic, some of these issues could be studied analytically:

- Use a linearized eigen-value analysis of the overall system using the proposed black start approaches. This would have the advantages of rapidly selecting control parameters from root locus or similar approaches, and would be able to more directly identify interactions between equipment and controllers. On the other hand, it would not be suitable to study large-scale phenomena as the optimization approach does. A potential scenario would be to investigate the potential control interaction of the proposed method in a multi-infeed HVdc system or with a nearby synchronous generator

- In the thesis, the emphasis was on black starting a multi-infeed HVdc grid. However. The investigation of the black start restoration of a HVdc grid with multiple converters on the dc side has not been considered. In addition, the converters' controls could interfere with each other. This also needs further investigation.

References

[1] Tripti Lahiri, "How Many People Actually Lost Power?" *The Wall Street Journal*. August 5, 2012, available: https://blogs.wsj.com/indiarealtime/2012/08/01/how-many-people-actually-lost-power-in-india/

[2] "Final Report on the August 14, 2003 Blackout in the United States and Canada: Causes and Recommendations", *Office of Electricity Delivery & Energy Reliability, U.S./Canada Power System Outage Task Force.* United States Department of Energy. *April 2004.*

[3] "North American Electric Reliability Corporation (NERC) Rules of Procedure Effective in Manitoba", April 12, 2011, available: https://www.hydro.mb.ca/regulatory_affairs/electric/mb_nerc_rules.pdf

[4] CIGRÉ WGB4.52, "HVDC Grid Feasibility Study," CIGRÉ Brochure 533, April 2013.

[5] Y. Xue, C. Yang, and X. Zhang, "Investigation of black start capability of LCC HVDC system with controllable capacitors," in IET ACDC, Beijing, China, May 28-29 2016.

[6] M. Mohaddes, D.P. Brandt, H. Huang, T. Schultheis, and G. Wild, "Supplying dead load with a conventional HVDC system," Colloquium on Role of HVDC, FACTS and Emerging Technologies in Evolving Power Systems, Bangalore, India, September 23-24 2005.

[7] M. Andersson, R. Cai, and C. Yang, “Black start of a passive AC network using bipolar LCC HVDC,” in IET ACDC, Beijing, China, May 28-29 2016.

[8] B. Li, T. Liu, W. Xu, Q. Li, Y. Zhang, Y. Li, and X.Y. Li, "Research on technical requirements of line-commutated converter-based high-voltage direct current participating in receiving end AC system's black start," in IET Generation, Transmission & Distribution, vol. 10, no. 9, pp. 2071-2078, 9 6 2016.

[9] Y. Jiang-Hafner, H. Duchen, M. Karlsson, L. Ronstorm, and B. Abrahamsson, “HVDC with Voltage Source Converters – A Powerful Standby Black Start Facility,” in *Proc. IEEE PES T&D Conference,* Chicago, USA, 2008.

[10] B. Feng, X. Zhai, Y. Li, and Z. Wang, “Experimental study on black-start capability of VSC-HVDC for passive networks,” in *Proc. IEEE PES APPEEC,* Xi’an, China, 2016.

[11] M. Bahrman and P.E. Bjorklund, “The New Black Start: System Restoration with Help from Voltage-Sourced Converters,” *IEEE Power and Energy Magazine*, vol. 12, no. 1, pp. 44-53, Jan.-Feb. 2014.

[12] Z. Li and G. Tan, “A Black Start Scheme Based on Modular Multilevel Control-High Voltage Direct Current,” *Energies*, vol. 11, 2018.

[13] Ying Jiang-Hafner, H. Duchen, M. Karlsson, L. Ronstrom and B. Abrahamsson, "HVDC with voltage source converters - a powerful standby black start facility," 2008 IEEE/PES T & D Conference and Exposition, Chicago, IL, 2008, pp. 1-9.

[14] N. Macleod, N. Cowton, and J. Egan, “System restoration using the black start capability of the 500 MW EirGrid east-west VSC HVDC interconnector,” in IET conference on RTDN, Birmingham, UK, September 22-24 2015.

[15] T. Midtsund, A. Becker, J. Karlsson, and K.A. Egeland, “A live black-start capability test of a voltage source HVDC converter,” in CIGRÉ Canada Conference, Winnipeg, CA, August 31 – September 2, 2015.

[16] N. Flourentzou, V. G. Agelidis, and G. D. Demetriades, “VSC-based HVDC power transmission systems: An overview,” *IEEE Transactions on Power Electronics*, vol. 24, no. 3, pp. 592-602, March 2009.

[17] S. Allebrod, R. Hamerski, and R. Marquardt, “New transformless, scalable modular multilevel converters for HVDC transmission,” in *IEEE Power Electronics Specialists Conference – PESC 2008*, Rhodes, Greece, 2008.

[18] M. Hagiwara and H. Akagi, “Control and experiment of pulsewidth-modulated modular multilevel converters,” *IEEE Transactions on Power Electronics*, vol. 24, no. 7, pp. 1737-1746, July 2009.

[19] M. Glinka and R. Marquardt, “A new AC/DC multilevel converter family,” *IEEE Transactions on Power Electronics*, vol. 52, no. 3, pp. 662-669, June 2005.

[20] M. Davies, M. Dommaschk, J. Dorn, J. Lang, D. Retzmann, and D. Soerangr, “HVDC Plus – basics and principle of operation,” Siemens Energy Sector, 2008.

[21] J. Z. Zhou, H. Ding, S. Fan, Y. Zhang and A. M. Gole, "Impact of Short-Circuit Ratio and Phase-Locked-Loop Parameters on the Small-Signal Behavior of a VSC-HVDC Converter," IEEE Transactions on Power Delivery, vol. 29, no. 5, pp. 2287-2296, Oct. 2014.

[22] J. Z. Zhou and A. M. Gole, "VSC transmission limitations imposed by AC system strength and AC impedance characteristics," 10th IET International Conference on AC and DC Power Transmission (ACDC 2012), Birmingham, 2012, pp. 1-6.

[23] L. Zhang, “Modeling and Control of VSC-HVDC Links Connected to Weak ac Systems,” Ph.D. Dissertation, Royal Institute of Technology, Stockholm, Sweden, 2010.

[24] O. Stanojev, “Partial grid forming concept for 100% inverter-based transmission systems,” Thesis, ETH, Zurich, Switzerland, 2018.

[25] Q. Zhong, P. Nguyen, Z. Ma, and W. Sheng, “Self-synchronized synchroconverters: inverters without a dedicated synchronization unit,” *IEEE Transactions on Power Electronics*, vol. 29, no. 2, pp. 617-630, Feb. 2014.

[26] M. Ashabani, Y. Abdel-Rady, and I. Mohamed, “Novel comprehensive control framework for incorporating VSCs to smart power grids using bidirectional synchronous-VSC,” *IEEE Transactions on Power Systems*, vol. 29, no. 2, pp. 805-814, Mar. 2014.

[27] S. Henninger, M. Schroeder, and J. Jaeger, “Grid-forming droop control of a Modular Multilevel Converter in Laboratory,” in PESGM, Portland, USA, Aug. 2018.

[28] A. Paquette and D. Divan, “Virtual impedance current limiting for inverters in microgrids with synchronous generators,” *IEEE Transactions on Industrial Applications*, vol. 51, no. 2, pp. 1630-1638, Mar. 2015.

[29] J. He and Y.W. Li, "Analysis, design, implementation of virtual impedance for power electronics interfaced distributed generation," *IEEE Transactions on Industrial Application*, vol. 47, no. 6, pp. 2525-2538, Nov./Dec. 2011.

[30] H.P. Beck and R. Hesse, "Virtual synchronous machine," *Proceedings of the 9th International Conference on Electrical Power Quality and Utilisation,* pp. 1-6, Oct. 2007.

[31] Q. C. Zhong and G. Weiss, "Synchroconverters: Inverters that mimic synchronous generators," *IEEE Transactions on Industrial Electronics*, vol. 58, no. 4, pp. 1259-1267, Apr. 2011.

[32] M. A. El-Sharkawi, *Wind Energy: An Introduction*. CRC Press, 2016.

[33] L. Max, "Energy evaluation for DC/DC converters in DC-based wind farms," Licentiate Thesis, Chalmers University of Technology, Göteborg, Sweden, 2007.

[34] P. Roshanfekr, "Energy-efficient generating system for HVDC off-shore wind turbine," Licentiate Thesis, Chalmers University of Technology, Göteborg, Sweden, 2013.

[35] S. Heier, *Grid Integration of Wind Energy: Onshore and Offshore Conversion Systems*. John Wiley and Sons, 2014.

[36] O. Anaya-Lara, D. Campos-Gaona, E. Moreno-Goytia, and G. Adam, *Offshore Wind Energy Generation: Control, Protection, and Integration to Electrical Systems*. John Wiley and Sons, 2014.

[37] "VSC transmission," CIGRÉ Working Group B4.37-269, Tech. Rep., 2005.

[38] E. W. Kimbark, *Direct Current Transmission, Vol. I.* New York: Wiley, 1971.

[39] J. Arrillaga, *High Voltage Direct Current Transmission, 2nd Edition*. London: The Institution of Electrical Engineers, 1998.

[40] C. Barker, *HVDC for beginners and beyond*, Alstom Grid, UK, 2002.

[41] T. Smed and G. Andersson, "Utilizing HVDC to damp power oscillations," in *IEEE Transactions on Power Delivery*, vol. 8, no. 2, pp. 620-627, April 1993.

[42] P. Agnihotri, A.M. Kulkarni, A.M. Gole, B.A. Archer, and T. Weekes, "A robust wide-area measurement based damping controller for networks with embedded multi-terminal and multi-infeed HVDC links," in *IEEE Transactions on Power Systems*, vol. 32, no. 5, pp. 3884-3892, 2017.

[43] P. Agnihotri, A.M. Kulkarani, and A.M. Gole, "Robust global control strategies for improvement of angular stability using FACTS and HVDC devices," in *International Journal of Emerging Electric Power Systems*, vol. 14, no. 1, pp. 95-104, 2013.

[44] S. Corsi, A. Danelli, and M. Pozzi, "Emergency-stability controls through HVDC links," in *IEEE Power Engineering Society Summer Meeting*, Chicago, USA, 2002.

[45] W. Breuer, M. Lemes, and D. Retzmann, "Perspectives of HVDC and FACTS for system interconnection and grid enhancement," in *CIGRÉ Workshop: Brazil-China-India Summit Meeting on HVDC and Hybrid Systems*, Rio de Janeiro, Brazil, 2006.

[46] G. Andersson, P. Donalek, R. Farmer, and N. Hatziargyriou, "Causes of the 2003 major grid blackouts in North America and Europe, and recommended means to improve system dynamic performance," *IEEE Transactions on Power System*, vol. 20, no. 2, pp. 1922-1928, November 2005.

[47] M. Bahrman and B. Johnson, "The ABCs of HVDC transmission technologies," *IEEE Power Energy Magazine*, vol. 5, no. 2, pp. 32-44, March/April 2007.

[48] O. B. Nayak, A. M. Gole, D. G. Chapman, and J. B. Davies, "Dynamic performance of static and synchronous compensators at an HVDC inverter bus in a very weak ac system," *IEEE Transactions on Power System*, vol. 9, no. 3, pp. 1350-1358, August 1994.

[49] D. Jovcic, N. Pahalawaththa, and M. Zavahir, "Investigation of the use of inverter control strategy instead of synchronous condensers at inverter terminal of an HVDC system," *IEEE Transactions on Power Delivery*, vol. 15, no. 2, pp. 704-709, April 2000.

[50] "IEEE guide for planning DC links terminating at AC locations having low short circuit capacities," IEEE Std 1204-1997, Tech. Rep., 1997.

[51] C. V. Thio, J. B. Davies, and K. L. Kent, "Commutation failures in HVDC transmission systems," *IEEE Transactions on Power Delivery*, vol. 11, no. 2, pp. 946-957, April 1996.

[52] L. Zhang and M. H. Bollen, "Characteristics of voltage dips in power systems," *IEEE Transactions on Power Delivery*, vol. 15, no. 2, pp. 827-832, April 2000.

[53] "Capacitor commutated converters (CCC) HVDC interconnections: digital modeling and circuit," CIGRÉ Working Group B4.34-352, Tech. Rep., 2008.

[54] S. Dennetier, S. Nguefeu, H. Saad, and J. Mahseredjian, “Modeling of Modular Multilevel Converters for the France-Spain Link,” In *Proc. International Conference on Power Systems Transients (IPST),* Vancouver, Canada, July 2013.

[55] N. Flourentzou, V. G. Agelidis, and G. D. Demetriades, “VSC-based HVDC power transmission systems: An overview,” *IEEE Transactions on Power Electronics*, vol. 24, no. 3, pp. 592-602, March 2009.

[56] F. Schettler, H. Huang, and N. Christl, “HVDC Transmission Systems using Voltage Sourced Converters Design and Applications,” In *Proc. IEEE Power Engineering Society Summer Meeting,* vol. 2, pp. 715-720, 2000.

[57] M. Saeedifard, and R. Iravani, “Dynamic Performance of a Modular Multilevel Back-to-Back HVDC System,” IEEE Trans. on Power Delivery, vol. 25, no. 4, pp. 2903-2912, Oct. 2010.

[58] “DC grid test system,” CIGRÉ Working Group B4.57-492, Tech. Rep., 2014.

[59] CENELEC TC8X, “Technical Guidelines for first HVDC Grid,” CENELECT TC8X/Sec0097/DC, Nov. 2012.

[60] “Control methodologies for direct voltage and power flow in a meshed HVDC grid,” CIGRÉ Working Group B4.58-699, Tech. Rep., 2017.

[61] C. Schauder and H. Mehta, "Vector analysis and control of advanced static VAr compensators," in *IEE Proceedings C - Generation, Transmission and Distribution*, vol. 140, no. 4, pp. 299-306, July 1993.

[62] I. Papic, P. Zunko, D. Povh and M. Weinhold, “Basic control of unified power flow controller,” in *IEEE Transactions on Power Systems*, vol. 12, no. 4, pp. 1734-1739, Nov. 1997.

[63] P. Kundur, “Power System Stability and Control,” 2nd ed.,McGraw-Hill, 1994.

[64] A. M. Gole, S. Filizadeh, R. W. Menzies, P. L. Wilson, “Optimization-Enabled Electromagnetic Transient Simulation”, IEEE Trans. on Power Delivery, 2004

[65] S. Filizadeh, A. M. Gole, D. A. Woodford and G. D. Irwin, "An Optimization-Enabled Electromagnetic Transient Simulation-Based Methodology for HVDC Controller Design," in *IEEE Transactions on Power Delivery*, vol. 22, no. 4, pp. 2559-2566, Oct. 2007.

[66] J. A. Nelder and R. Mead, "A simplex method for function minimization," *Comput. J.*, vol. 7, no. 4, pp. 308–313, 1965.

[67] E.On Netz GmbH, "Grid Code High and extra high voltage," April 2006, available: https://www.nerc.com/docs/pc/ivgtf/German_EON_Grid_Code.pdf.

[68] E. Kim, J. Kim, S. Kim, J. Choi, K.Y. Lee, and H. Kim, "Impact analysis of wind farms in the Jeju island power system" *IEEE Systems Journal*, vol. 6, no. 1, pp. 134-139, Mar. 2012.

[69] Offshore Projects Germany, June 2020, available: https://www.tennet.eu/index.php?id=2130&L=0.

[70] M. Zahid Khan, M. Mansoor Khan, H. Jiang, K. Hashmi, and M.U. Shahid, "An improved control strategy for three-phase power inverters in islanded AC microgrids," *Inventions Journal*, vol. 47, no. 3, July 2018.

[71] C. Arie Plet, "Fault Response of Inverter-based Distributed Generation," Ph.D. Dissertation, Imperial College London, London, UK, 2011.

[72] T. Green and M. Prodanović, "Control of inverter-based micro-grids," in *Electric Power Systems Research* , vol. 77, no. 9, pp. 1204-1213, July 2007.

[73] J. Z. Zhou and A. M. Gole, "Estimation of the Short Circuit Ration and the Optimal Controller Gains Selection of a VSC System," In *Proc. International Conference on Power Systems Transients (IPST),* Vancouver, Canada, July 2013.

Appendix A

Mathematical Representation of Proposed Grid-forming Method

A state space model was used in section 3.3.5 to show the poorer performance of the grid-forming converter for larger SCMVA values. This Appendix, shows the derivation of the state-space equation of the MMC-HVdc system, which considers the power synchronization and control dynamics, the dual control system, and the dynamics of the ac network. Figure A.1a shows the MMC inverter considered in this chapter and Figure A.1b shows its equivalent circuit used for developing the small-signal model. The ac source is modeled as a Thévenin impedance consisting of R_s and L_s. The MMC side is modeled by the total inductance, L, and a source v_c representing the MMC's internal voltage.

(a)

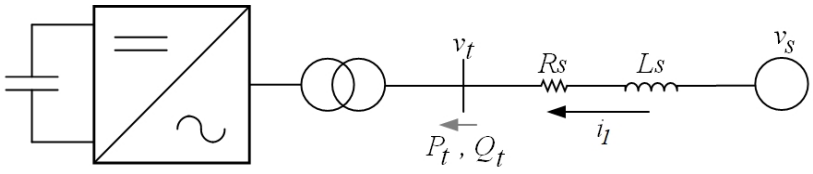

(b)

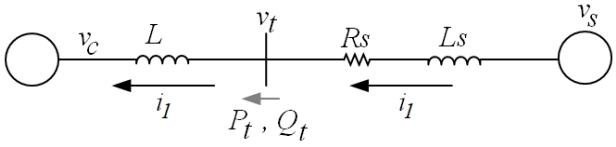

Figure A.1: Simplified system for eigenvalue analysis (a) Full MMC inverter representation (b) The equivalent circuit for small-signal analysis

A.1. Differential-Algebraic Equation of Ac System Network

$$L\frac{dI_{1d}}{dt} = V_{td} - V_{cd} - \omega L I_{1q} \tag{A1}$$

$$L\frac{dI_{1q}}{dt} = V_{tq} - V_{cq} + \omega L I_{1d} \tag{A2}$$

$$L_s\frac{dI_{1d}}{dt} = V_{sd} - V_{td} - \omega L_s I_{1q} - R_s I_{1d} \tag{A3}$$

$$L_s\frac{dI_{1q}}{dt} = V_{sq} - V_{tq} + \omega L_s I_{1d} - R_s I_{1q} \tag{A4}$$

A.2. Differential-Algebraic Equation of Filtering Measuring Signals

$$T\frac{dV_{tdf}}{dt} = -V_{tdf} + V_{td} \tag{A5}$$

$$T\frac{dV_{tqf}}{dt} = -V_{tqf} + V_{tq} \tag{A6}$$

$$T\frac{dI_{df}}{dt} = -I_{df} + I_d \tag{A7}$$

$$T\frac{dI_{qf}}{dt} = -I_{qf} + I_q \tag{A8}$$

A.3. Differential-Algebraic Equation of Upper Level Controller

$$\frac{dx_1}{dt} = V_{ref} - \sqrt{V_{tdf}^2 + V_{tqf}^2} \tag{A9}$$

$$V_{dmag} = K_{iAC}x_1 + K_{pAC}\left(V_{ref} - \sqrt{V_{tdf}^2 + V_{tqf}^2}\right) \tag{A10}$$

A.4. Differential-Algebraic Equation of Dual Controller

$$\frac{dx_2}{dt} = V_{dmag} - V_{tdf} \tag{A11}$$

$$I_{dref} = -K_{ivd}x_2 - K_{pvd}\left(V_{dmag} - V_{tdf}\right) \tag{A12}$$

$$\frac{dx_3}{dt} = -V_{tqf} \tag{A13}$$

$$I_{qref} = -K_{ivq}x_3 + K_{pvq}V_{tqf} \tag{A14}$$

$$\frac{dx_4}{dt} = I_{dref} - I_{df} \tag{A15}$$

$$V_{cd} = V_{tdf} - \omega L I_{qf} - K_{iid}x_4 - K_{pid}\left(I_{dref} - I_{df}\right) \tag{A16}$$

$$\frac{dx_5}{dt} = I_{qref} - I_{qf} \tag{A17}$$

$$V_{cq} = V_{tqf} + \omega L I_{df} - K_{iiq}x_5 - K_{piq}\left(I_{qref} - I_{qf}\right) \tag{A18}$$

A.5. Differential-Algebraic Equation of Power Synchronization and Control

$$J\frac{d\omega}{dt} = -D\omega + V_{tdf}I_{df} + V_{tqf}I_{qf} - P_{ref} \tag{A19}$$

$$\frac{d\theta}{dt} = \omega \tag{A20}$$

A.6. Differential-Algebraic Equations in Linearized form

$$T\frac{d\Delta V_{tdf}}{dt} = -\Delta V_{tdf} + \Delta V_{td} \tag{A19}$$

$$T\frac{d\Delta V_{tqf}}{dt} = -\Delta V_{tqf} + \Delta V_{tq} \tag{A20}$$

$$T\frac{d\Delta I_{df}}{dt} = -\Delta I_{df} + \Delta I_{d} \tag{A21}$$

$$T\frac{d\Delta I_{qf}}{dt} = -\Delta I_{qf} + \Delta I_{q} \tag{A22}$$

$$\frac{d\Delta x_1}{dt} = \Delta V_{ref} - \frac{V_{tdf}}{\left\|V_{tfil}\right\|}\Delta V_{tdf} - \frac{V_{tqf}}{\left\|V_{tfil}\right\|}\Delta V_{tqf} \tag{A23}$$

$$\frac{d\Delta x_2}{dt} = \Delta V_{dmag} - \Delta V_{tdf} \tag{A24}$$

$$\frac{d\Delta x_3}{dt} = -\Delta V_{tqf} \tag{A25}$$

$$\frac{d\Delta x_4}{dt} = \Delta I_{dref} - \Delta I_{df} \tag{A26}$$

$$\frac{d\Delta x_5}{dt} = \Delta I_{qref} - \Delta I_{qf} \tag{A27}$$

$$J\frac{d\Delta\omega}{dt} = -D\Delta\omega + I_{df}\Delta V_{tdf} + V_{tdf}\Delta I_{df} + I_{qf}\Delta V_{tqf} + V_{tqf}\Delta I_{qf} - \Delta P_{ref} \tag{A28}$$

$$\frac{d\Delta\theta}{dt} = \Delta\omega \tag{A29}$$

$$L\frac{d\Delta I_d}{dt} = \Delta V_{td} - LI_q\Delta\omega - \omega L\Delta I_q - \Delta V_{cd} \tag{A30}$$

$$L\frac{d\Delta I_q}{dt} = \Delta V_{tq} + LI_d\Delta\omega + \omega L\Delta I_d - \Delta V_{cq} \tag{A31}$$

$$L_s\frac{d\Delta I_d}{dt} = \Delta V_{sd} - R_s\Delta I_d - L_sI_q\Delta\omega - \omega L_s\Delta I_q - \Delta V_{td} \tag{A32}$$

$$L_s\frac{d\Delta I_q}{dt} = \Delta V_{sq} - R_s\Delta I_q + L_sI_d\Delta\omega + \omega L_s\Delta I_d - \Delta V_{tq} \tag{A33}$$

$$\Delta V_{dmag} = K_{iAC}\Delta x_1 + K_{pAC}\left(\Delta V_{ref} - \frac{V_{tdf}}{\|V_{tfil}\|}\Delta V_{tdf} - \frac{V_{tqf}}{\|V_{tfil}\|}\Delta V_{tqf}\right) \tag{A34}$$

$$\Delta I_{dref} = -K_{ivd}\Delta x_2 - K_{pvd}\left(\Delta V_{dmag} - \Delta V_{tdf}\right) \tag{A35}$$

$$\Delta I_{qref} = -K_{ivq}\Delta x_3 + K_{pvq}\Delta V_{tqf} \tag{A36}$$

$$\Delta V_{cd} = \Delta V_{tdf} - LI_{qf}\Delta\omega - \omega L\Delta I_{qf} - K_{iid}\Delta x_4 - K_{pid}\left(\Delta I_{dref} - \Delta I_{df}\right) \tag{A37}$$

$$\Delta V_{cq} = \Delta V_{tqf} + LI_{df}\Delta\omega + \omega L\Delta I_{df} - K_{iiq}\Delta x_5 - K_{piq}\left(\Delta I_{qref} - \Delta I_{qf}\right) \tag{A38}$$

$$\Delta V_{sd} = V_m sin(\delta - \theta)\Delta\theta \tag{A39}$$

$$\Delta V_{sq} = V_m cos(\delta - \theta)\Delta\theta \tag{A40}$$

A.7. Differential-Algebraic Equation Formulation

On linearizing the above equations, we get the linearized systems as,

$$\boldsymbol{M}\cdot\Delta\dot{\boldsymbol{X}} = \boldsymbol{A}\cdot\Delta\boldsymbol{X} + \boldsymbol{B}\cdot\Delta\boldsymbol{U}$$

Where,

$\Delta\boldsymbol{X} = [\Delta\boldsymbol{x} \quad \Delta\boldsymbol{z}]^T$

$\Delta\boldsymbol{x} = [\Delta V_{tdf} \quad \Delta V_{tqf} \quad \Delta I_{df} \quad \Delta I_{qf} \quad \Delta x_1 \quad \Delta x_2 \quad \Delta x_3 \quad \Delta x_4 \quad \Delta x_5 \quad \Delta\omega \quad \Delta\theta \quad \Delta I_d \quad \Delta I_q]^T$

$\Delta\boldsymbol{z} = [\Delta V_{td} \quad \Delta V_{tq} \quad \Delta V_{dmag} \quad \Delta I_{dref} \quad \Delta I_{qref} \quad \Delta V_{cd} \quad \Delta V_{cq} \quad \Delta V_{sd} \quad \Delta V_{sq}]^T$

$\Delta\boldsymbol{U} = [\Delta P_{ref} \quad \Delta V_{ref}]^T$

Non-zero elements of matrix $\boldsymbol{M}$:

$$M_{1,1} = M_{2,2} = M_{3,3} = M_{4,4} = T$$
$$M_{5,5} = M_{6,6} = M_{7,7} = M_{8,8} = M_{9,9} = M_{11,11} = 1$$
$$M_{10,10} = J$$
$$M_{12,12} = M_{13,13} = L$$
$$M_{14,12} = M_{15,13} = L_s$$

Non-zero elements of matrix $\boldsymbol{A}$:

$$A_{1,1} = A_{2,2} = A_{3,3} = A_{4,4} = A_{6,1} = A_{7,2} = A_{8,3} = A_{9,4} = A_{12,19} = A_{13,20} = A_{14,14} = -1$$
$$A_{15,15} = A_{16,16} = A_{17,17} = A_{18,18} = A_{19,19} = A_{21,21} = A_{22,22} = -1$$
$$A_{1,14} = A_{2,15} = A_{3,12} = A_{4,13} = A_{6,16} = A_{8,17} = 1$$
$$A_{9,18} = A_{11,10} = A_{12,14} = A_{13,15} = A_{19,1} = 1$$
$$A_{5,1} = \frac{-V_{tdf}}{\|V_{tfil}\|}, A_{5,2} = \frac{-V_{tqf}}{\|V_{tfil}\|}$$
$$A_{10,1} = I_{df}, A_{10,2} = I_{qf}, A_{10,3} = V_{tdf}, A_{10,4} = V_{tqf}, A_{10,10} = -D$$
$$A_{12,10} = -LI_q, A_{12,13} = -\omega L$$
$$A_{13,10} = LI_d, A_{13,12} = \omega L$$
$$A_{14,10} = -L_s I_q, A_{14,12} = -R_s, A_{14,13} = -\omega L_s$$
$$A_{15,10} = L_s I_d, A_{15,12} = \omega L_s, A_{15,13} = -R_s$$
$$A_{16,1} = \frac{-K_{pAC} V_{tdf}}{\|V_{tfil}\|}, A_{16,2} = \frac{-K_{pAC} V_{tqf}}{\|V_{tfil}\|}, A_{16,5} = K_{iAC}$$
$$A_{17,1} = K_{pvd}, A_{17,6} = -K_{ivd}, A_{17,16} = -K_{pvd}$$
$$A_{18,2} = K_{pvq}, A_{18,7} = -K_{ivq}$$
$$, A_{19,3} = K_{pid}, A_{19,4} = -\omega L, A_{19,8} = -K_{iid}, A_{19,10} = -LI_{qf}, A_{19,17} = -K_{pid}$$
$$A_{21,11} = V_m sin(\delta - \theta)$$
$$A_{22,11} = V_m cos(\delta - \theta)$$

Non-zero elements of matrix $\boldsymbol{B}$:

$$B_{5,2} = 1, B_{10,1} = -1, B_{16,2} = K_{pAC}$$